UNIVERSITÀ DEGLI STUDI DI CATANIA

DIPARTIMENTO DI FISICA E ASTRONOMIA

TESI DI DOTTORATO DI RICERCA IN FISICA
CICLO XXXI (2015-2018)

First observation of the Pygmy Dipole Resonance in the nucleus ^{68}Ni using an isoscalar probe above the neutron emission threshold

---

Author:
Nunzia Simona Martorana

Supervisors:
Dr. Giuseppe Cardella
Dr. Giuseppe Edoardo Lanza

Tutor:
Prof. Agatino Musumarra

Ph.D Coordinator:
Prof. Vincenzo Bellini

Contents

Introduction **1**

1 General features of the Pygmy Dipole Resonance **5**
1.1 History of the Pygmy modes 5
1.2 Theoretical approach 8
1.2.1 Microscopic model for the low-lying dipole states 11
1.2.2 Nuclear form factors 14
1.3 Link of PDR with the EoS and r-process 19
1.3.1 Constraints on the symmetry energy and neutron skins from Pygmy Dipole Resonance 19
Nuclear Dipole Polarizability 20
1.3.2 Influence of the Pygmy Dipole Resonance to the r-process . 22

2 Experimental method for the study of the PDR **25**
2.1 Real photons 25
2.2 Coulomb excitation 28
2.2.1 Halo nuclei at the neutron dripline and light neutron rich nuclei 29
2.2.2 Intermediate-mass and heavy nuclei 32
2.3 Hadronic interaction 34

3 Experiment **39**
3.1 Pygmy Dipole Resonance in the ^{68}Ni+ ^{12}C reaction 39
3.2 Experimental set-up 41
3.3 FRIBs@LNS facility 42
3.4 Tagging system 46
3.4.1 Production of charge states 47
3.4.2 Calibration of the DSSSD and MCP detector 50
3.4.3 PPAC detector 55

4 CHIMERA and FARCOS multidetectors **57**
4.1 CHIMERA multidetector 57
4.1.1 Silicon detectors 60
4.1.2 CsI(Tl) detectors 63
4.1.3 Electronic chains 65
Electronic chain for Si detectors 66
Electronic chain for CsI(Tl) scintillators 69
4.1.4 Trigger condition 70
Trigger condition for the Pygmy experiment 72
4.1.5 Identification methods 72
4.1.6 Particles detection and identification in CsI(Tl) 73
4.1.7 γ-rays detection and identification 80
4.1.8 Neutron detection 82
4.1.9 CsI(Tl) calibration 82
4.2 FARCOS array 87
4.2.1 Silicon and CsI(Tl) detectors of the FARCOS array 88
4.2.2 FARCOS configuration for the Pygmy experiment 90
4.2.3 Identification method with the FARCOS array 91

5 Decay channels of the PDR: results and discussion **95**
5.1 γ-decay channel 95
5.1.1 Doppler correction 104
5.1.2 CASCADE calculations 104
5.1.3 GEANT4 simulations 108
Folding procedure 109
5.1.4 Comparison with other experiments 112
5.2 Neutron decay channel of the Pygmy Dipole Resonance: method and preliminary results 116
5.3 Outlook 118
5.3.1 FraISe: the new INFN-LNS facility for in-flight RIBs production 118

Conclusion **122**

A Semiclassical calculations **127**

Bibliography **131**

List of Figures

1.1 Comparison of the measured (solid curves) and calculated spectra of the neutron capture γ-rays. The dashed curves present the results of calculations when both giant and pigmy resonance are accounted for. The dashed-dotted curves give results of calculations in which no account was taken for the pigmy resonance[6]. 6
1.2 RPA strength distributions for isovector (upper) and isoscalar (lower) response for Ni isotopes. 9
1.3 Schematic representation of the PDR state generated as an oscillation of the core against the neutron skin. 10
1.4 RPA transition densities calculated for the ^{68}Ni in the case of: the low-lying dipole states (a)-(d), the IVGDR (b)-(e) and the ISGDR (c)-(f). As indicated in the legends the proton, neutron, isoscalar and isovector components are plotted. 13
1.5 Comparison among the transition densities calculated with the RPA, HD and MPM models in the case of isoscalar and isovector modes of the PDR [4]. 13
1.6 Schematic representation of the interaction between two nuclei as described by the Eq. 1.13. 14
1.7 (a) Form factors for the system ^{68}Ni + ^{12}C for the PDR state. (b) Form factors for the system ^{68}Ni + ^{12}C for the ISGDR state. These form factors are calculated with the RPA, HD and MPM models [4]. 16
1.8 (a) Differential cross section for the the system ^{68}Ni + ^{12}C for the PDR state. (b) Differential cross section for the system ^{68}Ni + ^{12}C for the ISGDR state [4]. 17

1.9 Upper part: E1 strength distribution calculated, up to 12 MeV for the ^{116}Sn (left) and up to 10 MeV for the ^{140}Sn (right), in RQRPA and RQTBA [37]. Lower part: proton and neutron transition densities corresponding to the most pronounced peaks at low excitation energies at 8.94 MeV and 11.78 MeV for the ^{116}Sn, and 7.18 MeV and 10.94 MeV for the ^{140}Sn, respectively. For comparison the transition densities in the region of the GDR for both nuclei in the RQRPA calculation are also given. Figure taken from ref. [1]. 18

1.10 In the panel (a) the correlation between L and the percentage of sum rule for the PDR in the ^{68}Ni is plotted. In panel (b) the correlation between L and the neutron skin in the ^{68}Ni is shown. The numbers refer to several models used in the calculation [42]. 20

1.11 Correlation between neutron-skin thickness and dipole polarizability in ^{68}Ni using FSUGold [45]. The shaded zones indicate the experimental errors on the measured α_D and extrapolated $\Delta R_{n,p}$ values [44]. 21

1.12 (a) Ratio of the Maxwellian-averaged (n,γ) rates, calculated at T=1.5 10^9 K with GDR+ PR and without the PR contribution, as a function of N for 3100 neutron-rich nuclei involved in the r-process. (b) same as (a) as a function of S_n [46]. 23

1.13 (a) r-abundance distributions for T=10^9 K and neutron density N= 10^{20} cm^{-3} with three different calculations of the neutron capture rates: the standard GDR component, the GDR + PDR strength and the damped statistical CN plus DC contribution. The top curve corresponds to the solar r-abundances arbitrarily normalized. (b) same as (a) for a T=1.5 10^9 K and a neutron density N= 10^{28} cm^{-3}[46]. . . 24

2.1 Upper: Measured E1 strength distribution in ^{136}Xe up to the neutron separation energy. The dotted line indicates the sensitivity limit of the experiment[47]. Lower: γ-rays spectrum obtained for ^{88}Sr and corrected for background and detector response [48]. 27

2.2 Dipole-strength distribution of ^{11}Be extracted from a measurement of Coulomb breakup of a 520 MeV/nucleon ^{11}Be beam impinging on a Pb target. The data are from Palit et al. [49]. The solid curve shows a theoretical analysis of Typel and Baur in an effective-range approach[50]. Figure taken from [50]. 30

2.3 Photoneutron cross section for ^{16}O as measured with real photons [51] (upper panel), and for the unstable isotopes ^{20,22}O (lower panels) as extracted from the measured electromagnetic excitation cross section (symbols). The inset displays the cross section for ^{20}O near the neutron threshold on an expanded energy scale. The thresholds for decay channels involving protons are indicated by arrows. For ^{20,22}O, the data are compared to the shell model calculations[52]. Figure taken from [12]. 31

2.4 Electromagnetic dissociation cross sections and deduced photo-neutron cross sections for ^{130}Sn and ^{132}Sn. The dashed and dash-dotted curves show the fitted Gaussian and Lorentzian distributions assigned to the PDR and GDR respectively, while the red solid line is their sum [54]. 33

2.5 The high-energy γ-ray spectrum measured with BaF_2 detectors and Doppler corrected with the velocity of the projectile. The lines are the statistical model calculations for the target (dotted line) and for the beam (dashed line) nuclei. In the inset the continuous line superimposed to the measured data is the result of a GEANT simulation for a γ transition at 11 MeV [55]. 33

2.6 (a) Cross sections for the excitation of $J^\pi = 1^-$ in ^{124}Sn deduced from the (α,α' γ) experiment. (b) The B(E1) strength distribution, obtained in (γ, γ') experiment [8][58]. 35

2.7 (a) Singles cross section for the excitation of the J^π=1^- states in ^{124}Sn obtained in the (α,α' γ) coincidence experiment. (b) B(E1) strength distribution measured with the (γ,γ') reaction. The middle column shows the QPM transition probabilities in ^{124}Sn for the isoscalar (c) and electromagnetic (d) dipole operators. The RQTBA strength functions in ^{124}Sn for the isoscalar and electromagnetic dipole operators are shown in (e) and (f), respectively [59]. 36

2.8 Differential cross sections measured in the ^{124}Sn(^{17}O,^{17}O$'\gamma$) experiment, corresponding to the discrete lines integrated in two regions 5–7 and 7–9 MeV (top panel). For comparison, the corresponding strengths measured in α-scattering (middle panel) [58] and photon-scattering (bottom panel) [8] are plotted. Figure taken from [3]. . . 37

2.9 The Doppler-corrected γ-ray spectra: ^{20}O + α singles (a), ^{20}O + α, detected in coincidence with the 2_1^+ state (1.67 MeV) (b), ^{20}O + Au singles (c), ^{20}O + Au, detected in coincidence with the 2_1^+ state (d). The grey histograms are the background spectra. The grey error bars are statistical[63]. 38

3.1 Computed cross sections for the population of various excitation modes in the reaction ^{68}Ni+^{12}C as a function of the beam energy (AMeV) in the laboratory frame. 40
3.2 A sketch not to scale of the used experimental set up. 41
3.3 Map of the INFN-LNS. In this map the fragment separator (LNS-FRS), placed at the exit of the CS, is evident. The two dipoles, at 45° with respect to the beam line, are used to perform the selection of the fragments. Also the position of the ^{9}Be target is indicated in the map. In the upper inset a photo of the ^{9}Be target support is shown. 43
3.4 In figure the standard layout of the fragment separator is shown. . 45
3.5 Scheme, not to scale, of the tagging system. 47
3.6 Left: Photo of the MCP detector mounted on a ISO-flange. Right: Photo of the DSSSD. 48
3.7 ΔE-ToF plots obtained during the test selecting the several charge states. 49
3.8 ΔE-ToF plots obtained during the Pygmy experiment selecting different charge states. 50
3.9 LISE++ simulation [74] obtained considering the energy loss on the DSSSD. In this simulation it is possible to see several nuclei, produced in the reaction ^{70}Zn + ^{9}Be. 51
3.10 Left: ΔE-ToF plot obtained in the first part of the experiment. Right: ΔE-ToF plot obtained in the last part of the experiment. 52
3.11 Gaussian fits on the cuts shown in Fig. 3.10 for the ^{68}Ni (red histograms) and for the ^{69}Cu (green histograms) The (a)-(b) panels correspond to the first part of the experiment while the (c)-(d) ones correspond to the last part of the experiment. 53
3.12 (a)-(b) Energy and time calibration of a strip for the first part of the experiment. (c)-(d) Energy and time calibration of a strip for the last part of the experiment. 54
3.13 ΔE-ToF calibrated plot obtained with the tagging system. 55

3.14 Left: Photo of the PPAC detector mounted close to the CHIMERA sphere. Right: Beam trajectory obtained during the experiment, it is possible to clearly see the several wires of the PPAC detector. 56

4.1 The basic detection telescope of the CHIMERA multidetector. . . . 58
4.2 Photo of the CHIMERA multidetector placed at INFN-LNS. 58
4.3 Photo of the CHIMERA sphere. 59
4.4 Scheme of the CHIMERA multidetector. 59
4.5 Typical cross-sectional view of a passivated ion implanted silicon detector with a guard ring surrounding the active area [76]. 62
4.6 Not to scale scheme of a silicon detector belonging to the rings of the CHIMERA array. Green: fiberglass support. Azure-blue: detector active areas. Grey: guard ring. Red and Blue: electrical contacts [80]. 63
4.7 (a) Photo of the Si detectors of the CHIMERA sphere (b) schematic view of the Si detectors of the sphere [76]. 64
4.8 Photo of the motherboards placed on the external surface of the wheels mechanical structure (left) and on the top of the metallic baskets for sphere detectors (right)[76]. 66
4.9 Top: Scheme of the electronic chain for the silicon detectors in rings 1-3 and 14-26. Amplifiers and CFDs are CAMAC modules. Bottom: Scheme of the electronic chain for silicon detectors in rings 4-13. For these detectors it is possible also to extract the rise-time information. The main component of this electronic chain is constituted by a module NIM1568B. It provides an amplified energy signal, a multiplicity signal and two logic signals corresponding to the instants when the signal overcomes 30% and 80% of its peak value. 68
4.10 Sketch of the electronic chain used for the CsI(Tl) signals. The used amplifiers have NIM standard, and are manufactured by SILENA, they manage 16 channels. The stretchers are also NIM based modules. The QDCs are VME modules treating 64 channels with a common gate. 71
4.11 ΔE-E plot obtained with the CHIMERA multidetector [80]. 74
4.12 E-Rise Time plot obtained with the CHIMERA multidetector [80]. . 74
4.13 ΔE-ToF plot obtained with the CHIMERA multidetector [80]. 75
4.14 Fast-Slow identification plot obtained with the CHIMERA multidetector [80]. 75

4.15 Scheme of treatment of Fast and Slow components using the two gate method. 77
4.16 Fast–Slow identification scatter plot obtained for one crystal, located at θ= 13.75 ° of the CHIMERA array, in the reaction ^{124}Sn+ ^{64}Ni at 35 MeV/A. The insets show expanded portions of the scatter plot [84]. 77
4.17 Sketch of the slow gate timing. The "event accepted" signal, produced by the trigger, enables one RF signal. This signal is used as reference time to generate all gates. The dashed region shows the slow integration region of a signal, produced by a good coincidence. One can note the difference with the charge, integrated with the same gate, for a signal produced in a different burst (dashed signal that corresponds to spurious coincidence) [84]. 78
4.18 Fast–Slow identification scatter plot for a detector located at θ=1.4°. The observed lines with constant value of the fast component are due to spurious coincidences in different beam bursts. As can be seen in Fig. 4.17 the variation in the slow signal is due to the dependence of the position of the slow gate on the RF signal [84]. The vertical line corresponds to the case in which the gate is randomly sampling the fast signals at the edge of the flat/stretched part. . . . 79
4.19 Left: fast-slow obtained in the Pygmy experiment, Right: the same fast-slow in which we plot also the identification lines to show the identification procedure. 81
4.20 Fast-slow for CsI(Tl) detectors in the telescope 511 (covered by FARCOS) and 515 (not covered by FARCOS)[102]. 83
4.21 Comparison among MCNPX [103] and experimental energy spectra of light charged particles detected in the CHIMERA CsI(Tl) detectors in the shadow of FARCOS [102]. 84
4.22 Left: ΔE-E plot obtained for a telescope of the CHIMERA sphere in the p + ^{12}C reaction at 24 MeV. Right: Projection on the fast (E) axis, shown in the left panel, with the Gaussian fit performed on each bump. 85
4.23 Linear calibration for protons, obtained for a telescope of the CHIMERA sphere. 85

4.24 a) Q-value spectrum for the p + ^{12}C reaction. The elastic (green) and the inelastic peaks (yellow) are well separated. b) Energy spectra of γ-rays detected with the CsI(Tl) of CHIMERA, in coincidence with the inelastic (yellow peak) and the elastic channel (green peak) of the p + ^{12}C reaction. c) Energy spectra of γ-rays detected with the CHIMERA CsI(Tl), resulting from the subtraction of the two γ-ray spectra shown in panel b). d) γ- ray angular distribution for decay of the 4.44 MeV level. 86
4.25 Mechanical draw of the BB7 silicon strip detectors used for the FARCOS prototype. 89
4.26 Left: the image shows one of the FARCOS telescope assembled. Right: the image shows the components of each telescope [118]. . . 89
4.27 Copper block placed behind each telescope, in order to support and cool the four CsI(Tl) preamplifiers. 90
4.28 Left: Mechanical support used for the FARCOS prototype, composed by four telescopes. Right: photo of the support with the mounted four telescopes. 90
4.29 Simulation, performed with SRIM [119], of the energy loss ΔE against the total energy E_{tot} of nickel isotopes in the first two stages of a FARCOS telescope. In the inset the preliminary mass estimation for the ^{67}Ni, ^{68}Ni, ^{69}Ni is shown. 92
4.30 ΔE-E simulation of the energy loss in the first two stages of a FARCOS telescope, performed with LISE++ taking into account the envelop of beams. However, in this simulation we have not included the dipole after the MCP detector. 93
4.31 ΔE-E plot obtained with the FARCOS array, considering two correlated strips. 94

5.1 (a) ΔE-E scatter plot observed with the FARCOS array, irradiated by the reaction products produced with the whole fragmentation beam. The isotopic identification of fragments with Z from 27 to 30 is observed. In the inset the ΔE-ToF identification scatter plot of the cocktail beam is shown. (b) Reaction products detected with the FARCOS array in coincidence with ^{68}Ni^{28+} ions, as shown in the black circle in the inset of Fig. 5.1(a). 97

5.2 (a) ΔE-E plot obtained with FARCOS in coincidence with the $^{68}Ni^{28+}$ beam, detected with the tagging system. (b) Energy γ-spectrum obtained in coincidence with Ni fragments, inside the black ellipse in Fig. 5.2 (a). The blue spectrum corresponds to γ-rays correctly identified while the red one corresponds to spurious coincidences. . . . 98
5.3 (a) Blue dots: energy γ-spectrum, Doppler shift corrected, obtained with the subtraction of the two spectra plotted in Fig. 5.2 (b). The blue dashed curve corresponds to standard statistical calculations, obtained considering the statistical decay of the ^{68}Ni nucleus populated with a range of excitation energies peaked at 26.5 MeV. The red full curve corresponds to CASCADE calculations, obtained including the presence of PDR, GDR and GQR. (b) CASCADE calculations obtained including the PDR, the GDR and the GQR without the folding with the detector response. 99
5.4 (a) γ-rays energy spectra Doppler shift corrected. The blue dots represent the coincidence with ^{68}Ni. The red squares represent the γ-rays energy spectrum in coincidence with ^{66,67}Ni. These spectra have been normalized at the low energy region. The blue full line is the γ-rays first step spectrum obtained with CASCADE. (b) Cross section of the PDR obtained considering the difference of the two spectra shown in Fig. 5.4 (a). 102
5.5 (a) The measured γ-rays angular distribution. The line is the expected E1 angular distribution. (b) The ^{68}Ni angular distribution measured in coincidence with γ-rays in the region of the Pygmy resonance. 103
5.6 Energy γ spectrum without Doppler correction (red) and energy γ spectrum Doppler shift corrected (green). 105
5.7 The curves represent CASCADE calculations obtained at several excitation energies up to 28 MeV. The blue dots represent the γ-rays energy spectrum in coincidence with Ni fragments. 106
5.8 CASCADE calculations obtained with a standard CASCADE calculation (black curve), including the GQR contribution (green curve), including the PDR+GDR contributions (violet curve) and including the PDR+GDR+GQR contributions (red curve). 108

5.9 Energy γ spectrum obtained in coincidence with the ^{68}Ni beam and with the ^{68}Ni fragment. The blue dashed curve corresponds to the CASCADE calculation considering the statistical decay of the ^{68}Ni, while the blue full line corresponds to the first step CASCADE calculation. 109
5.10 Geometry of the CHIMERA multidetector as used for the GEANT4 simulations. Also the Si detectors of the FARCOS array, placed after the CHIMERA multidetector sphere are visible. The Si detectors of the FARCOS array are better seen in the inset, where we plot a zoom of that region. 110
5.11 Energy γ-rays spectra simulated with GEANT4 in order to extract the detection efficiency around 10 MeV. 110
5.12 Detection efficiency obtained with GEANT4 simulations for γ-rays of about 10 MeV as a function of the thickness (left) and θ_{LAB} (right). 111
5.13 Detection efficiency obtained with GEANT4 as a function of the γ-energy for the ring 10 at $\theta_{LAB} \approx 30$ °. 111
5.14 γ-rays energy spectrum obtained with GEANT4 at $\theta_{LAB} \approx 30°$. Each colored region corresponds to the region in which we performed the integral to obtain the folding of CASCADE calculations. 113
5.15 Fits on the Pygmy Dipole Resonance bump obtained with the subtraction (a) and the ratio (b) between the ^{68}Ni channel and the ^{66,67}Ni. 113
5.16 (a) Results obtained in ref. [55], (b) results obtained in our experiment, (c) results obtained in ref. [44]. 114
5.17 In the figure two fast-slow plots are shown, for a telescope not covered (a) by the FARCOS array and for a telescope covered (b) by the FARCOS array. 117
5.18 Fast-slow for a telescope of the CHIMERA array covered by FARCOS. In the figure also the charged particles region (blue ellipse), produced by neutrons interaction, is shown. 117
5.19 θ relative angle obtained performing the coincidence between the neutrons, detected with the CHIMERA array, and ^{67}Ni detected with FARCOS. 118
5.20 θ relative angle simulated with Phase Space [131]. 119
5.21 Schematic view of the INFN-LNS beam lines and halls. The position of the actual fragment separator and of the new one, FraISe, are indicated by circles [66]. 120
5.22 Schematic view of FraISe [66]. 120

5.23 Expected yield with the new fragment separator FraISe [66]. 121

Introduction

Collective excitations are a common feature of the atomic nuclei. The most important among them are the so called Giant Resonances which, in a macroscopic interpretation, are seen as coherent oscillation of many nucleons. By studying the characteristics of such collective modes different information have been learned about the properties of the nuclear matter, as the compression modulus and the symmetry energy.
The first Giant Resonance, the Giant Dipole Resonance (GDR), was discovered more than 70 years ago. The observed photonuclear cross section in the energy range of the GDR exhausts nearly the 100 % of the sum rule for isovector electric dipole (E1) transitions. The GDR is usually described, macroscopically, as an oscillation of all protons against all neutrons of the nucleus. A systematic study of its properties began around the 1950. Subsequently, with the development of cyclotron and linear accelerators, as well as with the increasing of experimental techniques, other modes were found and studied in detail.
In particular, during the 60's, experimental investigations showed an accumulation of the γ-rays E1 strength around the nucleon binding energy in several isotopes. This accumulation of low-lying dipole strengths has been called Pygmy Dipole Resonance (PDR) for the smaller strength, about 5-10 % of the sum rule, in comparison with the GDR one. Several investigations provided that such accumulation of low-lying dipole states was connected to the neutron excess in nuclei and its strength was more intense in nuclei far from the stability line with respect to the stable ones.
The understanding of the low-lying E1 states around the nucleon binding energy is attracting considerable interest also for the strong relation with the neutron skin and with the symmetry energy of the equation of state (EoS). Indeed, from the PDR strength it is possible to estimate the size of the neutron skin and to constrain the symmetry energy. One of the major task of experimental and theoretical investigations is to determine a consistent density parametrization of the symmetry energy which can provide a unified picture of nuclear properties. Indeed through the symmetry energy quantity several features of the atomic nuclei as well as of

the neutron stars can be obtained. Furthermore, the PDR might have an influence also on the astrophysical r-process, responsible for the nucleosynthesis of elements heavier than iron, in fact the presence of a dipole strength around the neutron separation energy strongly enhances the neutron capture cross section. In this framework, a better knowledge of the PDR properties could provide a link to understand the neutron stars (with radius $\approx 10^4$ m) starting from the study of the neutron skin in nuclei (with radius $\approx 10^{-15}$ m), and it could provide useful information in the present multimessenger era.
The interpretation of the structure of the low-energy E1 strength, in particular the degree of collectivity, in almost all nuclei with a neutron excess is still under debate. Indeed, there are several approaches able to describe the Pygmy resonance. Considering a macroscopic interpretation, the Pygmy resonance can be associated to the vibration of the neutron skin against a saturated core with the same number of protons and neutrons. On the other hand, the several microscopic interpretations based on many body theory allow to study deeply inside the structure of such modes. These theoretical calculations are all in agreement on the main characteristics of the low-lying states, for instance the fact that such states are originated in nuclei with a neutron excess.
One of the most important feature of the PDR is the behavior of the transition densities: the proton and neutron transition densities are in phase inside the nucleus, while at the surface just the neutron contribution is present. This confirms that such modes are linked to the neutron excess in nuclei. Moreover, the isoscalar and isovector part of the transition density at the surface have the same order of magnitude and shape. Such characteristic denotes the mixing of the isovector and isoscalar character of the mode, that therefore can be populated by both isoscalar and isovector probes.
From the experimental point of view, the PDR has been investigated in a large number of stable nuclei, below the neutron emission threshold, with the photo scattering technique and with isoscalar probes, namely using $(\alpha,\alpha'\gamma)$ and $(^{17}O,^{17}O'\gamma)$ experiments. The comparison between these investigations reveals that only a group of states, belonging to an energy range approximately between 4 and 6 MeV, is excited by both isoscalar and isovector probes, whereas another group, at energies higher than the previous one, is populated only using the electromagnetic interaction. This phenomenon, called "isospin splitting" or "isospin mixing", is evident in all the stable nuclei analyzed and it is currently a topic of interest due to the fact that its nature has to be well understood.

The investigation of the PDR in unstable nuclei was carried out in pioneering experiments performed at the GSI, using isovector probes, namely relativistic Coulomb excitation with natural targets of Pb and Au. Recently, the low-lying strength was also investigated in the unstable nucleus ^{20}O, using both isovector and isoscalar probes, below the neutron separation threshold.
In order to better understand the nature of the Pygmy Dipole Resonance and to verify if the isospin splitting is a common feature of such low-lying mode, it is necessary to measure the PDR using several probes, in different mass regions and in particular at energy above the neutron emission threshold.
At the Laboratori Nazionali del Sud (LNS)- INFN we performed an experiment, aimed to study for the first time the Pygmy decay in the ^{68}Ni at 28A MeV, above the neutron emission threshold, using an isoscalar probe, namely a natural carbon target of ^{12}C. A ^{70}Zn primary beam was accelerated to an energy of 40A MeV, using the Superconducting Cyclotron (CS) of the INFN-LNS, and it impinged on a 250 μm thick ^{9}Be target to produce, with a projectile fragmentation reaction, the ^{68}Ni beam, delivered via the FRIBs@LNS fragment separator of the INFN-LNS.
The ^{68}Ni + ^{12}C reaction permits to investigate the isoscalar excitation of the PDR as it is also confirmed by semiclassical calculations. Such calculations, based on microscopic form factors built with microscopic RPA transition densities showed that, at 28A MeV, most of the total inelastic PDR cross section, (almost the 60 %) is due to the pure nuclear interaction. The Coulomb contribution amounts to 9 %, while the 30 % is given by the interference between nuclear and Coulomb contributions.
The γ-decay channel of the PDR was studied using the 4π CHIMERA multidetector, while the scattered ^{68}Ni ions were detected and identified in four prototype telescopes of the FARCOS array. Moreover, we present also some preliminary results about the neutron decay of the Pygmy Dipole Resonance.
In summary, the thesis is based on the experimental study of some of properties of the so called Pygmy Dipole Resonance for the exotic isotope ^{68}Ni. The investigation has been carried out using an isoscalar probe, which has been proved to be a useful mean for the study of these modes by theoretical calculations as well as previous experimental works. The comparison with previous experimental results obtained by using an isovector probe has shown that there are no important differences between the two. This might confirm the theoretical expectation that in the mode there is a strong mixing of isovector and isoscalar characteristics. On the other hand, due to the limits of the relative small statistics and relative scarce energy resolution of the present measurements, it is not possible to draw definite

conclusions about the presence of isospin splitting for the PDR at energies above the neutron emission threshold. Further experiments with the same experimental apparatus are necessary in order to enlighten this question.
The thesis is organized in the following way: we introduce in Chapter 1 the theoretical approaches to the physics case, in Chapter 2 the main experimental findings about the low-lying dipole strength and the experimental methods used to study the PDR are described. In Chapter 3 we introduce the experimental set up and the production of the exotic beam. In this Chapter we report also the results obtained with the semiclassical calculations. Moreover, we discuss the data analysis relative to the selection of the $^{68}Ni^{28+}$. In Chapter 4 we describe the CHIMERA and the FARCOS array, and we discuss the methods used to detect γ-rays and neutrons. In this Chapter we report also the data analysis relative to the calibration of the CHIMERA multidetector. In Chapter 5 we report the results and the discussion about the γ-decay channel of the PDR and the preliminary results about the neutron decay channel of the PDR.

Chapter 1

General features of the Pygmy Dipole Resonance

In this Chapter we report the introduction to the physics case for the study of the Pygmy Dipole Resonance (PDR) and we discuss the main theoretical aspects, that are relevant for the investigation of these low-energy dipole modes. Moreover, we present also some experimental results, related to the main theoretical works. In this Chapter we recall four main papers [1–4].

1.1 History of the Pygmy modes

Recently, much relevance has been given to the collective states in neutron-rich nuclei. The study of collective states indeed allows to understand the nuclear structure, the effective nucleon-nucleon interaction, the bulk properties of the nuclear matter, as the compression modulus and the symmetry energy. The remarkable interest in these states is also driven by the presence of an electric dipole response around the nucleon binding energy [1–3]. This excitation mode, known as Pygmy Dipole Resonance (PDR), carries few per cent of the Energy-Weighted Sum Rule (EWSR) and several theoretical models predict its presence for almost all stable and unstable neutron rich nuclei.
The history of the PDR started in the 60's, when G. A. Bartholomew presented in a paper [5] a systematic theoretical and experimental study concerned with the nature of the neutron capture γ-rays. In this paper was pointed out the observation of an enhancement of the γ-rays strength around 5-7 MeV in many isotopes. J.S. Brzosko et al., in their manuscript titled *"Effect of the pigmy resonance on the calculations of the neutron capture cross section"* [6], reported a comparison between the experimental cross sections of the (n,γ) reaction for several nuclei (^{103}Rh, ^{127}I, ^{181}Ta, ^{197}Au) with a theoretical model. In their model, they studied the influence

of a E1 resonance, located at an energy of $E_\gamma \approx 6$ MeV, and they coined for the first time the term "pigmy resonance", to indicate this "new" E1 resonance. They underlined that the agreement with the experimental values was better in the case in which the "pigmy resonance" was included in their calculations, as it is possible to note in Fig. 1.1.

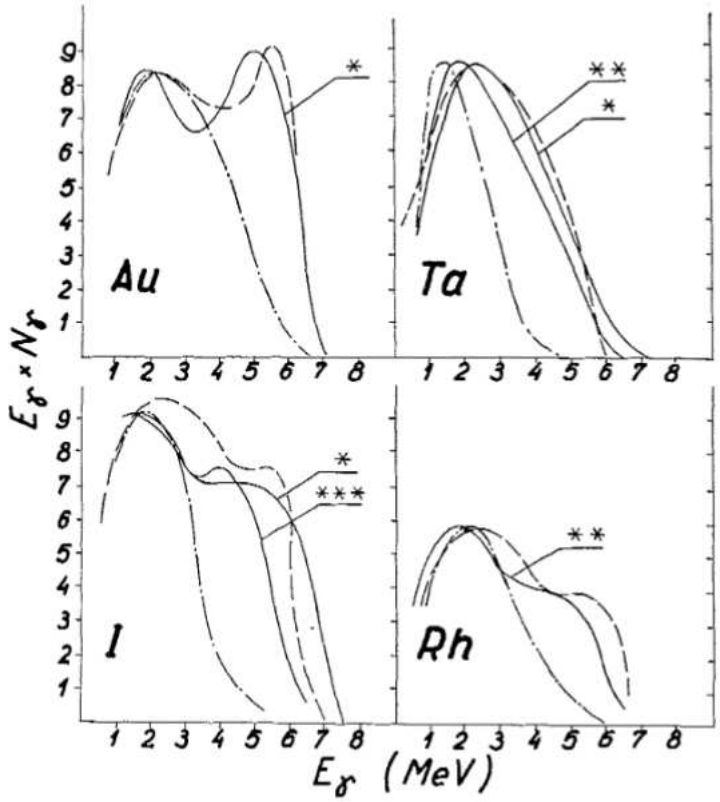

FIGURE 1.1: Comparison of the measured (solid curves) and calculated spectra of the neutron capture γ-rays. The dashed curves present the results of calculations when both giant and pigmy resonance are accounted for. The dashed-dotted curves give results of calculations in which no account was taken for the pigmy resonance[6].

In 1971 R. Mohan et al. [7] gave a theoretical interpretation of this mode. They introduced a three-fluid model of nuclei, in which the three fluids are the protons, the neutrons of the same orbitals as protons, and the neutron excess. This lead to two independent electric dipole resonances. The first one due to the oscillation of all protons against all neutrons and the second one, energetically lower, where only the neutron excess oscillates against a saturated core, in which protons and neutrons are in the same orbitals. In this manuscript R. Mohan et al. [7] estimated that the neutron-proton strength was more of two orders of magnitude stronger than the strength of neutrons against the saturated core. This is in agreement with

the currently idea for which the low-lying energy modes may be associated to the oscillation of neutron excess against a saturated core.
K. Govaert at al. [8] carried out one of the first high resolution Nuclear Resonance Fluorescence (NRF) experiment. The several methods, used to investigate the PDR, will be recalled in detail in the Chapter 2. Subsequently, several NRF experiments were carried out on the photo-response of nuclei, in the region of the particle emission threshold [1]. Moreover, with the advent of high-energy radioactive beams, several studies were performed in order to study the properties of this mode in reaction experiments.
Tanihata et al. [9, 10] used secondary heavy-ion beams to measure the interaction cross sections of light neutron-rich nuclei. They observed large cross sections for nuclei located at the neutron drip line, as the ^{11}Li, implying a large radius. Also for these nuclei a small dipole strength was found at very low energies, and sometimes this strength is also called pygmy resonance.
In the 1987 Hansen and Jonson [11] gave the interpretation that the large radius, linked to the large observed cross section, was related to the spatial extension of the wave function of the weakly bound neutrons, extending far beyond the nuclear mean field, and they coined the name "neutron halo". Nowadays, it is known that in the halo nuclei the low-energy dipole strength is of non-resonant character and it is related to the single-particle excitations of the loosely bound neutrons. However, these investigations have triggered the idea that a vibrational mode of loosely bound neutrons against a saturated core might appear and might be observable in neutron rich nuclei. The study performed on Oxygen isotopes, using Coulomb excitation, revealed that the low-energy dipole strength can not be explained just considering a single-particle excitation, as in the case of ^{11}Be, implying an excitation neutron excess -core [12, 13]. An intense experimental and theoretical investigation has then started in the nineties to understand the dipole response of neutron-rich nuclei. The numerous experiments have employed both Coulomb and Hadronic excitations, in both stable and unstable nuclei [1–3], as better specified in the Chapter 2. The use of both Coulomb and Hadronic excitations is justified by microscopic calculations and can be explained studying the transition densities of low-lying modes, as will be discussed in the following sections.
These investigations have shown that the dipole strength related to the excitation of excess neutrons is completely decoupled from the Giant Dipole Resonance (GDR) and it is located close to the neutron separation threshold, it is in this sense Pygmy Dipole Strength (PDS) or Pygmy Dipole Resonance (PDR). Despite of the innumerable theoretical and experimental efforts, the knowledge about the nature

of the PDR is still not conclusive.

1.2 Theoretical approach

The interpretation of the structure of the low-energy E1 strength in almost all nuclei with a neutron excess is currently under discussion. Indeed, while the main features of the E1 response, mainly dominated by the Isovector Giant Dipole Resonance (IVGDR), are reproduced quite consistently in many models, the energetically low-lying part of the E1 strength often differs between calculations, since it is much more dependent on the details of the nuclear force and theoretical models. For these reasons, the systematic of the low-lying E1 strength is a matter of on going discussions and there are several approaches to study these low-lying states [1]. In ref. [2] it is possible to find a detailed and complete description of the theoretical approaches. In this section we report just a brief overview, with a particular attention for the ^{68}Ni results, reported in ref. [4].
For spherical and closed shell nuclei the use of the Hartree-Fock (HF) method combined with the Random Phase Approximation (RPA) is the most appropriate tool [14–18]. For open shell and deformed nuclei the use of Hartree-Fock-Bogoliubov method with Quasi-Particle RPA is employed for the description of the PDR [19, 20]. Extensions of particle-hole approaches, taking into account two-particle - two-hole contributions, like the second RPA approach [21, 22], and the coupling to two or three-phonons configurations, like the Extended Theory of finite Fermi Systems (ETFFS) [23] or the Quasi-particle Phonon Model (QPM), which takes into account explicitly the coupling between nucleons and phonons [24], have been used in the description of the low-lying dipole states. Relativistic mean-field theory, like RRPA [25–27] or the RQRPA [28–30], give also a good description of the properties of nuclei. A good description of the PDR features is obtained also within the Relativistic Quasi-particle Time Blocking Approximation (RQTBA) [31].

All these calculations coincide on the main characteristic of the low-lying states, namely the fact that such states are originated in nuclei with a neutron excess. Moreover, the strength of this mode is more intense in the exotic neutron-rich nuclei with respect to the stable ones. Furthermore, in neutron poor nuclei a PDR correlated to a proton skin has been predicted [32].
As an example, in a pioneering theoretical work [14] it has been shown that, as soon as the number of neutrons increases, the isovector and isoscalar dipole responses show a small bump at low energy in the strength distribution, which is

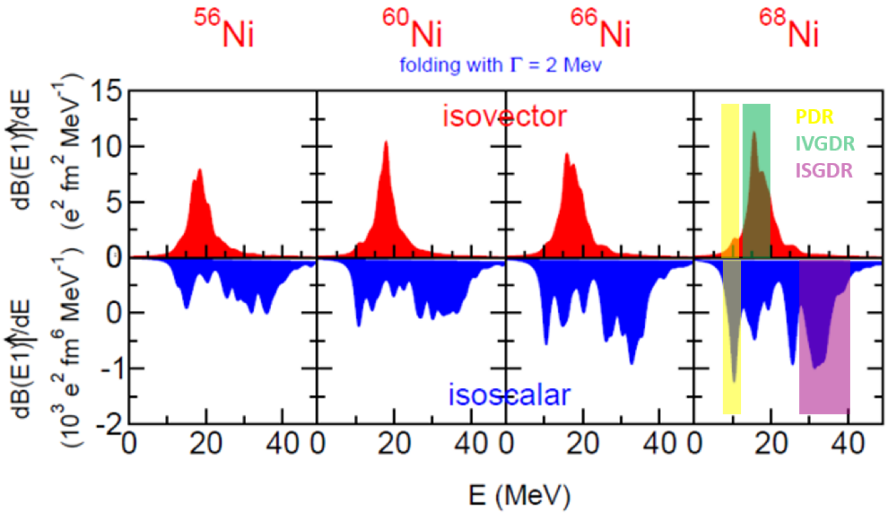

FIGURE 1.2: RPA strength distributions for isovector (upper) and isoscalar (lower) response for Ni isotopes.

well separated from the well known peak of the GDR.

In Fig. 1.2 it is shown the predicted dipole response to an isovector (upper panels) and isoscalar (lower panels) probe for Ni isotopes. These strengths were obtained performing an HF plus RPA calculation. The curves are generated by a smoothing procedure, using a Lorentzian with a 2 MeV width. In the figure it is possible to observe that, as soon as the neutrons number increases, a small peak, at around 10 MeV, becomes evident in the isovector dipole response and it is clearly discernible for the ^{68}Ni isotope. We note this trend also in the lower panel, where the isoscalar response is plotted. These calculations have been obtained considering the operators for the isovector response (IV) and isoscalar response (IS) given by :

$$O_{1M}^{(IV)} = 2\frac{Z}{A}\sum_{n=1}^{N} r_n Y_{1M}(\hat{r}_n) - 2\frac{N}{A}\sum_{p=1}^{Z} r_p Y_{1M}(\hat{r}_p) \tag{1.1}$$

$$O_{1M}^{(IS)} = \sum_{i=1}^{A}(r_1^3 - \frac{5}{3}\langle r^2\rangle r_i) Y_{1M}(\hat{r}_i) \tag{1.2}$$

In the Fig. 1.2 the peaks, shown in the two panels, at different excitation energies, are related to different excitation modes, as can be evidenced by studying the different structure of their transition densities. Looking at the ^{68}Ni case, the small bump at around 10 MeV corresponds to the PDR excitation. This confirms that the PDR is linked to the neutron excess and it is present in both isoscalar and isovector

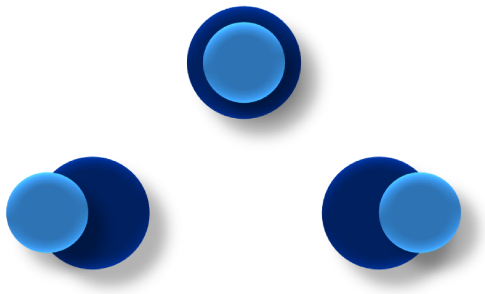

FIGURE 1.3: Schematic representation of the PDR state generated as an oscillation of the core against the neutron skin.

responses. Therefore, considering that a nucleus with a neutron excess is made of a saturated core (in which neutrons and protons sit in the same orbitals), and a neutron skin, then the PDR can be considered as a surface mode corresponding to an out of phase oscillation of the core against the neutron skin, which is formed by the neutron excess, as shown in Fig. 1.3.
Indeed, it is possible to study the PDR mode also using a Macroscopic Pygmy Model (MPM) [4]. In this model the density is the sum of three terms:

$$\rho(r) = \rho_p(r) + \rho_n^c(r) + \rho_n^s(r) \tag{1.3}$$

where c and s indicate the core and the skin, respectively. The neutron and proton transition densities are defined by:

$$\delta\rho_n(r) = \delta\left[\frac{N_S}{A}\frac{d\rho_n^c(r)}{dr} - \frac{N_c+Z}{A}\frac{d\rho_n^S(r)}{dr}\right] \tag{1.4}$$

$$\delta\rho_p(r) = \delta\left[\frac{N_S}{A}\frac{d\rho_p(r)}{dr}\right] \tag{1.5}$$

Starting from these transition densities one can construct the isoscalar and isovector transition densities (we omit, for simplicity, the r dependence):

$$\delta\rho_{is} = \delta\left[\frac{N_S}{A}\frac{d\left(\rho_n^c+\rho_p\right)}{dr} - \frac{N_c+Z}{A}\frac{d\rho_n^S}{dr}\right] \tag{1.6}$$

$$\delta\rho_{iv} = \delta\left[\frac{N_S}{A}\frac{d\left(\rho_n^c-\rho_p\right)}{dr} - \frac{N_c+Z}{A}\frac{d\rho_n^S}{dr}\right] \tag{1.7}$$

The neutron core density as well as the neutron skin density can be calculated within the Hartree-Fock (HF) approach, imposing that the core is formed by the

protons and neutrons occupying equal orbitals. In this model it is assumed that the protons are more strongly interacting with the neutrons of the core than with the neutrons of the skin. In the following we report the results for the transition densities, obtained with the MPM model, as well as with other models and the comparison between such models.

1.2.1 Microscopic model for the low-lying dipole states

The Pygmy dipole states are described more precisely using a microscopic model. In this approach the transition densities that commonly one can use are determined with the wave function and the amplitudes coming from a HF plus RPA calculation [4] or their extensions [25, 26, 28, 30].
In general, one can consider a vibrational state, namely an oscillation of the nucleon density around the ground state density $\rho^0(\vec{r})$ [33].
Considering an excited vibrational state $|\nu\rangle$, the corresponding time-dependent wave function is:

$$|\psi(t)\rangle = |0\rangle + c_\nu|\nu\rangle e^{-\frac{iE_\nu t}{\hbar}} \tag{1.8}$$

and the corresponding nuclear density is given by:

$$\rho(\vec{r},t) = \langle\psi(t)|\sum_{i=1}^{A}\delta(\vec{r}-\vec{r}_i)|\psi(t)\rangle = \rho^0(\vec{r}) + \delta\rho(\vec{r},t) \tag{1.9}$$

with

$$\delta\rho(\vec{r},t) = \langle 0|\sum_{i=1}^{A}\delta(\vec{r}-\vec{r}_i)|\nu\rangle e^{-\frac{iE_\nu t}{\hbar}} + c.c. \tag{1.10}$$

The transition density is the time-independent part of $\delta\rho(\vec{r},t)$, that is:

$$\rho^\nu(\vec{r}) = \langle 0|\sum_{i=1}^{A}\delta(\vec{r}-\vec{r}_i)|\nu\rangle \tag{1.11}$$

The transition densities can be used to have information of the structure of a vibrational state, in particular regarding the spatial distribution of the oscillations. In Fig. 1.4 transition densities for the ^{68}Ni are plotted, in the case of the PDR state, predicted at around 10.4 MeV, in the case of Isoscalar Giant Dipole Resonance (ISGDR), which is predicted by the RPA calculation at an excitation energy of E=32.2 MeV, and in the case of IVGDR that is predicted at about E=17 MeV. In particular, the transition densities for protons (black dashed line) and neutrons (red dot-dashed line) as well as the isoscalar (black solid line) and isovector (green

solid line) combinations are shown in the Fig. 1.4.
In the panel (a) the trend shown is typical of the PDR states: the proton and neutron transition densities are in phase inside the nucleus while at the surface only the neutron contribution is present. The tails of the neutron transition densities extend themselves to a larger radius than the proton ones. This behavior suggests also the idea that the PDR could be considered as a surface vibration of the neutron skin against a saturated core. In the same figure (panel (d)), it is possible to note that the isoscalar and isovector part of the transition densities at the surface have the same order of magnitude and the same shape, which denotes mixing of the isovector and isoscalar character of the mode, therefore this mode can be populated by both isoscalar and isovector probes [16]. In Fig. 1.4 (b), one can observe the typical behavior of the isovector GDR with the proton and neutron transition densities out of phase, and thus a strong isovector transition density (panel (e)). This corresponds to the macroscopic picture of the GDR produced by an oscillation of protons against neutrons. In Fig. 1.4 (c) and (f), the characteristic shape of a compressional mode is shown by the transition densities of the ISGDR: the proton and neutron contributions are in phase, giving rise to a strong isoscalar component with a node close to the nuclear radius. In the case of ISGDR another model is able to reproduce such state: the Harakeh-Dieperink (HD) model [34]. This model allows to calculate the corresponding isoscalar transition densities, assuming that the isoscalar dipole Energy Weighted Sum Rule is fully exhausted by a single collective state.

The microscopic, macroscopic, and the HD models allow to extract the transition densities in the case of PDR mode, as shown in Fig. 1.5 [4]. In the figure (a) the isoscalar transition density calculated with the MPM model (blue dot-dashed line) is shown together with the other two iscoscalar transition densities, calculated with the RPA and HD models. In the peripheral region the agreement between the RPA model and the MPM model seems better with respect the HD model. In the figure (b) the transition densities are shown for the isovector mode of the PDR, in this case only the RPA and MPM can be used. In this figure it is also possible to see the good agreement between the two models.
This comparison, as will be also discussed in the following, seems to contain the fundamental characteristics that are important in the definition of the PDR state: a mixing of isoscalar and isovector components, which makes possible the population of the state via both isoscalar and isovector probes.

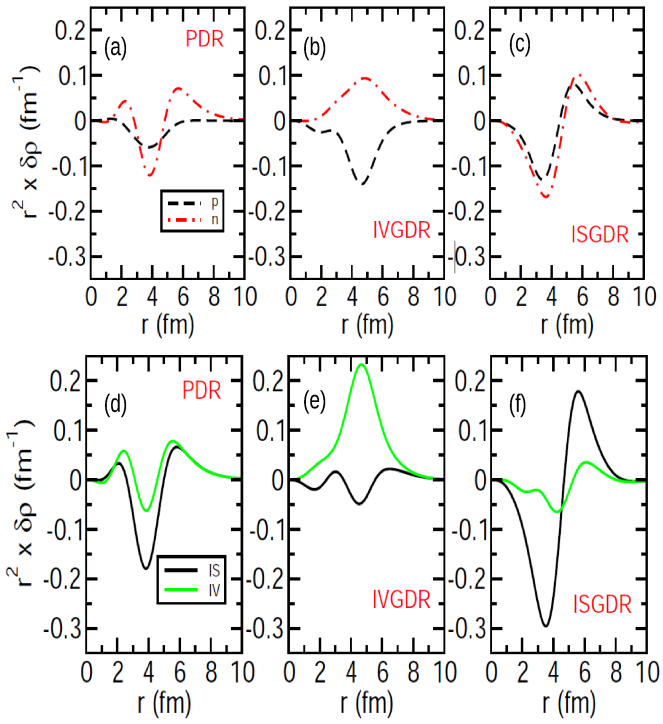

FIGURE 1.4: RPA transition densities calculated for the ^{68}Ni in the case of: the low-lying dipole states (a)-(d), the IVGDR (b)-(e) and the ISGDR (c)-(f). As indicated in the legends the proton, neutron, isoscalar and isovector components are plotted.

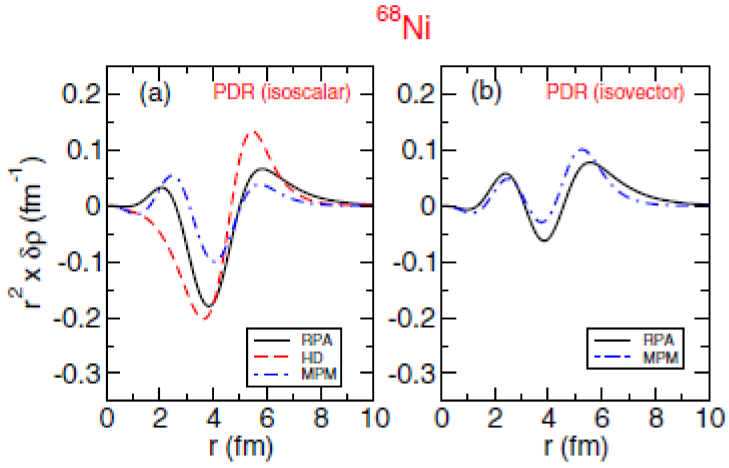

FIGURE 1.5: Comparison among the transition densities calculated with the RPA, HD and MPM models in the case of isoscalar and isovector modes of the PDR [4].

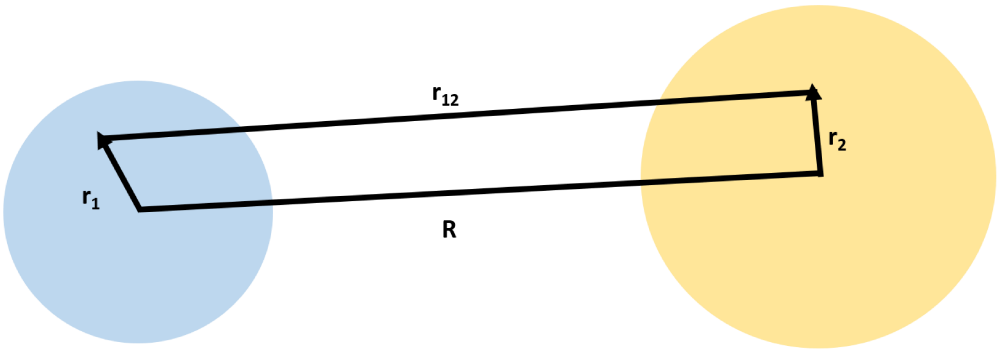

FIGURE 1.6: Schematic representation of the interaction between two nuclei as described by the Eq. 1.13.

1.2.2 Nuclear form factors

In order to extract information about the Pygmy Dipole Resonance and the relative EWSR percentage it is possible to perform Distorted Wave Born Approximation (DWBA) calculations, which depend on the models used for inelastic form factor. These calculations are performed using a complex optical potential. The potential has a real part as well as an imaginary part:

$$U(R) = V(R) + iW(R) \tag{1.12}$$

where V(R) is the real part and W(R) is the imaginary component of this potential. In a heavy ions reaction the nuclear potential is usually given by the so called double folding procedure which consists on performing an integral of the nucleon-nucleon interaction over the nuclear densities of both the projectile and the target nuclei [35, 36].
It can be written as:

$$U(\vec{R}) = \int\int \rho_p(\vec{r_1})\rho_t(\vec{r_2})v(\vec{r}_{12})d\mathbf{r_1}d\mathbf{r_2} \tag{1.13}$$

where the $\rho_p(\vec{r_1})$ and $\rho_t(\vec{r_2})$ are the projectile nuclear density and the target nuclear density respectively, while $v(\vec{r}_{12})$ is the nucleon-nucleon interaction, with $\vec{r_{12}} = \vec{r_2} - \vec{r_1}$, as shown in Fig 1.6. The real part of the optical potential, which together with the Coulomb interaction, determines the classical trajectory, is constructed with the double folding procedure [35, 36]. Taking also the isospin dependent part of the nucleon-nucleon interaction it is possible to write the local effective interaction $v(r_{12})$ as composed by two terms, the isoscalar part v_0 generating an isoscalar ion-ion potential and an isovector term v_1 giving an isospin

dependent folding potential which has an explicit dependence on the difference between the neutron and proton densities. This implies that the neutron-neutron, proton-proton and neutron-proton interactions will be:

$$v_{nn} = v_{pp} = v_0 + v_1, v_{np} = v_0 - v_1. \tag{1.14}$$

Then for the double folding the U(R) potential can be written as:

$$U(\vec{R}) = \int\int [\rho_{p_n}(r_1)\rho_{t_n}(r_2) + \rho_{p_p}(r_1)\rho_{t_p}(r_2)](v_0 + v_1)d\mathbf{r_1}d\mathbf{r_2} + \int\int [\rho_{p_n}(r_1)\rho_{t_p}(r_2) + \rho_{p_p}(r_1)\rho_{t_n}(r_2)](v_0 - v_1)d\mathbf{r_1}d\mathbf{r_2} \tag{1.15}$$

The transition densities are the basic ingredients to construct the nuclear form factors describing nuclear excitation processes. The use of proper form factors, that can be derived either within a macroscopic collective model or in a microscopic approach, is of fundamental importance to deduce these physical quantities. Typically, the form factors in a microscopic approach are calculated within the procedure of double-folding. Indeed, the double-folding potential, between two heavy ions, is obtained by integrating the nucleon-nucleon interaction over the densities of the two nuclei, as in the Eq. 1.15.
In a similar way, the form factors are constructed by using the density of one nucleus on one side and the transition densities of the exited nucleus on the other side. Following the procedure described in ref. [4, 16], in which also the isospin-dependent part of nucleon-nucleon interaction is included, the form factors have two components F_0 and F_1, defined as follows:

$$F_0 = \int\int [\delta\rho_{p_n}(r_1) + \delta\rho_{p_p}(r_1)]v_0(r_{12})[\rho_{t_p}(r_2) + \rho_{t_n}(r_2)]r_1^2 dr_1 r_2^2 dr_2 \tag{1.16}$$

$$F_1 = \int\int [\delta\rho_{p_n}(r_1) - \delta\rho_{p_p}(r_1)]v_1(r_{12})[\rho_{t_n}(r_2) - \rho_{t_p}(r_2)]r_1^2 dr_1 r_2^2 dr_2 \tag{1.17}$$

In particular, the form factor F_1 is zero when we consider reactions in which one or both nuclei have N=Z.
In Fig. 1.7 we plot the form factors obtained in ref. [4] for the ^{68}Ni + ^{12}C reaction. In this figure the form factors obtained with the MPM transition densities (Eq. 1.6, 1.7), the RPA one and also the one obtained with the Harakeh-Dieperink (HD) model are shown. From Fig. 1.7 (a) one can infer that the models generate differ-

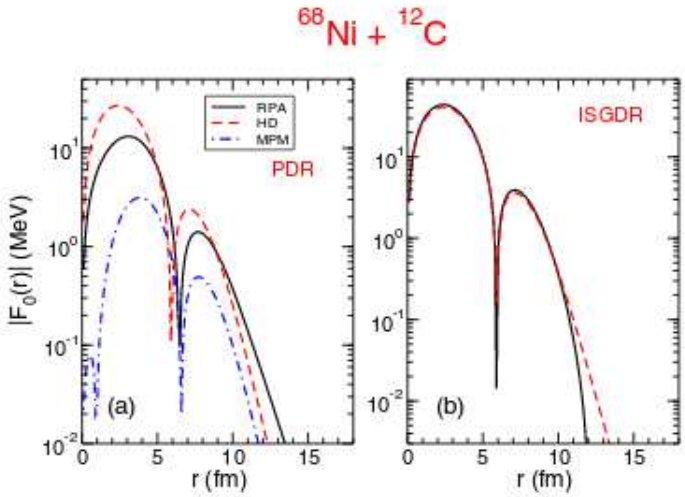

FIGURE 1.7: (a) Form factors for the system ^{68}Ni + ^{12}C for the PDR state. (b) Form factors for the system ^{68}Ni + ^{12}C for the ISGDR state. These form factors are calculated with the RPA, HD and MPM models [4].

ent form factors, this means that these differences have an implication on the cross sections and it is important to construct the correct form factor to extract information on the Pygmy Dipole Resonance parameters. For the ISGDR (panel (b)) the form factors, calculated with the HD and with the RPA method, are identical, with a small difference present just in the peripheral region.

In order to understand the implication of these differences in the evaluation of the cross section, we show in Fig. 1.8 the cross section for the PDR and ISGDR states [4]. As it is possible to observe the cross section for the ISGDR, obtained with the HD model and with the microscopic RPA approach, are almost identical. This result is due to the fact that the ISGDR state is a pure isoscalar state. While, there is not agreement between the cross section for the PDR obtained with the different models (Fig. 1.8 (a)). The difference between the MPM and RPA models, observed in both form factors and cross sections, can be explained considering the different transition densities obtained with these models (Fig. 1.5).

The difference in transition densities, between the two models, arises because in the RPA case transition densities are constructed considering particle-hole configurations, while in the macroscopic approach, transition densities are obtained as derivative of the ground state densities.

The difference obtained with the HD model, in the case of the PDR, means that to extract correct information about the PDR is fundamental to include all the important properties of these states, in particular the strong mixing of isoscalar and

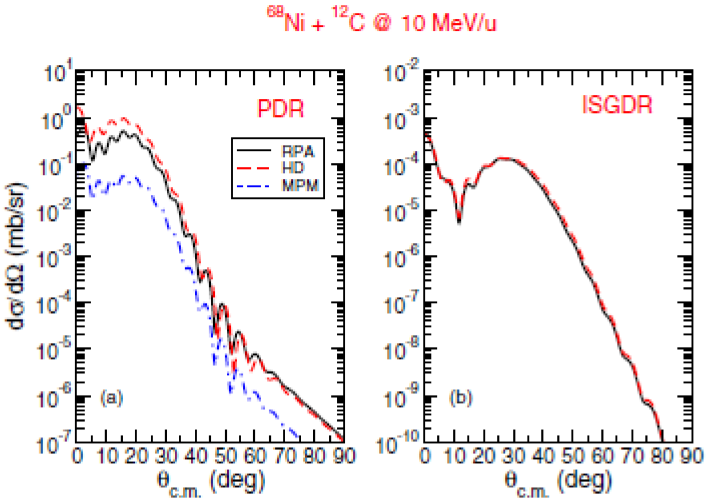

FIGURE 1.8: (a) Differential cross section for the the system ^{68}Ni + ^{12}C for the PDR state. (b) Differential cross section for the system ^{68}Ni + ^{12}C for the ISGDR state [4].

isovector characters.

For completeness, we show in Fig. 1.9 different results obtained with some theoretical models, discussed at the beginning of this Chapter. In the upper panel of this figure we show the E1 strength distribution, for the ^{116}Sn nucleus and for the neutron rich ^{140}Sn nucleus, calculated in the relativistic time blocking approximation (RQTBA) and in the relativistic quasi-particle random-phase approximation (RQRPA) as presented in ref. [37].
In this figure it is possible to note that the low-lying E1 strength is strongly enhanced and shifted to lower energies in the neutron rich ^{140}Sn isotope, showing, also in this case, that such strength increases with larger neutron number.
In the lower part of the figure are plotted the transition densities of the most pronounced low-lying E1 excitations in the RQRPA calculation. For comparison also the corresponding densities of the GDR, at higher excitation energy, are given. Also these models reproduce the main characteristic of the pygmy mode: in the inner part proton and neutron transition densities are very similar and in phase, while at the outer part only the neutron contribution is present, which leads to the interpretation of the neutron-skin oscillation.

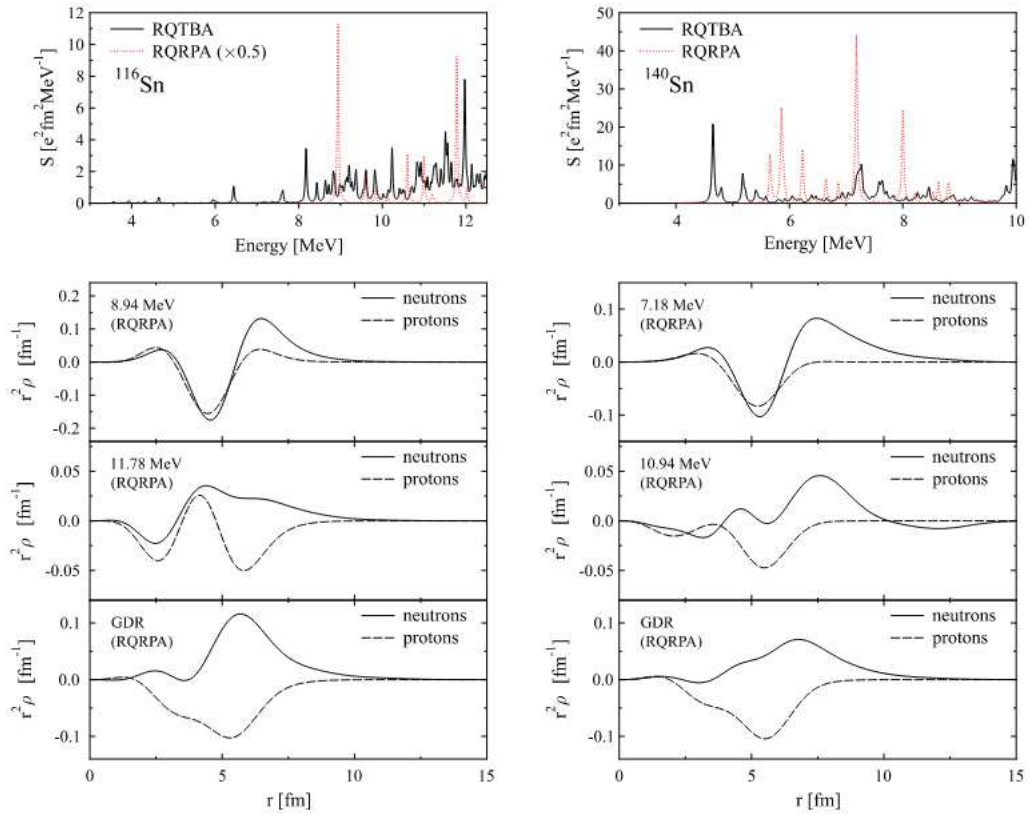

FIGURE 1.9: Upper part: E1 strength distribution calculated, up to 12 MeV for the ^{116}Sn (left) and up to 10 MeV for the ^{140}Sn (right), in RQRPA and RQTBA [37]. Lower part: proton and neutron transition densities corresponding to the most pronounced peaks at low excitation energies at 8.94 MeV and 11.78 MeV for the ^{116}Sn, and 7.18 MeV and 10.94 MeV for the ^{140}Sn, respectively. For comparison the transition densities in the region of the GDR for both nuclei in the RQRPA calculation are also given. Figure taken from ref. [1].

1.3 Link of PDR with the EoS and r-process

There are also two important aspects related with the PDR in nuclei. One is the link of pygmy states to the equation of state of neutron-rich matter and also to objects in the universe such as neutron stars [26, 30, 38]. The other one is the influence of the PDR on reaction rates in the astrophysical r-process which synthesizes approximately 50% of the abundance of the elements heavier than iron [39–41].
In the following sections we recall some theoretical and experimental works to explain more in detail these two important links with the PDR.

1.3.1 Constraints on the symmetry energy and neutron skins from Pygmy Dipole Resonance

The density dependence of the nuclear symmetry energy plays a crucial role in nuclear physics and astrophysics and it is investigated in both theoretical and experimental works. As it is known, the symmetry energy is not an observable which can be directly measured, and it has been typically obtained from complex analyses of multifragmentation reactions. The energy per particle in a nuclear system, characterized by a total density ρ (sum of the neutron and proton densities ρ_n and ρ_p) and by a local asymmetry $\delta = (\rho_n - \rho_p)/\rho$ is usually defined as [42]:

$$\frac{E}{A}(\rho, \delta) = \frac{E}{A}(\rho, \delta = 0) + S(\rho)\delta^2 \tag{1.18}$$

In this equation the so-called symmetry energy is indicated with S(ρ), and the derivative of the symmetry energy at saturation is related to the "slope" parameter L by the equation:

$$S'(\rho)|_{\rho=\rho_0} = \frac{L}{3\rho_0} \tag{1.19}$$

The PDR is connected to the presence of the neutron-skin in neutron rich nuclei, therefore the study of the Pygmy Dipole Resonance could be also important because of the connection with the slope of the symmetry energy. This means that the study of the PDS (Pygmy Dipole Strength) could give important information about these quantities.
As an example, we show in Fig. 1.10 results obtained in ref. [42] in which the authors investigated correlations between the behavior of the nuclear symmetry energy, the neutron skins and the percentage of EWSR in the case of ^{68}Ni and

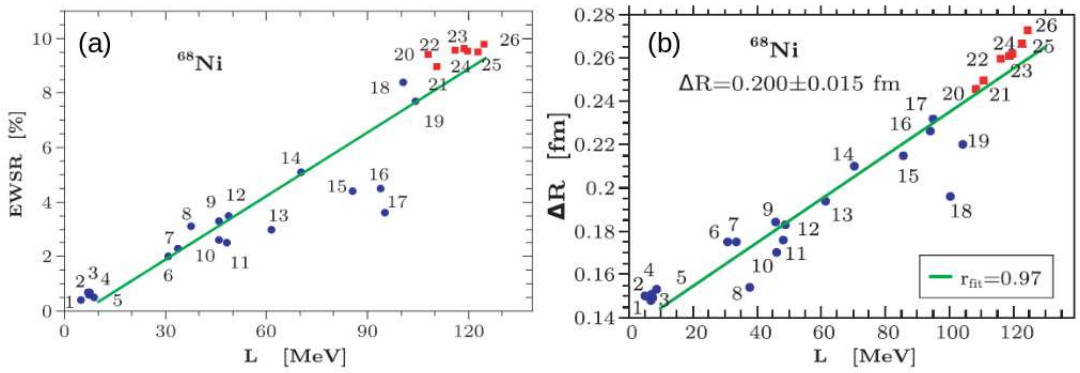

FIGURE 1.10: In the panel (a) the correlation between L and the percentage of sum rule for the PDR in the ^{68}Ni is plotted. In panel (b) the correlation between L and the neutron skin in the ^{68}Ni is shown. The numbers refer to several models used in the calculation [42].

^{132}Sn, using different RPA models for the dipole response. A comparison with experimental data allowed to constrain the value of the derivative of the symmetry energy at the saturation and the neutron skin radius, obtaining a value of the symmetry energy $S(\rho_0) \approx 32.3 \pm 1.3$ MeV and a neutron skin thickness $\approx 0.200 \pm 0.015$ fm for the ^{68}Ni.

This kind of theoretical investigation can be a good tool to add a further constraint to the knowledge of the EoS. However, one has to take into account that each experiment probes different density region. This means that to add relevant information about the EoS and its parameters, a series of studies, probing the behavior of symmetry energy at different densities, should be pursued; the study of Pygmy Dipole Resonance constitutes an important part of these studies. Moreover, when comparing results from different studies, one should not compare just the L parameter, that is, the extrapolation toward the ρ_0 region, but the effective behavior of the symmetry energy in the region of sensitivity of the given study.

Nuclear Dipole Polarizability

From an experimental point of view it is possible to extract the neutron skin of a nucleus as well as the slope of the symmetry energy starting from the study of the electric dipole polarizability. The electric dipole polarizability is indeed an observable directly related to the inverse of the energy-weighted sum rule and, as pointed out by Reinhard and Nazarewicz [43], this observable could provide a more robust and less model dependent observable to extract the neutron skin

$\Delta R_{n,p}$ thickness. This variable was measured for the first time in the ^{68}Ni in ref. [44] and it is defined as follows:

$$\alpha_D = \frac{\hbar c}{2\pi^2} \int_0^\infty \frac{\sigma(E)}{E^2} dE \tag{1.20}$$

Where $\sigma(E)$ is the photo-absorption cross section. In the manuscript of Rossi et al., [44] the authors used the obtained α_D in order to extract values for the $\Delta R_{n,p}$. Indeed, the measured dipole polarizability is compared to relativistic random phase approximation calculations, yielding a neutron-skin thickness of 0.17(2) fm, see also Fig. 1.11 .

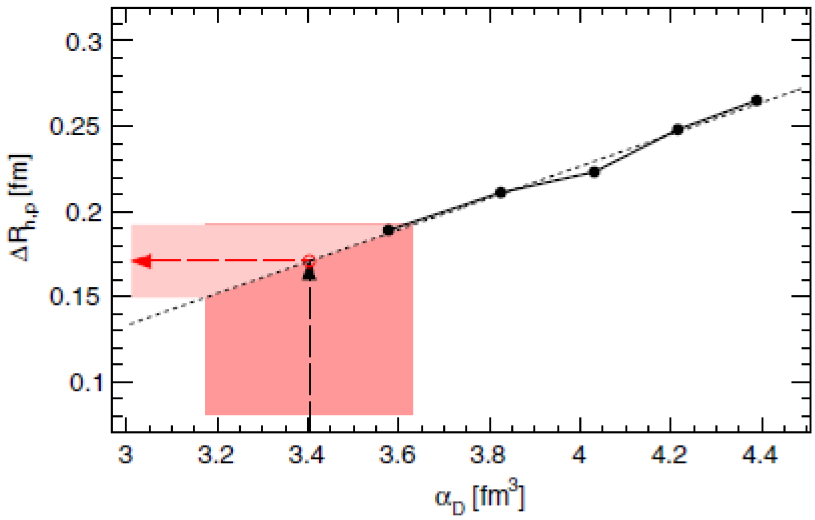

FIGURE 1.11: Correlation between neutron-skin thickness and dipole polarizability in ^{68}Ni using FSUGold [45]. The shaded zones indicate the experimental errors on the measured α_D and extrapolated $\Delta R_{n,p}$ values [44].

Therefore, a systematic study for different nuclei could be very valuable to explore possible model dependence and eventually to constrain the density-dependence of the symmetry energy. The density dependence of the symmetry energy is of fundamental importance because it governs also the radius of neutron stars. This means that the study of the PDR could be a link to understand the neutron stars ($\approx 10^4$ m) starting from the study of the neutron skin in nuclei ($\approx 10^{-15}$ m). Huge theoretical and experimental efforts are indeed still in progress to constrain the symmetry energy of the EoS, and its density dependence.

1.3.2 Influence of the Pygmy Dipole Resonance to the r-process

The study of the PDR may give an important contribution also to the knowledge of the r-process. The majority of the existing elements in the universe are produced in stars. The radiative neutron-capture has a fundamental role in the production of such elements because it is believed to be responsible for the formation of the vast majority of the elements heavier than Fe. Depending on the neutron densities N_n, it is possible to distinguish two types of neutron-capture processes: the slow (s) neutron-capture process, which is a low-density process with $N_n \approx 10^8$ cm^{-3}, and the rapid (r) neutron-capture process, at densities $N_n \approx 10^{20}$ cm^{-3}. The s process operates in mass regions situated within the valley of β stability .
Whereas, the r-process is believed to proceed in explosive stellar environments producing neutron-rich nuclei well beyond the β-stability valley and consequently giving rise to the formation of heavy exotic nuclear systems. In several theoretical works, it is shown that the existence of a low-energy E1 pygmy resonance could enhance the neutron capture cross sections [39–41].
As an example of calculations of this phenomenon, in ref. [46] the author reported the influence of the statistical compound nucleus model, the PDR and the direct capture mechanism, on the radiative neutron capture by neutron-rich nuclei. The neutron capture rates are commonly evaluated within the framework of the statistical model of Hauser-Feshbach . This model makes the fundamental assumption that the capture process takes place with the intermediary formation of a compound nucleus CN in thermodynamic equilibrium. In this approach, the (n,γ) rate, at temperatures of relevance in r-process environments, strongly depends on the low-energy tail of the GDR [46].
However, in this paper [46] the author predicted that the PDR strength, even with a small strength, is enough to increase the neutron capture cross section.
In Fig. 1.12 (a)-(b) we show the Maxwellian-averaged neutron capture rate, calculated with and without the PDR component. In this paper [46] the author evaluated also the influence of a direct channel (DC) process with respect to the formation of a compound nucleus. Studies on neutron capture reactions have been devoted to the description of the DC mechanism, in which the incoming neutron is scattered directly into a final bound state without forming a CN. In Fig. 1.13 the r-abundance distributions, resulting from two r-process events, are shown . The first one Fig. 1.13 (a) is characterized by a low temperature T=10^9 K and a neutron density N= 10^{20} cm^{-3}. In these conditions an (n,γ)-(γ,n) in the equilibrium can not be achieved, i.e. the (n,γ) and (γ,n) rates are not systematically larger than

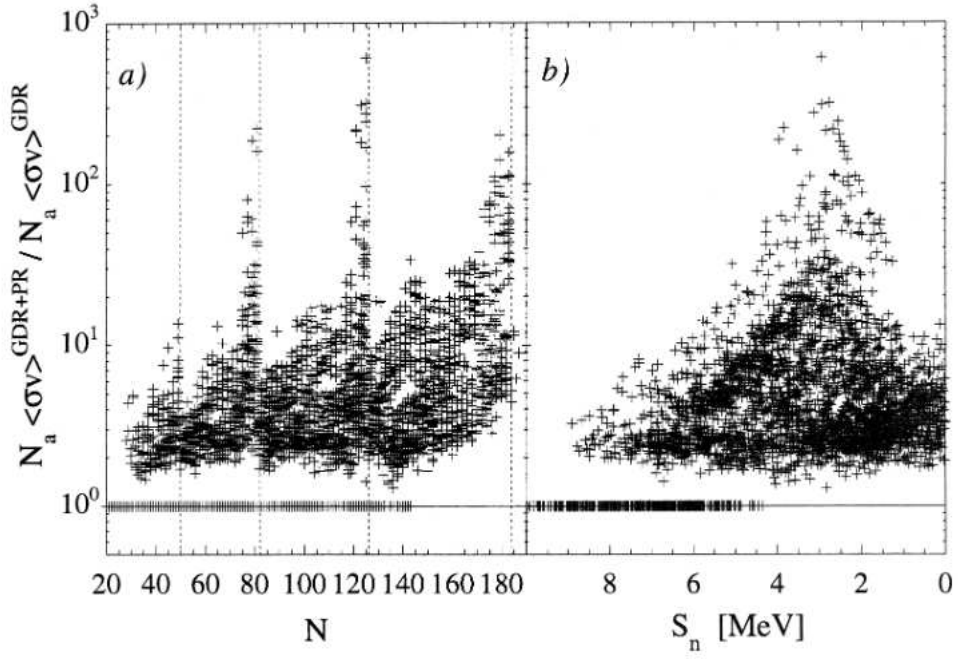

FIGURE 1.12: (a) Ratio of the Maxwellian-averaged (n,γ) rates, calculated at T=1.5 10^9 K with GDR+ PR and without the PR contribution, as a function of N for 3100 neutron-rich nuclei involved in the r-process. (b) same as (a) as a function of S_n [46].

the β-decay rates. As we can note in Fig. 1.13 (a), the GDR rates lead principally to the production of the A $\approx$ 90–110 elements. The PDR effect tends to accelerate the neutron captures and enables the production of heavier nuclei with A $\approx$ 130. However, neither the CN damping effect nor the DC contribution influence the r-abundance distribution significantly. The second example of r-process event is plotted in Fig. 1.13 (b), for a T=1.5 10^9 K and a neutron density N= 10^{28} cm^{-3}, in this case the GDR and GDR + PDR capture rates are much larger than the β-decay rates, so that an (n,γ) equilibrium is achieved in all the isotopic chains.
Recently, more precise microscopic calculations, as the QRPA, have been used to investigate this phenomenon [39]. In particular, the folded QRPA strength is used for the evaluation of the neutron capture cross section within the framework of the statistical model of Hauser–Feshbach. The cross sections at energies around 10 MeV are found to be enhanced by a factor up to 30 when approaching the neutron drip line. The low-energy contribution to the E1 strength predicted by the QRPA calculations is held responsible for this enhancement [39]. This result underlines the crucial role of the PDR in this process. However, more accurate calculations in this area are needed.

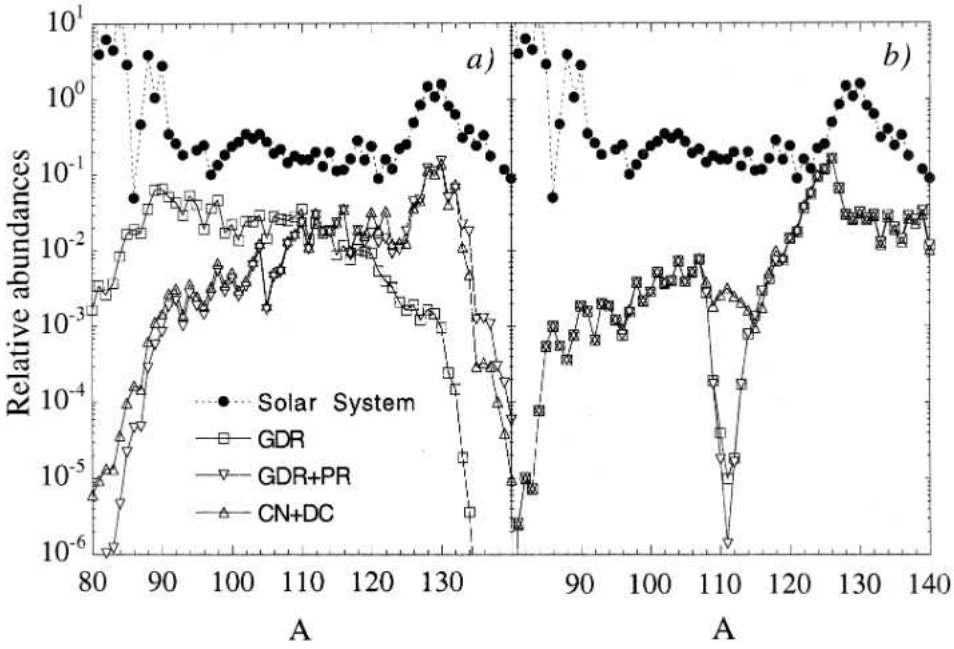

FIGURE 1.13: (a) r-abundance distributions for T=10^9 K and neutron density N= 10^{20} cm^{-3} with three different calculations of the neutron capture rates: the standard GDR component, the GDR + PDR strength and the damped statistical CN plus DC contribution. The top curve corresponds to the solar r-abundances arbitrarily normalized. (b) same as (a) for a T=1.5 10^9 K and a neutron density N= 10^{28} cm^{-3}[46].

Chapter 2

Experimental method for the study of the PDR

In this Chapter we introduce the main experimental findings, and in particular we describe the use of nuclear reactions to study the PDR in radioactive beam, that is the subject of this thesis.
The experimental study of the PDR started with the use of the NRF method, however the possibility to excite this mode with both isoscalar and isovector probes allows to use both real or virtual photons and the hadronic interaction, using α particles and others interacting nuclei. In this Chapter we recall two main papers [1, 3].

2.1 Real photons

Experiments using real photons have provided first data to study the PDR properties in stable nuclei. The method of photon scattering (γ, γ') nuclear resonance fluorescence (NRF) was used to investigate several stable nuclei in different mass regions. The real photons are highly selective to excite dipole states, this means that exclusively the J=1 states are excited in an even-even nucleus. Moreover, the excitation mechanism is well known and this includes only the electromagnetic interaction. For this reason, the spin, parity or transition strengths can be extracted from the measured quantities in a model independent way.
The disadvantage is that photons are often completely absorbed in the excitation process; consequently to determine the excitation energy the photon energy has to be known. It is possible to use a mono-energetic photon beam, in order to know the photon energy from the beginning, or the excitation energy has to be deduced from the spectroscopy of the decay products. Moreover, depending on the properties of the photon beam either excited states in a large or narrow energy region

are populated from the ground state.
In the case of single excitations one is sensitive to the integrated cross section $I_{i,f}$, which describes the excitation from the ground state into the excited state at E_i and the following decay to the final state at E_f. The connection to the corresponding transition widths is given by [1, 47]:

$$I_{i,f} = \pi^2 \left(\frac{\hbar c}{E_i}\right)^2 g \frac{\Gamma_0 \Gamma_f}{\Gamma} \tag{2.1}$$

In this equation Γ is the total width and Γ_0 and Γ_f are the partial width to the ground state and the final state, respectively. The spin factor is given by $g = (2j_i + 1)/(2j_0 + 1)$. The decay width to the ground state is directly linked to the reduced transition probabilities B which for the present case of E1 is given by (formula taken from [1, 47]):

$$\frac{B(E_1)\uparrow}{e^2 fm^2} = 9.554 \cdot 10^{-4} g \frac{\Gamma_0}{meV} \left(\frac{MeV}{E_i}\right)^3 = 2.49 \cdot 10^{-3} \frac{\Gamma}{\Gamma_0} \frac{I_{i,0}}{keV fm^2} \frac{MeV}{E_i} \tag{2.2}$$

In order to calculate the decay width Γ_0 and the B(E1) values for the single excitations, the corresponding decay branching to the ground state has to be known. In some cases, no decays to excited states are observed and thus Γ_0/Γ=1. However, small and unobserved decays to excited final states may add and lead to a value of Γ_0/Γ smaller than 1. In this case the extracted B(E1) values represent a lower limit. In such approach, parity and spin quantum numbers can be deduced by investigating angular and polarization observables. For the determination of the spin of the excited state the multipolarity of the transition can be measured, using the angular distribution of photons with respect to the incoming beam. In the case of an even-even nucleus and thus a ground state of $J_0^\pi = 0^+$ the angular distributions of the spin cascades 0→1→0 and 0→2→0 differ considerably from each other and from an isotropic distribution. For these cases it is sufficient to measure the intensity of the transition at few angles, as 90 ° and 135 ° with respect to the beam axis. This means that, from an experimental point of view, few detectors but with a high resolution are needed to perform these investigations. For odd nuclei the situation is different and the angular distribution could not show such strong dependency on the angle, this means that the spin assignments is more difficult.
For the determination of the parity the polarization of one of the involved photons needs to be defined, either a polarized photon beam is used for the excitation or the polarization of the scattered photons is measured, for example using the

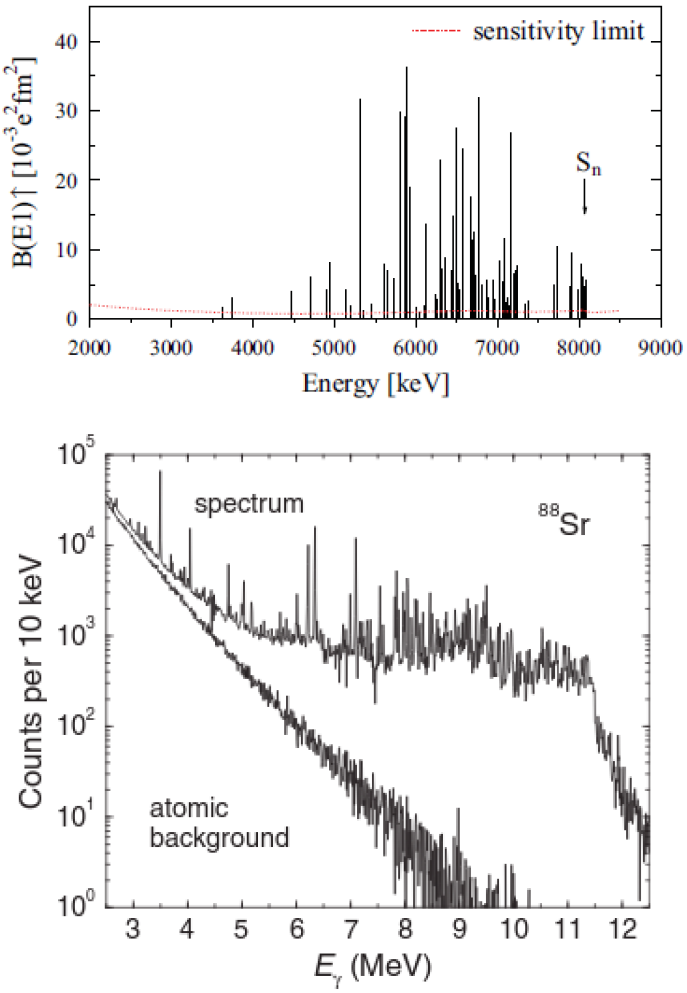

FIGURE 2.1: Upper: Measured E1 strength distribution in ^{136}Xe up to the neutron separation energy. The dotted line indicates the sensitivity limit of the experiment[47]. Lower: γ-rays spectrum obtained for ^{88}Sr and corrected for background and detector response [48].

Compton polarimetry method [1].

This NRF approach requires the observation of the single transitions, which means to resolve the corresponding peaks in the measured spectra. The big advantage of this analysis is that does not depend by models, namely no specific models need to be applied in order to extract the properties of such excited states. Using this approach several stable nuclei are studied in different mass regions, as an example we show in Fig. 2.1 (upper panel) the result of an experiment [47] performed with this method.

When one leaves the approach state-to-state, the complete spectrum, including the continuous part, need to be analyzed. This requires a more complex analysis, taking into account not only primary transitions but also secondary transitions and

background distribution. In this way also nuclei with a high level density can be studied. However, this study includes the necessity to perform simulations which should also consider the detector response. Such simulations should be also able to remove some background, as well as to evaluate the branching ratios, performing, for example, statistical calculations. An example of the results obtained with this method is shown in Fig. 2.1 (lower panel) [48].
First experiments with real photons were carried out at excitation energies below the neutron separation energy, and the decay radiation was measured with high precision using High-Purity Germanium (HPGe) semiconductor detectors. In the region around and above the neutron threshold, the photo dissociation process is the dominant reaction channel. For this excitation energy region the neutron energies in the (γ,n) reaction are very low and thus a prompt detection in order to perform time-of-flight spectroscopy is difficult. In addition, the daughter nucleus has a very low-energy excited states and the only measure of the neutron energy does not provide the information to reconstruct the excitation energy. Consequently, the energy information has to be determined by the photon beam itself.

2.2 Coulomb excitation

With the aim to investigate the Pygmy Dipole Resonance also the Coulomb excitation has been used, in particular this method is applicable for radioactive beams. In order to study radioactive nuclei, the beams are focused on a target, which is the one inducing the electromagnetic excitation. Typically targets with a high Z, as Au or Pb, are used. The study of the PDR is in this case performed by the detection of photon decay or/and by the determination of the neutron decay. The decay of the excited projectiles is detected using a photon spectrometer or calorimeter surrounding the target, or a neutron detector, and also heavy-ion detectors for tracking and identifying the heavy charged fragments.
The process of relativistic Coulomb excitation is mainly selective to electric dipole excitations, similar to real-photon absorption. For ultra-relativistic energies, the equivalent photon field, seen by the projectile, corresponds to a plane wave. This implies excitation probabilities, for electric and magnetic multipole transitions, corresponding to those produced by real photons [1]. The instrumental response however might be rather complex due to inefficiencies of the photon detection, or due to misidentification of the number of outgoing neutrons.
At lower beam energies, magnetic dipole excitations are suppressed, while quadrupole

excitations are enhanced compared to real-photon scattering. Indeed, for high-precision measurements the different multipoles have to be considered. Measurements at different beam energies as well as a precise measurement of the scattering-angle distribution can be used to decompose the different multipolarities. Moreover, in the determination of the resonance parameters, contributions from E2 excitations have been taken into account by assuming standard parameters for the giant quadrupole resonance.
In addition to possible admixtures of electromagnetic excitations with respect to the E1, also nuclear excitations have to be considered. In particular, for impact parameters larger than the sum of the two radii of target and projectile, only the electromagnetic interaction is important, while for smaller impact parameters, nuclear processes dominate. In the evaluation of the cross section for the electromagnetic excitation, the nuclear contribution is determined usually with a measurement performed using a carbon target and then this contribution is subtracted from the total cross section.
How the dipole response of nuclei changes with the increasing of the neutrons number has been experimentally investigated for various nuclei in different mass regions. In general, a redistribution of dipole strength towards lower excitation energies has been observed for nuclei with bigger neutron excess. Starting from these experimental studies, it is possible to separate three mass regions, the light dripline nuclei, where the effect of the halo is present, light neutron-rich non-halo nuclei in the mass range A $\approx$ 20 and intermediate-mass to heavy nuclei (Ni and Sn).

2.2.1 Halo nuclei at the neutron dripline and light neutron rich nuclei

Neutron halo nuclei exhibit a very characteristic dipole response. In experiments performed with high-energy radioactive beams it was indeed observed that the low separation energy for nuclei at the drip line results in large dipole transition probabilities, close to the threshold (soft electric dipole mode). The experimental method, used to investigate these nuclei, consists in Coulomb breakup (breakup of core and neutron(s) halo) experiments.
As an example, in Fig. 2.2 we show the results of a Coulomb breakup experiment performed on ^{11}Be and the corresponding theoretical calculations [49, 50]. It is basically the only single-particle component of the valence neutron in the ^{11}Be that contributes to the large observed dipole transition strength, close to the neutron

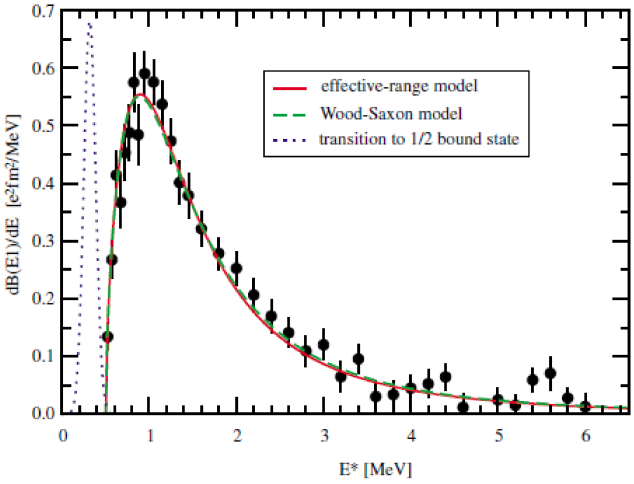

FIGURE 2.2: Dipole-strength distribution of ^{11}Be extracted from a measurement of Coulomb breakup of a 520 MeV/nucleon ^{11}Be beam impinging on a Pb target. The data are from Palit et al. [49]. The solid curve shows a theoretical analysis of Typel and Baur in an effective-range approach[50]. Figure taken from [50].

threshold, indeed this strength is interpreted as a non-resonant direct breakup.

The situation is more complicated for two-neutrons halo nuclei, as ^{11}Li, ^{6}He. The long tail of the neutron wave function leads to large dipole-transition probabilities close to the threshold, like in the case of ^{11}Be. The strength is, however, also sensitive to the correlation amongst the neutrons in the ground state. The soft E1 excitation observed in one-neutron halo nuclei is of non-resonant character and it is related to the single- particle structure of the loosely bound halo neutron. For two-neutron halo nuclei the situation is not fully conclusive.

The dipole response of light neutron-rich nuclei has been investigated only for few nuclei up to now. In ref. [12] the photoneutron cross section for unstable neutron-rich Oxygen isotopes was investigated, observing a dipole strength distribution at lower excitation energies for ^{20,22}O compared to the ^{16}O, see Fig. 2.3 . The authors found that a large fraction of the sum rule is exhausted assuming a ^{16}O core plus excess neutrons (integrating the strength from the threshold to 15 MeV), but with a decreasing trend for the more neutron-rich isotopes. A strict separation into core- and valence-neutron domains seems not to be realized. The strength, integrated up to 20 MeV for the unstable neutron rich nuclei, exceeds the cluster sum-rule limit, meaning that core excitations play a role in this energy region, while for ^{16}O very little strength is found in this energy region.

Also in ref. [13] it is possible to find information about the neutron rich nucleus

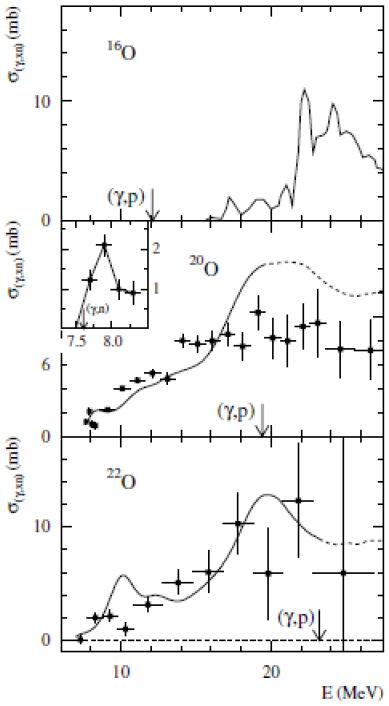

FIGURE 2.3: Photoneutron cross section for ^{16}O as measured with real photons [51] (upper panel), and for the unstable isotopes ^{20,22}O (lower panels) as extracted from the measured electromagnetic excitation cross section (symbols). The inset displays the cross section for ^{20}O near the neutron threshold on an expanded energy scale. The thresholds for decay channels involving protons are indicated by arrows. For ^{20,22}O, the data are compared to the shell model calculations[52]. Figure taken from [12].

^{20}O below the threshold, in which dipole states carry significant strength in contrast to the ^{18}O nucleus, for which no dipole strength in such energy range has been observed. This indicates a shift of dipole strength towards lower energies as one approaches the neutron drip-line. A measurement of Coulomb breakup of ^{26}Ne has been carried out also at RIKEN by Gibelin et al. [53], searching for the PDR.
A substantial redistribution of dipole strength towards lower excitation energies has been observed for light neutron-rich nuclei compared to the stable ones, but in the region of A $\approx$ 20-30 a clear separation with respect to the GDR is not so evident.

2.2.2 Intermediate-mass and heavy nuclei

First experimental observations of the low-lying dipole resonance in heavy neutron-rich unstable nuclei, above the neutron threshold, came from a measurement of the electromagnetic excitation in ^{130,132}Sn at 500 MeV/A investigated at the GSI, using a Pb target. Adrich et al. [54] have reported low-lying dipole strength in excess of the GDR tail, in both nuclei, located at around 10 MeV excitation energy. The results are shown in Fig. 2.4. In contrast to measurements for stable tin isotopes a peak-like structure is clearly visible at lower excitation energy, and well separated from the GDR.
In an another experiment performed at GSI, the PDR has been investigated studying the γ decay of ^{68}Ni projectiles at 600 MeV/nucleon after excitation on gold target [55]. As can be seen in Fig. 2.5, a peak-like structure can be observed in the Doppler corrected γ-ray spectrum above a background, mainly due to the statistical decay of the target or of the projectile nuclei. The Pygmy Dipole Resonance in the ^{68}Ni has been investigated also in ref. [44], measuring the neutron decay after the interaction with a ^{nat}Pb target.

Another suitable experimental method, to extract the full dipole strength in stable nuclei, consists of the proton inelastic scattering at forward angles. The Coulomb excitation method has been applied by Tamii et al. to study the electric and magnetic dipole responses in ^{208}Pb [56]. A high intensity polarized proton beam at 295 MeV has been used to excite ^{208}Pb target nuclei. The scattered protons have been analyzed with high resolution, covering angles close to and including the zero degree. At very forward angles, the cross section for nuclear excitation is

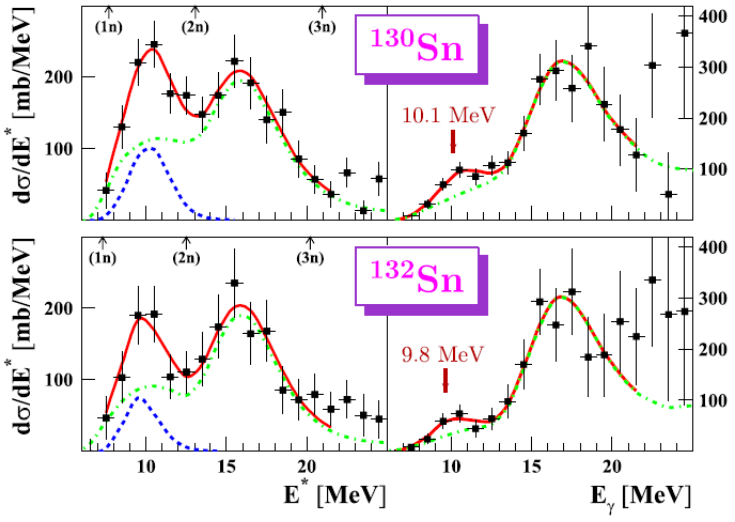

FIGURE 2.4: Electromagnetic dissociation cross sections and deduced photo-neutron cross sections for ^{130}Sn and ^{132}Sn. The dashed and dash-dotted curves show the fitted Gaussian and Lorentzian distributions assigned to the PDR and GDR respectively, while the red solid line is their sum [54].

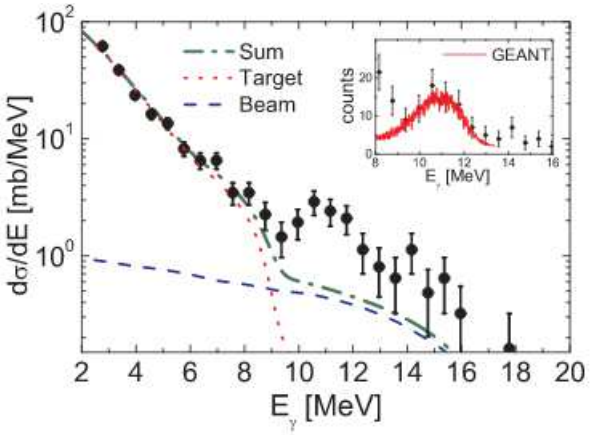

FIGURE 2.5: The high-energy γ-ray spectrum measured with BaF_2 detectors and Doppler corrected with the velocity of the projectile. The lines are the statistical model calculations for the target (dotted line) and for the beam (dashed line) nuclei. In the inset the continuous line superimposed to the measured data is the result of a GEANT simulation for a γ transition at 11 MeV [55].

small and the measured yield is dominated by E1 transition due to Coulomb excitation and nuclear M1 spin-flip transition. In this way the authors extract the cross section related to electromagnetic excitation. Since M1 transitions are suppressed in Coulomb excitation, and the E2 contribution to the cross section is small, the authors have derived the photo-absorption cross section and a B(E1) distribution.

2.3 Hadronic interaction

As discussed above, the PDR may be excited using also isoscalar probes, namely using the hadronic interaction.
One commonly used approach is the inelastic scattering of α particles at about 30 MeV/A at forward angles. As it is known, α particles dominantly excite isoscalar excitations via the hadronic interaction from the ground state. However, compared to the electromagnetic interaction, the hadronic interaction is much less selective: in contrast to real or virtual photons which favor $\Delta J = 1,2$ excitations, exhibiting strong electromagnetic transitions from the ground state, the hadronic interaction can populate states with higher spins and it shows not trivial strength selectivity.
One of the first experiment conducted with α particles was carried out by Poelhekken et al. [57], using a NaI detector. In this experiment, Poelhekken et al. studied the low-energy isoscalar dipole strength in ^{208}Pb, ^{90}Zr, ^{58}Ni and ^{40}Ca, using the $(\alpha, \alpha'\gamma)$ reaction. With a coincidence condition between α and γ-rays was possible to be selective with the $J^{\pi}=1^{-}$ state for investigated nuclei.
In the last decade, the 1^{-} states were studied in numerous nuclei with the (α, $\alpha'\gamma$) reactions [3]. The common feature of these measurements is that only a subset of the 1^{-} states is populated both by (α, $\alpha'\gamma$) and (γ,γ'), while another subset, at higher energy, is populated only via (γ,γ') experiments. Thus these experiments reveal a structural splitting of low-lying electric dipole strength into a first group which can be populated in photon and α scattering and a second group, at higher energy, populated only in photon scattering experiments, as can be observed in Fig. 2.6. This different excitation can be explained by the different nature of the two probes (isovector/isoscalar) or by their different interaction zones within the nucleus (whole nucleus or surface). This result has been also investigated with microscopic calculations [59] in RQTBA and QPM models. These calculations show an enhancement of the isoscalar E1 strength at the lowest excitation energy, while at higher energies the isoscalar strength drops with respect to the isovector E1 strength. In ref. [59] the authors gave a theoretical interpretation on the basis

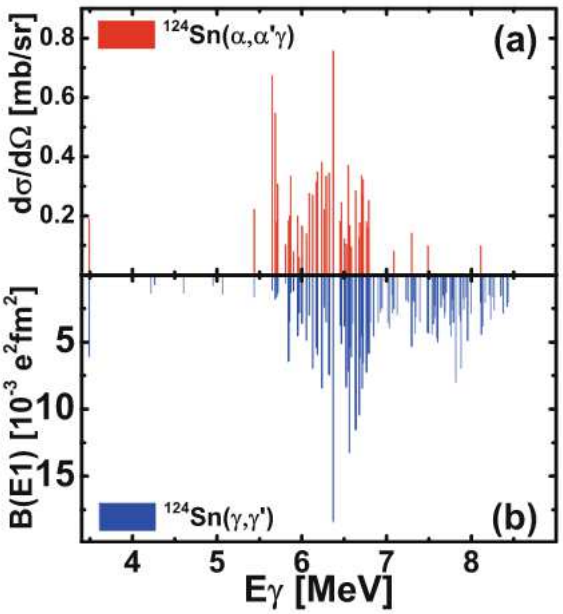

FIGURE 2.6: (a) Cross sections for the excitation of $J^{\pi} = 1^{-}$ in ^{124}Sn deduced from the (α,α' γ) experiment. (b) The B(E1) strength distribution, obtained in (γ, γ') experiment [8][58].

of the transition densities. Indeed while at low excitation energy the E1 strength shows the signatures of a neutron-skin oscillation, typically associated to the PDR, at higher energies the transition densities show more isovector components and represent a transition character towards the IVGDR [59], see also Fig. 2.7 [59].
Another experimental approach to investigate the PDR with isoscalar probes is using different bombarding energies and different types of colliding nuclei, characterized by different mixtures of isoscalar and isovector components.
First experiments with this method were carried out at INFN-LNL using the AGATA demonstrator and LaBr detectors for the γ -ray spectroscopy, in coincidence with the detection of scattered ^{17}O nuclei [3, 60–62]. In particular, as in the case of (α, $\alpha'\gamma$), the (^{17}O, ^{17}O $'$ γ) experiments reveal that the hadronic probes excite strongly only the low-energy region of the pygmy states. This is a further indication of the separation in two distinct parts of the low-lying dipole region: one which is populated by both isoscalar and isovector probes and the other one, at higher energy, where only the electromagnetic interaction excites these states, see Fig. 2.8 [3]. The use of an isoscalar probe was carried out mainly in reaction below the neutron separation threshold on stable nuclei. Recently, the isospin character of low-lying state was investigated, for the first time, in an experiment using both isoscalar and isovector probes on the unstable ^{20}O nucleus [63]. In this experiment the authors

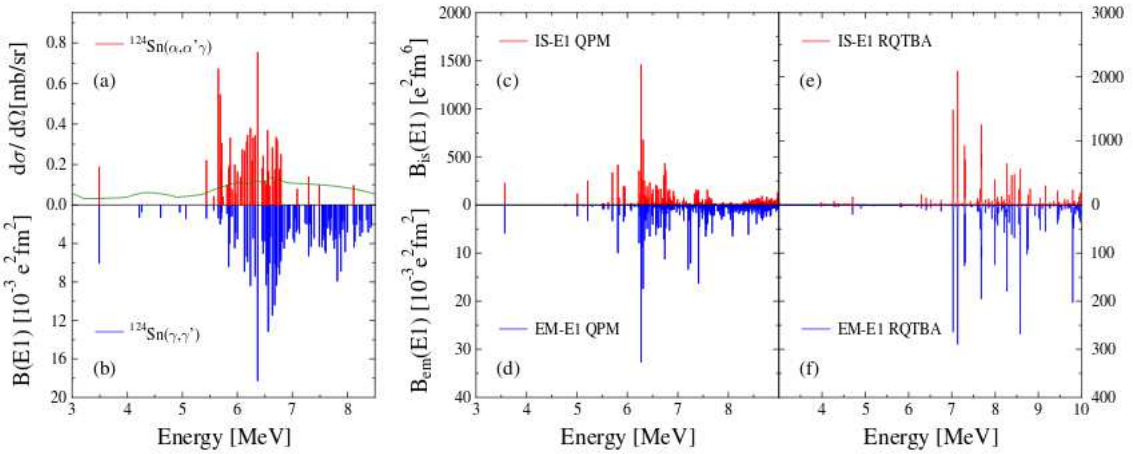

FIGURE 2.7: (a) Singles cross section for the excitation of the $J^{\pi}=1^{-}$ states in ^{124}Sn obtained in the (α,α' γ) coincidence experiment. (b) B(E1) strength distribution measured with the (γ,γ') reaction. The middle column shows the QPM transition probabilities in ^{124}Sn for the isoscalar (c) and electromagnetic (d) dipole operators. The RQTBA strength functions in ^{124}Sn for the isoscalar and electromagnetic dipole operators are shown in (e) and (f), respectively [59].

observed the isospin character and also the isospin mixing seems to be present, as can be observed in Fig. 2.9.

Despite of these several experimental results, the nature of the isospin splitting or isospin mixing phenomenon, in a very limited energy range, has to be better understood and it is currently a topic of interest.

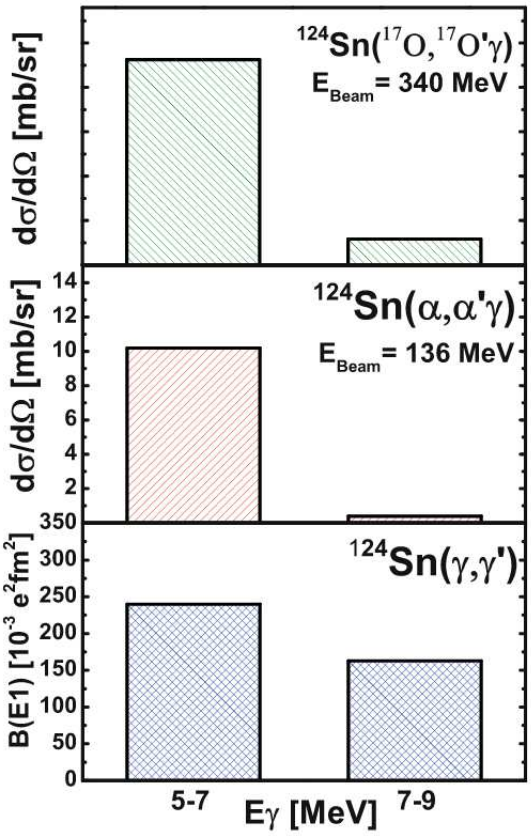

FIGURE 2.8: Differential cross sections measured in the ^{124}Sn(^{17}O,^{17}O$'\gamma$) experiment, corresponding to the discrete lines integrated in two regions 5–7 and 7–9 MeV (top panel). For comparison, the corresponding strengths measured in α-scattering (middle panel) [58] and photon-scattering (bottom panel) [8] are plotted. Figure taken from [3].

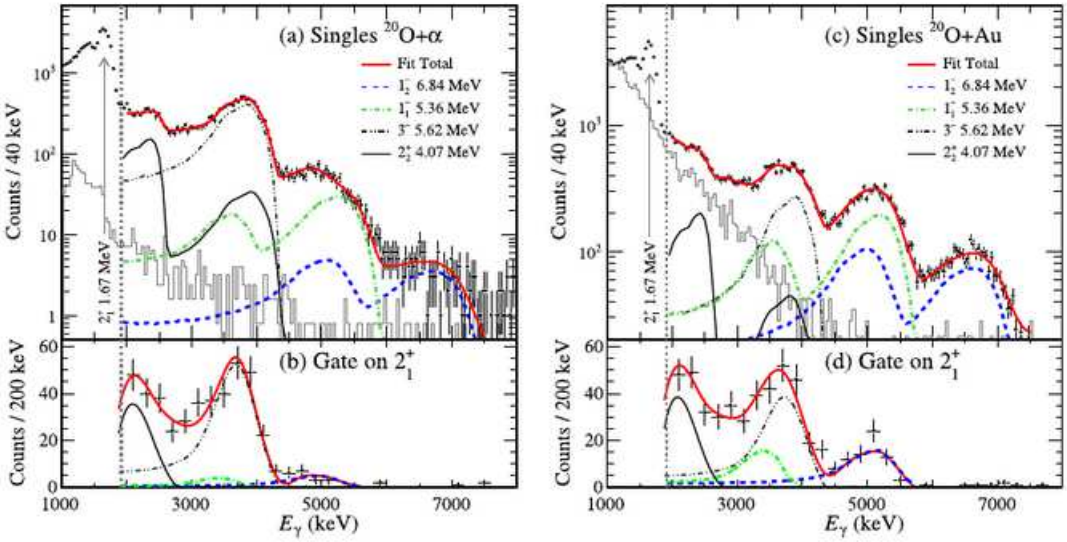

FIGURE 2.9: The Doppler-corrected γ-ray spectra: ^{20}O + α singles (a), ^{20}O + α, detected in coincidence with the 2^+_1 state (1.67 MeV) (b), ^{20}O + Au singles (c), ^{20}O + Au, detected in coincidence with the 2^+_1 state (d). The grey histograms are the background spectra. The grey error bars are statistical[63].

Chapter 3

Experiment

3.1 Pygmy Dipole Resonance in the ^{68}Ni+ ^{12}C reaction

As discussed in the Chapter 2, experiments performed using isoscalar probes may give important information about the PDR structure, despite the difficulty of such experiments, due to the lower selectivity of hadronic reactions with respect to the use of real photons as well as virtual photons.
At INFN-LNS in Catania we performed the first experiment to excite the PDR in the ^{68}Ni through an isoscalar probe, i.e. a natural carbon target, more selective to the isoscalar excitation with respect to the isovector one.
In order to prove that the ^{12}C is a good isoscalar probe and to understand which states can be populated in the ^{68}Ni+ ^{12}C reaction at the energy used in the experiment 28A MeV, there have been performed calculations of inelastic cross section within the semiclassical model, where it is assumed that the motion of the center of mass of the two interacting nuclei is described by the classical mechanics while the nuclear excitation is described according to the quantum mechanics. The model used is based on microscopic form factors built with microscopic RPA transition densities [4, 15, 16], including the states of natural parity of multipolarities between 0 and 3. Such calculations have been done according to the semiclassical coupled channel model described in refs. [4, 15, 16], where the real part of the optical potential has been obtained by the double folding procedure, while the imaginary part has been chosen to have the same geometry of the real part with half of its intensity. This is a standard procedure when one has no experimental information about the elastic scattering cross section. The details about the semiclassical model and the calculations are described in Appendix A.
In Fig. 3.1 we show the obtained results with the approach above described for the calculation performed including the RPA states having more than 5 % EWSR. In the panel (a) the Nuclear contribution is shown, in the panel (b) is plotted the

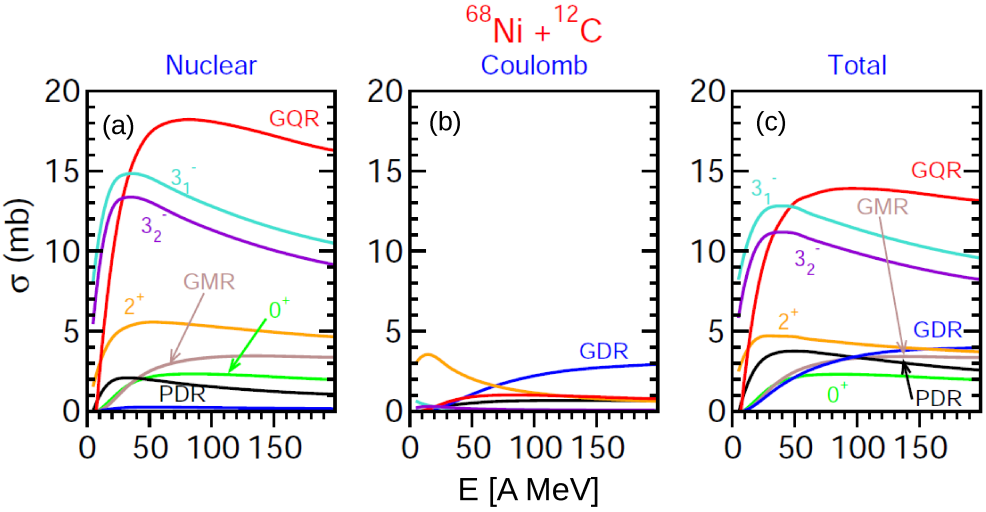

FIGURE 3.1: Computed cross sections for the population of various excitation modes in the reaction ^{68}Ni+^{12}C as a function of the beam energy (AMeV) in the laboratory frame.

Coulomb one and in the panel (c) both contributions are taken into account. From the figure (c) one can see that, at about 28A MeV, the PDR has a cross section larger than the GDR, the GMR and the low-lying 0^+ state. While the PDR cross section is smaller than the low-lying 2^+ and 3^- states. However, these latter states have an excitation energy lower than 5 MeV. As it is possible to observe, the GQR has the largest cross section, approximately 10 times larger than the PDR.

We stress that in Fig 3.1 the cross sections for the population of these states are plotted. Such cross sections are obtained as an integral over the classical impact parameters contributing to the process; therefore they contain the contributions of all possible scattering angles.

In order to compare these calculations with the experimental data, that will be discussed in the following Chapters, one has first of all to perform the integral only over the impact parameters that contribute to the measured scattering angles and then to combine the cross section calculations with the γ-decay probability or with the neutron decay probability. For instance the γ-decay probability of the GQR is

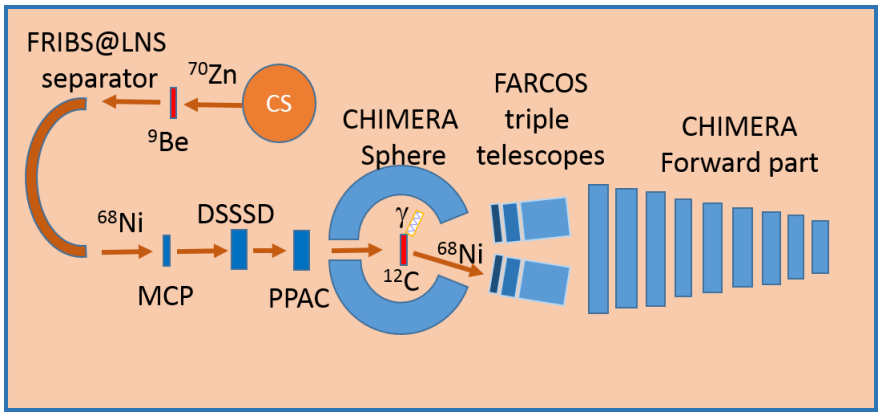

FIGURE 3.2: A sketch not to scale of the used experimental set up.

quite small, therefore even if this channel has a large cross section for the formation it can not be seen in the γ-decay channel.
Such calculations allow to understand that with ^{68}Ni+ ^{12}C reaction at 28A MeV the PDR state, several low energy states and also the GQR could be populated with a high probability. These semiclassical calculations, show also that at 28A MeV most of the total inelastic PDR cross section (more than 60 %) is due to the pure nuclear interaction.The Coulomb contribution amounts at 9 %, while another 30 % is given by the interference between nuclear and Coulomb contributions.
Moreover, the ^{12}C has a very low probability to emit γ-rays in the region of the PDR (around 10 MeV [44, 55]). All excited levels in this energy range have in fact a negligible branching ratio [64]. Starting from these findings it is evident that, despite of the difficulty of the experiment, in which in principle we have to take into account also for the population of other multipolarities, the reaction that we used is quite selective with respect to the PDR mode.

3.2 Experimental set-up

The experiment was carried out at INFN-LNS in Catania, from the 25/11/2015 to the 12/12/2015. In Fig. 3.2 a sketch, not to scale, of the experimental apparatus is presented.
A ^{70}Zn primary beam was accelerated to an energy of 40A MeV, using the Superconducting Cyclotron (CS), and it impinged on a 250 μm thick ^{9}Be target to produce, with a projectile fragmentation reaction, the ^{68}Ni beam, delivered via the FRIBs@LNS (in **F**light **R**adioactive **I**on **B**eam**s** at INFN-LNS) fragment separator of the INFN-LNS [65, 66]. A fundamental component of this facility is a standard

tagging system [67], which permits to measure event-by-event the isotopic composition of the exotic beam. This tagging system is composed of a Micro-Channel Plate detector (MCP), and of a Double-Sided Silicon Strip Detector (DSSSD). The identification of nuclei in the cocktail beam, as well specified in the section 3.4.2, was obtained by using the ΔE-ToF identification method. The *start* of the Time of Flight (ToF) measurement was given by the MCP, located at a distance of 12.9 m from the DSSSD. The *stop* of the ToF and the ΔE were provided by the strips of the DSSSD, mounted about 2 m before the ^{12}C reaction target.
The DSSSD was also used to obtain the position information, important to reconstruct the trajectory of the beam. In order to determine the beam trajectory more precisely, we used a Parallel Plate Avalanche Counter (PPAC) with a spatial resolution of 1 mm, mounted 80 cm from the 75 μm ^{12}C target.
The PDR can decay via both neutron and γ-rays emission, this latter with less probability. To investigate the decay channels we used the CHIMERA (**C**harged **H**eavy **I**on **M**ass and **E**nergy **R**esolving **A**rray) multidetector [68, 69], whereas to detect the ^{68}Ni and other heavy ions, produced in the reaction with the ^{12}C, we used the FARCOS (**F**emtoscope **AR**ray for **CO**rrelations and **S**pectroscopy) array [70, 71], as better discussed in the following. FARCOS is a modular array of telescopes arranged in a single cluster, each of such telescopes consists of three detection stages. The first two stages are two Double Sided Silicon Strip Detectors (DSSSD) 300 μm and 1500 μm thick respectively. The last stage of a FARCOS telescope consists of four CsI(Tl) crystals.
During the experiment the FARCOS array was composed by four telescopes and it was placed just after the sphere of the CHIMERA multidetector and it covered polar angles from 2° to 7°, with approximately the 70% coverage of azimuthal angles.
In the following we will give details of the several components of the experimental set up and the methods that we used for this experiment.

3.3 FRIBs@LNS facility

The FRIBs@LNS (in **F**light **R**adioactive **I**on **B**eams at INFN-LNS) facility allows to carry out nuclear physics experiments investigating the properties of short-lived nuclear species [65, 66]. In this facility the **R**adioactive **I**on **B**eam**s** (RIBs), from ^{6}He to ^{68}Ni, at intermediate energy, have been produced since 2001 [72], using the fragmentation of various stable beams accelerated by the Superconducting Cyclotron

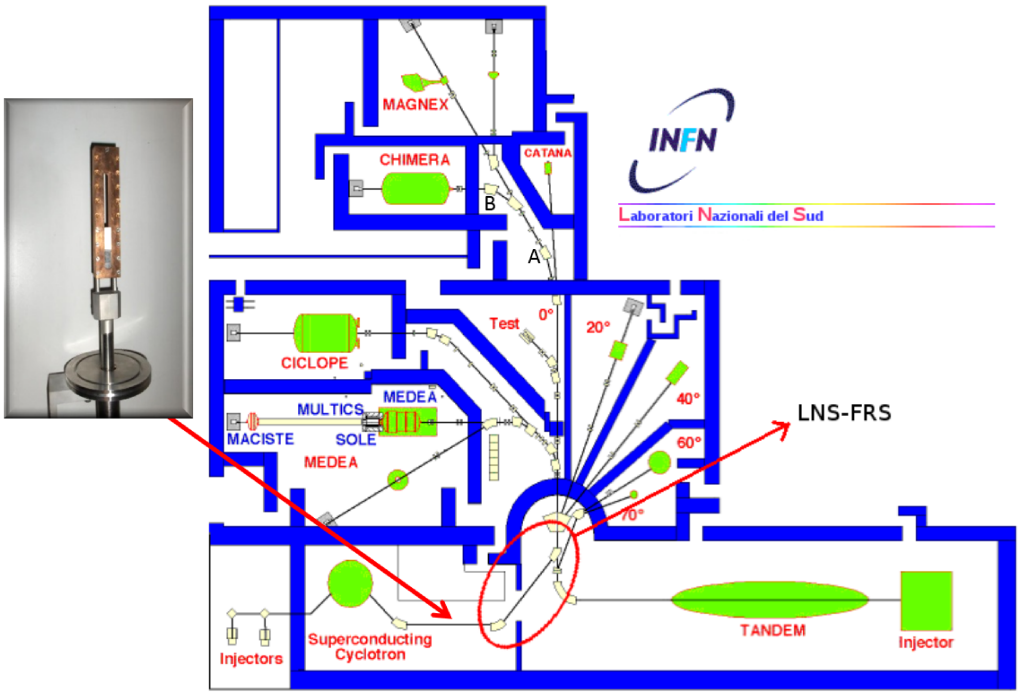

FIGURE 3.3: Map of the INFN-LNS. In this map the fragment separator (LNS-FRS), placed at the exit of the CS, is evident. The two dipoles, at 45° with respect to the beam line, are used to perform the selection of the fragments. Also the position of the ^{9}Be target is indicated in the map. In the upper inset a photo of the ^{9}Be target support is shown.

(CS). In particular, the RIBs are produced using the so called in-flight technique, namely the fragmentation of a fast projectile, the primary beam accelerated by the CS, on a, usually Beryllium, production target. The Beryllium target is placed near to the exit of the Superconducting Cyclotron, as indicated in Fig. 3.3. In the upper part of this figure we show a photo of the Beryllium support system, this system is water cooled and movable.

Currently, the typical intensities for beams obtained with FRIBs are limited by the maximum power (100 W) of the Superconducting Cyclotron [65]. For the ^{68}Ni beam the expected intensity was about 20 KHz.

In the projectile fragmentation reaction a multitude of nuclei are produced, therefore a magnetic analysis and a selection are needed to select RIBs of interest at the desired energy. Indeed, the nuclei of interest should be separated from the primary beam and other fragments produced in the target reaction. The advantage of using intermediate energy reactions in inverse kinematics is that all the products leave the target with velocities close to the primary beam one, and they

can be selected in-flight, since they follow different trajectories in a magnetic field. The fragment separator allows to separate the reaction products from the beam and in certain cases to select specific isotopes (according to the atomic mass A or the atomic number Z). In general, the electro-magnetic separation is due to the Coulomb and Lorentz forces that deflect ions according to [73]:

$$\vec{F} = \frac{d\vec{p}}{dt} = q(\vec{E} + \vec{v} \times \vec{B}) \tag{3.1}$$

Using this formula for a particle with a charge q, velocity v, electric field E and magnetic field B, one can calculate the particle trajectory $\frac{d\vec{p}}{dt}$. If E is equal to zero and B is a homogeneous magnetic field perpendicular to the ions velocity , the ion trajectory is a circle with a radius ρ. Typically, the variable that allows to calculate such trajectory is the magnetic rigidity, define as Bρ:

$$B\rho = \frac{p}{q} \tag{3.2}$$

The unit of the magnetic rigidity is the Tesla meter.
An electro-magnetic separator consists of different basic elements, the most common ones are the magnetic dipoles, the magnetic quadrupoles, and also multipoles of higher order.
The fragment separator of the FRIBs facility consists, as it is possible to observe in Fig. 3.3, of two 45 $^\circ$ dipoles of the standard transport line, to perform the magnetic selection, trying to maximize the yield of the wanted unstable isotope and to eliminate unwanted isotopes.
In Fig. 3.4 it is shown in detail the composition of the fragment separator. The two bending dipole magnets D1 and D2 are positioned downstream the target, while to focus the beam of reaction products, quadrupole magnets are placed in front and behind each dipole. In particular three quadrupoles triplets Q1-Q3, Q4-Q6 and Q7-Q9 are used with two sextupoles correctors S4, S9 near quadrupoles Q4, Q9. Also the possible position of the degrader, placed at the intermediate focus, is shown in Fig. 3.4.
The collision products are then analyzed by the FRIBs fragment separator with Bρ values selected to maximize the transmission of one specific isotope or, in average, the bunch of isotopes one is interested to study. It is known that a magnetic analysis can not separate isotopes with the same m/q ratio, or m/Z in case of fully stripped ions, moreover due to the finite $\Delta p/p$ acceptance ($\approx$ 1 % in the case of FRIBs), the obtained exotic beam is a cocktail beam, i.e. it contains several isotopes

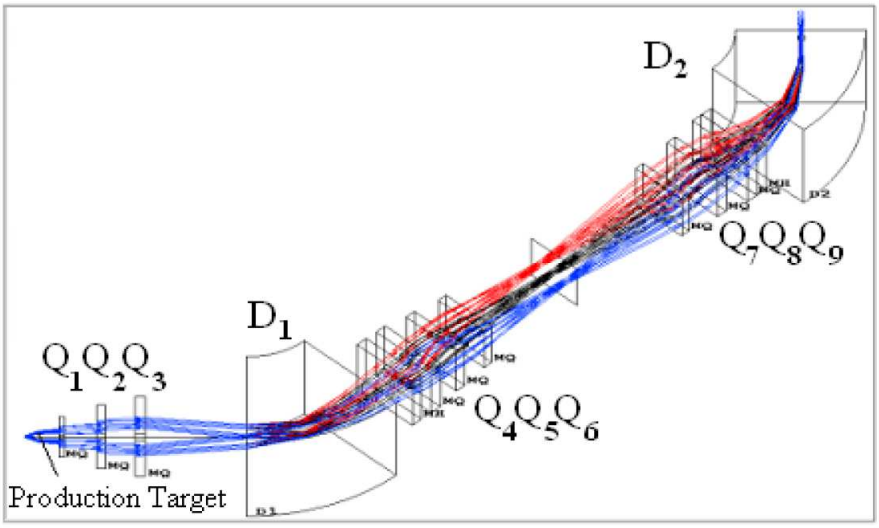

FIGURE 3.4: In figure the standard layout of the fragment separator is shown.

at the same time. In some cases, this can also be an advantage since a single experimental configuration allows to carry out a measurement with different beams. However, this means that an event-by-event identification (using a so called "tagging" method) of ions, arriving on the reaction target point, is needed in order to offline select the desired beam. For that purpose, a device has been developed in the CHIMERA beam line [67], whose characteristics are described in details in the following sections.

With the purpose to optimize the transport on the beam line we used a standard method, based on the use of a "pilot" beam, namely, in our case, a beam of ^{70}Zn transported with the same Bρ used for the transport of the ^{68}Ni (B$\rho \approx 2.0334$ Tm). This purpose was obtained using a thin Aluminum target to degrade the energy of ^{70}Zn primary beam. The optimized transport achieved for the pilot beam is, in principle, valid for the secondary beam, also because the beam energy degradation produces a pilot beam with similar emittance as the fragmentation beam. In the whole beam line, from the CS to the CHIMERA hall, there are several Faraday cups, that allow to count the intensity of the beam, and several Al_2O_3 targets, to check the correct focusing of the beam. The transport of the beam and the correct focusing on the CHIMERA chamber target point were checked using a Al_2O_3 target and a video-camera. Of course, during this procedure the DSSSD and the MCP were moved out with respect to the correct position. When the pilot beam was correctly transported and focused on the CHIMERA target point, we proceeded with

the ^{70}Zn primary beam for the production of the fragmentation beam.

3.4 Tagging system

The tagging system consists of a large surface Micro Channel Plate (MCP) that produces the *start* of Time of Flight (ToF) measurement, and of a Double Sided Silicon Strips Detector (DSSSD) mounted at about 12.9 meters after the MCP and at about 2 meters from the reaction target. The DSSSD delivers the energy loss (ΔE), the first information on the beam position and the *stop* for the ToF measurement. However, we have to underline that multichannel Time Digital Converters (TDCs) used in the experiment can work only with a common stop mode, therefore we inverted the timing, using the MCP signal to stop all TDCs used in the experiment. In the following we will present both calibrated ΔE-ToF scatter plots and not calibrated plots, in which the time is measured with the *start* from the DSSSD and the *stop* obtained with a delayed MCP signal (smaller channels number means longer time difference).
In this tagging system also a Parallel Plate Avalanche Counter (PPAC), mounted at about 80 cm from the reaction target, and having 1 mm of spatial resolution, is used to reconstruct precisely the trajectory of the exotic beam. In Fig. 3.5 we show a scheme of the used tagging system.

The large surface MCP (43 $\times$ 63 mm^2, 700 μm thick) was assembled starting from the bare micro-channel glasses, made by Topag Lasertechnik and mounted in a chevron configuration. An aluminized mylar foil (2 μm thick) with an evaporation of LiF (15 μg/cm^2) is used as source of electrons, emitted when the beam impinges on the foil. Those electrons are driven, by using an electric field, to the upper surface of the MCP. The electron drift region is constituted by a metallic box supporting a grid biased at the same voltage of the upper surface of the MCP. Such box has a lateral opening to allow the beam crossing. The fast signal emitted from the biased MCP is collected by a planar anode. A resistive divider provides the right bias voltages to the emitting foil (Vf $\approx$ -4200 V), grid (Vg $\approx$ -2300 V) and rear (Vr $\approx$ -300 V) [67]. This MCP is able to sustain a rate up to 10^6 particles per second, without degradation of efficiency and resolution [67]. The MCP mounted, on a standard ISO-flange, is shown in the left part of the Fig. 3.6. The DSSSD is a standard detector, with a thickness of 156 μm and 32 mm $\times$ 32 mm strips, 2 mm

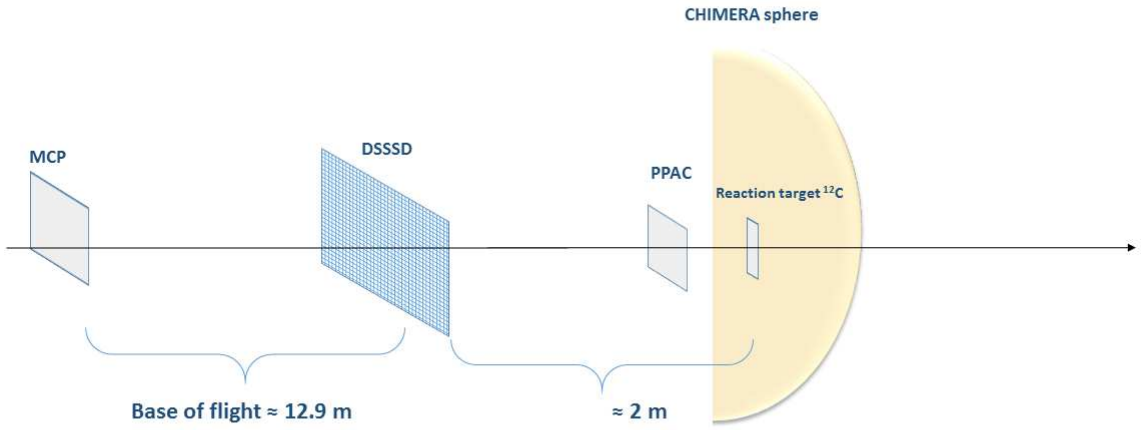

FIGURE 3.5: Scheme, not to scale, of the tagging system.

wide. This detector was polarized with V $\approx$ 30 Volt (reverse current $\approx$ 5 μA). In the right part of Fig. 3.6 a photo of the DSSSD is shown.

3.4.1 Production of charge states

At the energy used for the experiment the probability to produce, after the ^{9}Be target, not fully stripped ions is significant. It is therefore interesting to measure the presence of different charge states, after the ^{9}Be production target.
We indeed performed a preliminary test to study the population of charge states. In particular we measured after the ^{9}Be target the population of charge states of the ^{70}Zn degraded beam. The population was evaluated changing the magnetic field of the first dipole and measuring in a faraday cup the beam current of the various charge states obtained. In Tab. 3.1 such values are reported. We note that 92 % of the beam is fully stripped, but a not negligible amount of ions is produced also at the charge states 29^{+} and 28^{+}. We verified further that these percentages are well reproduced by LISE++ calculations [74].

After the verification of the presence of different charge states in the cocktail beam we had to understand if these charge states were transported along the whole

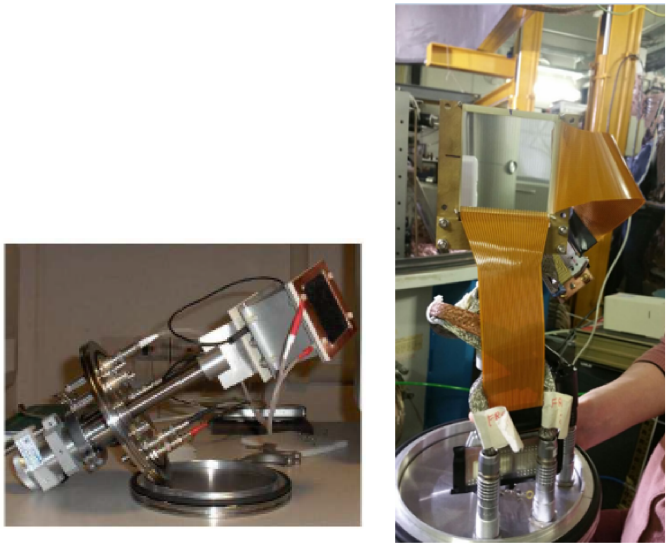

FIGURE 3.6: Left: Photo of the MCP detector mounted on a ISO-flange. Right: Photo of the DSSSD.

TABLE 3.1: Values of the charge state, energy, Bρ, measured current on the first dipole, measured current on the Faraday cup, ppA, measured percentage of the charge state and valuated percentage with LISE++.

Char. State	E [MeV/A]	B ρ	Cur. magnet[A]	Far. cup [nA]	ppA	% measured	% LISE
30^+	32.978	1.944	127	1.35	45	92%	91.78%
29^+	32.978	2.011	131	0.11	3.8	7.8%	7.88%
28^+	32.978	2.083	136	0.003	0.1	0.2%	0.34%
27^+	32.978	2.160	141	− − −	− − −	− − −	− − −

beam line and in particular the effect of the MCP mylar foil on the transport. In fact the beam passing the mylar foil can change its charge state.
Therefore contaminants not fully stripped have around 90% probability to lose the remaining electrons so changing their Bρ. After the MCP two further dipoles of the transport beam line are present before the CHIMERA chamber, therefore the cocktail beam is purified by most of these contaminants. On the other side also fully stripped ions of the correct Bρ have a 10% probability to gain an electron again changing their Bρ. Such ions are then lost from the beam.
In order to verify this cleaning effect and to measure the amount of beam contaminants we changed the current in the last two magnets of the beam line to measure the presence of ions 28^+ becoming 27^+ after the MCP and of ions 27^+ becoming 28^+. The obtained identification scatter plots are plotted in Fig. 3.7 ((a) and (c)), compared with the standard 28^+- 28^+ case (figure (b)). In detail one can note that ^{68}Ni ions are present in the case of $28^+ \rightarrow 27^+$. These are the part of beam lost

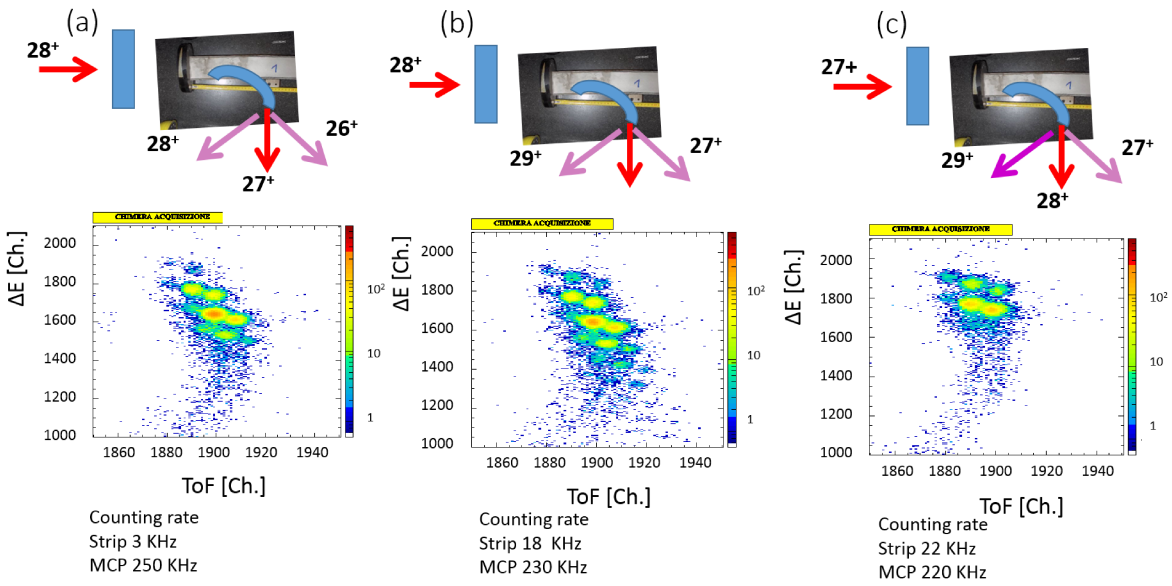

FIGURE 3.7: ΔE-ToF plots obtained during the test selecting the several charge states.

because of the MCP effect. In the $27^+ \rightarrow 28^+$ case Cu and Zn ions dominate, while in the region of ^{68}Ni the beam intensity is rather small. We evaluated that the contamination due to the presence of the 27^+ state is very low, as can be observed in the (c) panel. With this method we therefore proved that the stripping effect of the MCP allowed to clean the cocktail beam from most of contaminants.

We used this procedure also during the Pygmy experiment, the obtained results are shown in Fig. 3.8. In these figures we show calibrated ΔE-ToF plots, obtained with the calibration discussed in the section 3.4.2.

In the figure (a) we show the ΔE-ToF obtained in the case of $28^+ \rightarrow 27^+$. In this case we obtained a very low statistics, confirming that the losses of the 28^+ state are very low. In the figure (b) we show the ΔE-ToF obtained in the case of $28^+ \rightarrow 28^+$. In the figure (c) we display the ΔE-ToF obtained in the case of $27^+ \rightarrow 28^+$. Also in this case we confirm the results obtained during the test, having a small contamination due to the 27^+.

Following this procedure we evaluated in detail that just the 92% of the incoming Zn beam is totally stripped, more than the 7% of the ions have a charge state of 29^+, and also the 28^+ charge state is present. However the configuration of the transport beam line, with the presence of magnets after the MCP, allows to reject the largest amount of this background by the stripping effect of the mylar foil.

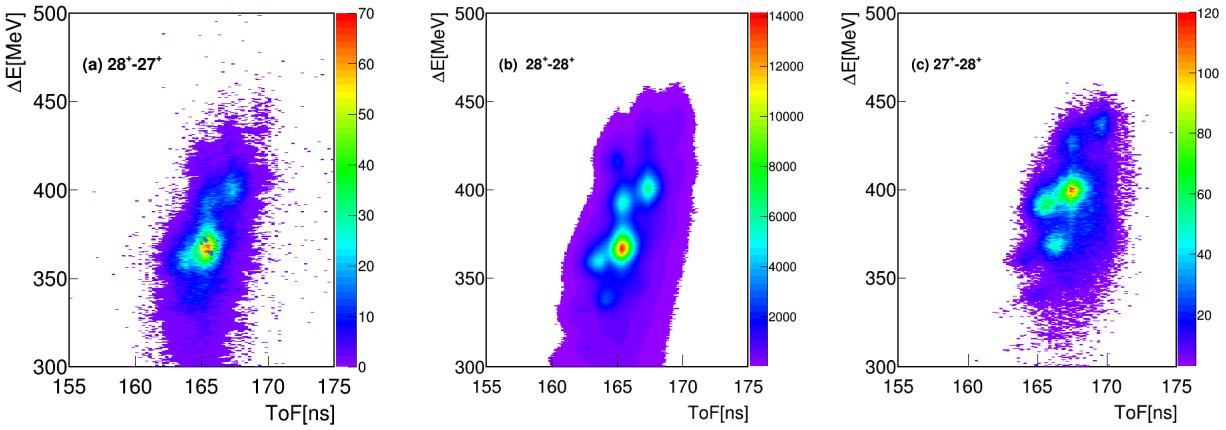

FIGURE 3.8: ΔE-ToF plots obtained during the Pygmy experiment selecting different charge states.

With this method we were therefore able to correctly identify the $^{68}Ni^{28+}$ beam.

3.4.2 Calibration of the DSSSD and MCP detector

The first part of the data analysis was dedicated to the calibration of the tagging system (DSSSD+MCP). Performing LISE++ simulations [74], taking into account the beam line elements, we were able to evaluate the expected yield of fragments, produced in the reaction with the ^{9}Be target, as shown in Fig. 3.9. In this figure is indeed shown a ΔE-ToF plot, obtained with a LISE++ simulation. Each bump shown in the figure corresponds to a nucleus, with determined values of ΔE-ToF, the colors are indicative of the intensity for each nucleus. The LISE++ simulations were a fundamental support, because allowed also to take into account the presence of charge states, produced in the reaction.

During the experiment we realized that, due to the high energy loss of the heavy ion fragments, the DSSSD was damaged. This means that the response function was not the same for the whole measurement. Therefore, we performed several calibrations, for each strip of the tagging system, to take into account of the radiation damage and the change in the detector response.
To have an idea of the calibration procedure and of the radiation damage of the

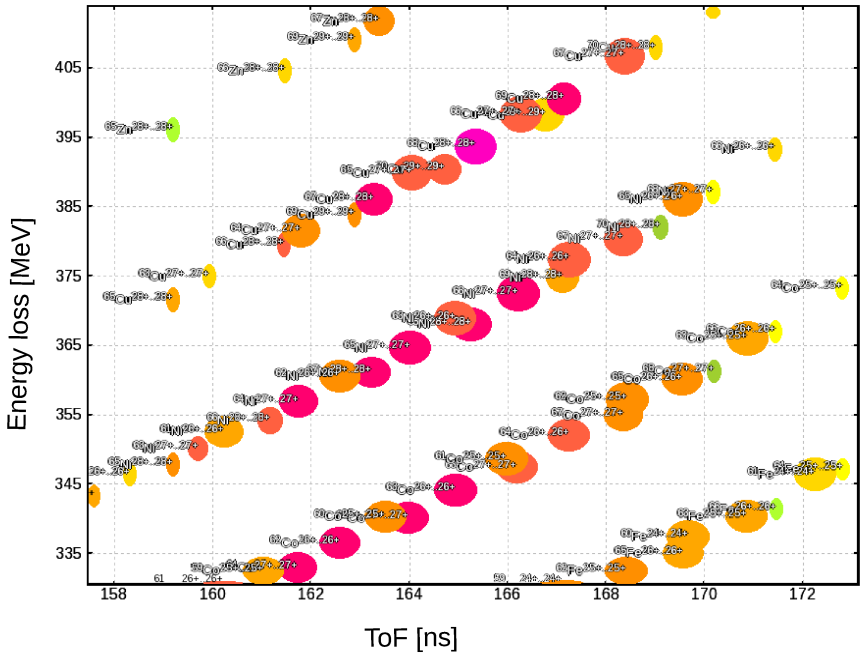

FIGURE 3.9: LISE++ simulation [74] obtained considering the energy loss on the DSSSD. In this simulation it is possible to see several nuclei, produced in the reaction ^{70}Zn + ^{9}Be.

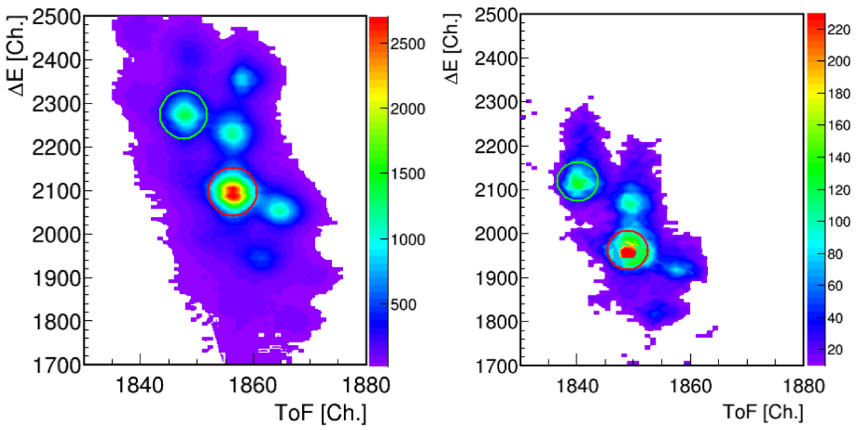

FIGURE 3.10: Left: ΔE-ToF plot obtained in the first part of the experiment. Right: ΔE-ToF plot obtained in the last part of the experiment.

DSSSD, we show in Fig. 3.10 two ΔE-ToF plots, for the same strip of DSSSD, respectively for the first part of the experiment (left) and for the last part of the experiment (right).

In Fig. 3.10 one can note that the ^{68}Ni (red circles) is the most abundant beam obtained in the cocktail. In the left part of the figure we note a good separation between several nuclei, whereas in the right part the separation between several isotopes is worse. Moreover we note a shift in the response of the detector, due to the damage of DSSSD. Some strips were completely damaged, and in that case we have removed these latter from the data analysis.

To obtain the calibration, we performed graphical cuts on the ΔE-ToF plot in channels, to select the nuclei. As an example in Fig. 3.10 are indicated the ΔE-ToF regions corresponding to the ^{68}Ni (red circles) and to the ^{69}Cu nucleus (green circles). We performed Gaussian fits on the projections in energy and time of each bump, to extract the centroids. In Fig. 3.11 we show the Gaussian fits on these projections, in the case of the ^{68}Ni cuts (red histograms) and ^{69}Cu (green histograms), for the first part of the experiment ((a)-(b)) and the last part of the experiment ((c)-(d)). In Fig. 3.11 (c) is clearly visible the damage of the DSSSD, that leads to a worse energy resolution with respect to the first part of the experiment (figure (a)).

We evaluated an energy resolution of 3 % for the first part of the experiment, while in the last part the energy resolution was about 5 %. The damage in the time signal is less evident, indeed the time resolution was $\approx$ 1 % for the whole measurement. We underline that the measured resolution, also in the first part of the experiment, is mainly due to the fragmentation beam spread. Indeed, with the FRIBs facility

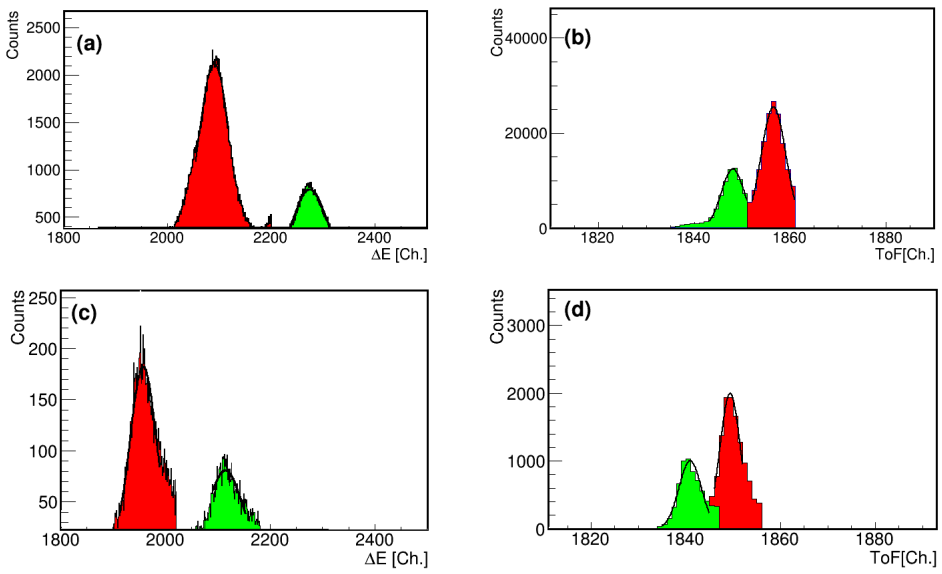

FIGURE 3.11: Gaussian fits on the cuts shown in Fig. 3.10 for the ^{68}Ni (red histograms) and for the ^{69}Cu (green histograms) The (a)-(b) panels correspond to the first part of the experiment while the (c)-(d) ones correspond to the last part of the experiment.

we transport ≈1 % of $\Delta p/p$.
As mentioned above, we followed the calibration procedure for each strip of the tagging system and for each nucleus observed in the ΔE-ToF plot. Moreover, also with the support of the LISE++ simulations, we were able to assign at each centroid the corresponding values of ΔE [MeV] and ToF [ns].
In this way we performed linear fits, in order to have the energy and the time calibration. As an example, in Fig. 3.12 we plot the linear fits for a strip of the DSSSD, for the first part of the experiment (a)-(b) and for the last part of the experiment (c)-(d). While in Tab. 3.2 and Tab. 3.3 we report the values of centroids and the relative energy and time values for each bump, in such tables moreover it is also possible to observe the isotopes that compose the exotic beam.

We stress that despite of the damage of the DSSSD, a carefully selection of beams obtained in the cocktail allowed us to minimize the rejection of data.
Finally, in Fig. 3.13 it is shown the calibrated plot for a subset of 100 runs. The calibration of the tagging system permitted to evaluate the total beam intensity obtained during the experiment. In total, we obtained $\approx 1.44 \cdot 10^9$ events of ^{68}Ni and about $9 \cdot 10^9$ total events; namely the ^{68}Ni is ≈ the 20 % of the total beam intensity.

Isotope	Energy [Channels]	Energy [MeV]	Time [Channels]	Time [ns]
^{69}Cu	2275.5	400.6	1848.1	167.2
^{68}Cu	2232.9	393.7	1856.5	165.4
^{68}Ni	2100	368	1856.6	165.3
^{67}Ni	2056.4	361.1	1864.7	163.2
^{65}Co	1950.7	340.1	1861.3	164
zero	1.64E+002	0.00E+000		

TABLE 3.2: In the table we report the centroids for each bump shown in Fig 3.10 Left, obtained with Gaussian fits, and the corresponding values of Energy and Time in MeV and ns.

Isotope	Energy [Channels]	Energy [MeV]	Time [Channels]	Time [ns]
^{69}Cu	2111.11	400.6	1840.12	167.2
^{68}Ni	1957.35	368	1849.36	165.3
zero	1.64E+002	0.00E+000		

TABLE 3.3: In the table we report the centroids for each bump shown in Fig 3.10 Right, obtained with Gaussian fits, and the corresponding values of Energy and Time in MeV and ns.

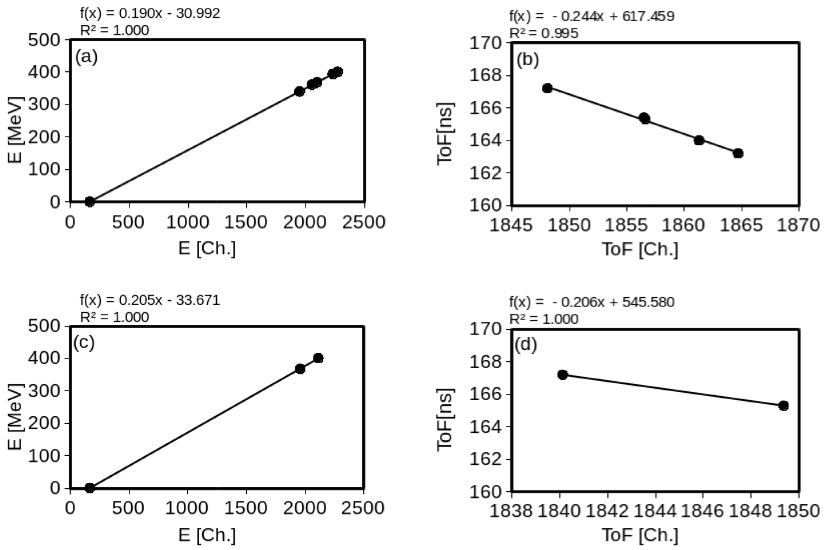

FIGURE 3.12: (a)-(b) Energy and time calibration of a strip for the first part of the experiment. (c)-(d) Energy and time calibration of a strip for the last part of the experiment.

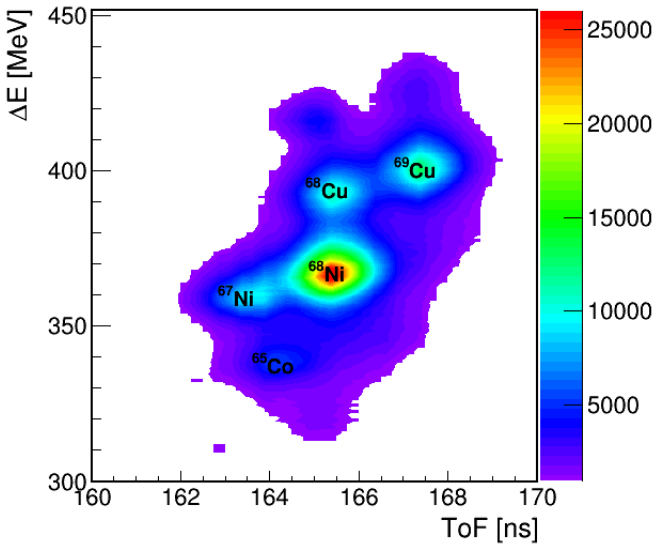

FIGURE 3.13: ΔE-ToF calibrated plot obtained with the tagging system.

As reported in the section 3.4.1 in the case of ^{68}Ni beam, respect to other light systems, a further difficulty in the beam identification is given by the presence of not fully stripped ions. This increases the difficulty in the unambiguous identification of the transported beam particles.
However, thanks to the configuration of the transport beam line, with magnets after the MCP, most of these charge states were rejected. Some small contamination is in any case present, but using the FARCOS array it was possible to remove this background, as will be discussed in the next Chapters.
The total ^{68}Ni beam intensity obtained during the experiment was considerably lower with respect the intensity expected (20 KHz). This was due to a problem with the oven for the production of the ^{70}Zn source. The problem will be totally resolved with the new oven, developed for low-melting element, as the ^{70}Zn, allowing to conduct in the future experiment with a higher intensity.

3.4.3 PPAC detector

As stated above, we used also a Parallel Plate Avalanche Counter (PPAC) in order to evaluate the beam trajectory [75]. The PPAC is composed by a central cathode and two anodes, placed symmetrically with respect to the cathode at a distance of

2.4 mm. The detector active area is 62 $\times$ 62 mm^2. The cathode is made of a 1.5 μm-thick stretched mylar foil with 30 nm of aluminum evaporated on both surfaces. Each anode is a mesh of 60 gold-plated tungsten 20 μm-thick wires in the x and y directions, with a spacing of 1 mm. The wires of the first anode are oriented horizontally while the wires of the second one vertically.
The position information of a beam crossing the PPAC is extracted from the anode signals, using a delay-line readout. Indeed, each wire is electrically connected to discrete LC circuit delay lines of 2.3 ns/mm each, with a 50 Ω impedance, resulting in a total delay of 138 ns in both the x and the y directions [75].
The PPAC is filled with CF_4 at a working pressure of 10–20 mbar. The gas is continuously flowed to avoid contamination due to outgassing from the detector surfaces. The cathode in average was biased at a negative potential of $\approx$ 760 V.
During the experiment we had some problems with the response of the PPAC, for this reason we were not able to reconstruct the trajectory of the beam event-by-event. However, we were able to reconstruct the trajectory of the beam in average. In Fig. 3.14 (left) a photo of the PPAC detector, placed at the entrance of the CHIMERA sphere, is shown. In Fig. 3.14 (right) we show an example of the trajectory of the beam obtained with the PPAC detector during the experiment.

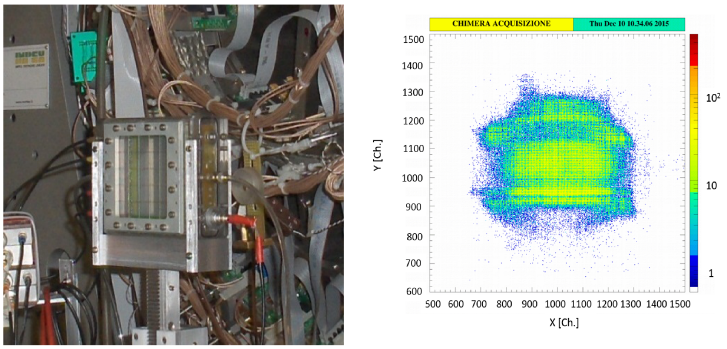

FIGURE 3.14: Left: Photo of the PPAC detector mounted close to the CHIMERA sphere. Right: Beam trajectory obtained during the experiment, it is possible to clearly see the several wires of the PPAC detector.

We used the average trajectory reconstructed with the PPAC and the position information obtained with the DSSSD to evaluate also the angular divergence, obtaining a value of $\approx$ 0.5 $^\circ$. Using the reconstructed beam trajectory, as specified in the following Chapters, we performed Monte Carlo simulations to evaluate the detection efficiency of the ^{68}Ni beam.

Chapter 4

CHIMERA and FARCOS multidetectors

In this Chapter we describe the CHIMERA multidetector and the FARCOS array, the standard electronics used for the Pygmy experiment, the several identification methods and in particular the detection and identification of γ-rays and neutrons as well as the identification of the ^{68}Ni beam and other isotopes produced in the reaction with the ^{12}C target.

4.1 CHIMERA multidetector

The CHIMERA (**C**harged **H**eavy **I**on **M**ass and **E**nergy **R**esolving **A**rray) multidetector was installed at INFN-LNS with the aim to study heavy ion reactions and related reaction mechanisms, in a wide energy range, with a particular attention to the Fermi energy domain [68, 69]. For this purpose CHIMERA was developed to have the following properties:

- High angular coverage (94% of 4π)
- High granularity, achieved with a large number of telescopes (1192)
- Several identification techniques, simultaneously used to identify in mass and charge the emitted nuclei and particles
- Low detection thresholds
- Large dynamic range

The CHIMERA multidetector includes 1192 telescopes, arranged in 35 rings, with a cylindrical geometry along the beam axis and a total length of 4 m. Each telescope consists of a silicon detector followed by a CsI(Tl) scintillator, coupled to a

photodiode, to form a ΔE-E telescope, as schematically shown in Fig. 4.1.

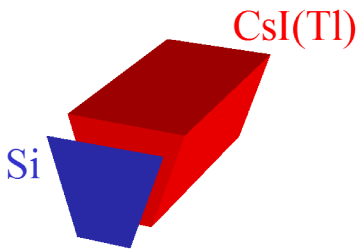

FIGURE 4.1: The basic detection telescope of the CHIMERA multidetector.

The CHIMERA multidetector can be divided in two main parts:

- the so-called forward part, shaped as a cone, consists of 688 telescopes. This forward part is assembled in 18 rings, grouped in couples, and supported by 9 wheels centered on the beam axis. The granularity changes with the increasing of the polar angles. For example, the first wheel is composed of 16 trapezoidal cells, the ninth by 48 trapezoidal cells. Each cell contains a Si-CsI(Tl) telescope. The rings are placed at a distance from the target varying from 350 to 100 cm, with increasing of the polar angle.
  All the rings are put on platforms allowing their independent displacement. This forward part is indeed mechanically independent and covers polar θ angles from 1° to 30°, with 360 ° for the azimuthal ϕ angle. From 0 ° to 1 ° there is a hole to let the beam pass through. A photo of the CHIMERA multidetector, placed inside the CHIMERA vacuum chamber, in which is clearly visible the forward part, is shown in Fig. 4.2.

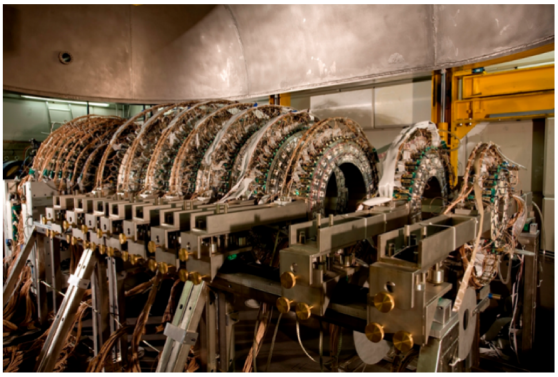

FIGURE 4.2: Photo of the CHIMERA multidetector placed at INFN-LNS.

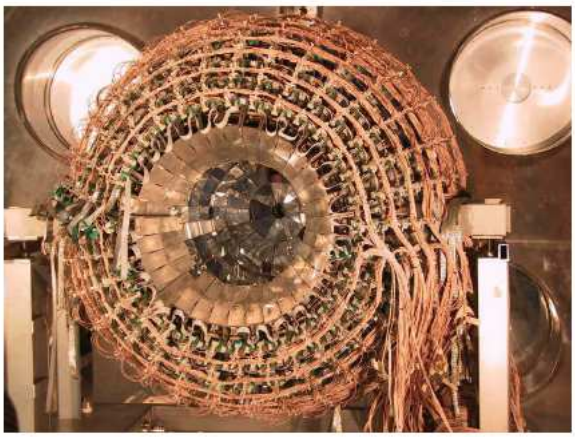

FIGURE 4.3: Photo of the CHIMERA sphere.

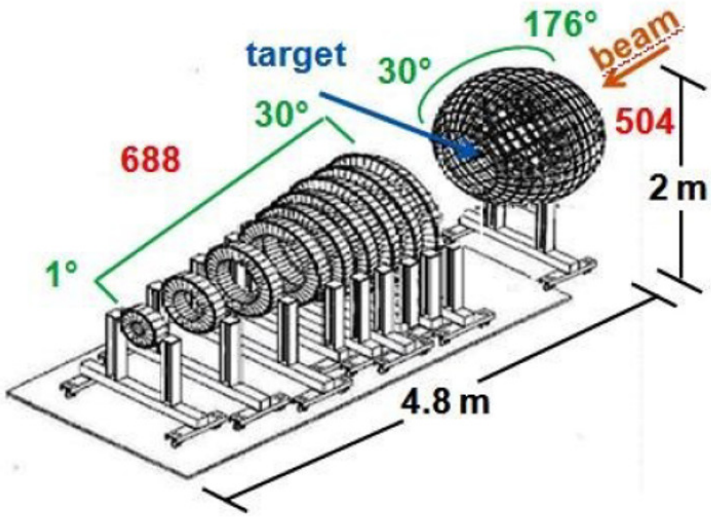

FIGURE 4.4: Scheme of the CHIMERA multidetector.

- the so-called backward part or sphere is composed by 504 telescopes and covers the θ angles from 30° to 176°, and 360 ° of azimuthal angles. The backward part telescopes form a sphere around the target, with a radius of 40 cm. The CHIMERA sphere is further divided in 17 rings. The first 15 rings are segmented into 32 cells, while the last 2 rings are segmented into 16 and 8 cells. Each cell of the spherical part houses a steel box containing a Si and CsI(Tl) detector. A photo of the CHIMERA sphere is shown in Fig. 4.3.

In Fig. 4.4 we show a scheme of the CHIMERA multidetector, in which it is also possible to note the beam direction.
In Tab. 4.1 we report the general characteristics of the detectors, being θ and ϕ

the polar and the azimuthal angles respectively [76]. The guiding principle in the modules distribution of the CHIMERA multidetector is to have a small solid angle in the region of small polar angles. In this region indeed is expected to have the maximum yield of charged particles. This purpose is achieved placing at a relative long distance from the target the first rings, and increasing the sectioning of the rings placed near to the target point.

The detectors include some dead regions, due for example to the presence of target rods and metallic supports. These dead regions, together with the beam entrance and outgoing holes, reduce the geometrical efficiency of the device, leading to a value of 94% of the whole solid angle 4π. In this way a high granularity, giving low multi-hit probability and high solid angle coverage is achieved. These characteristics, together with the low energy detection threshold, greatly enhance the possibility of a complete event reconstruction.
To reach the high vacuum necessary to the good functioning of the detectors (10^{-6} mbar) root, turbo-molecular and cryogenic pumps are used. Moreover, silicon detectors and preamplifiers are cooled by means of a forced circulation of a refrigerant fluid.

4.1.1 Silicon detectors

Silicon detectors are widely used in nuclear physics due to the good energy and time resolution, the high density (2.33 g/cm^3), the low energy to create an electron-hole pair (3.6 eV with respect to 30 eV in gases) and the fast signal collection Time (10 ns in 300 μm Si) [73].
The silicon detectors of the CHIMERA array [77–79] are produced with a passivated planar technology by the MICRON Semiconductor and EURYSIS companies. The fabrication process starts by constructing a wafer of Si that is n doped by means of donors. The surface of the wafer is then passivated by creating a thin layer of SiO_2. Subsequently, some regions of passivation are removed to create windows for the incoming particles. A p -n junction is then created by converting a thin layer of silicon (under the entrance windows) from type n to type p, by means of a boron ionic implantation. The so-formed p-doped zone is often called rectifying contact. To improve the depletion of the junction, a thin layer of As atoms is placed in the rear part of the detector. This region of the detector is often called blocking contact. The construction process ends by evaporating aluminium

Wheels	Ring	Dist. (cm)	Θmin (deg)	Θmax (deg)	Modules	ΔΦ(deg)	Surface (cm^2)	ΔΩ (mSr)/(singlemodule)
1	1 2	350	1.0 1.8	1.8 2.6	16	22.5	16.3 25.6	0.13 0.21
2	3 4	300	2.6 3.6	3.6 4.6	24	15	22.2 29.3	0.25 0.33
3	5 6	250	4.6 5.8	5.8 7.0	32	11.25	23.3 28.6	0.37 0.46
4	7 8	210	7.0 8.5	8.5 10	40	9	24.2 29.1	0.55 0.66
5	9 10	180	10 11.5	11.5 13	40	9	24.8 28.2	0.77 0.87
6	11 12	160	13 14.5	14.5 16	48	7.5	20.8 23.1	0.81 0.90
7	13 14	140	16 18	18 20	48	7.5	26.2 29.1	1.34 1.49
8	15 16	120	20 22	22 24	48	7.5	23.6 25.7	1.64 1.78
9	17 18	100	24 27	27 30.0	48	7.5	29.5 32.7	2.95 3.27
10	19	40	30.0	38.0	32	11.25	24.5	15.33
11	20	40	38.0	46.0	32	11.25	29.3	18.34
12	21	40	46.0	54.0	32	11.25	33.6	21.0
13	22	40	54.0	62.0	32	11.25	37.2	23.25
14	23	40	62.0	70.0	32	11.25	40.1	25.05
15	24	40	70.0	78.0	32	11.25	42.2	26.35
16	25	40	78.0	86.0	32	11.25	43.4	27.15
17	26	40	86.0	94.0	32	11.25	43.9	27.42
18	27	40	94.0	102.0	32	11.25	43.4	27.15
19	28	40	102.0	110.0	32	11.25	42.2	26.35
20	29	40	110.0	118.0	32	11.25	40.1	25.05
21	30	40	118.0	126.0	32	11.25	37.2	23.25
22	31	40	126.0	134.0	32	11.25	33.6	21.0
23	32	40	134.0	142.0	32	11.25	29.3	18.34
24	33	40	142.0	150.0	32	11.25	24.5	15.33
25	34	40	150.0	163.0	16	22.50	56.7	35.45
26	35	40	163.0	176.0	8	45.00	50.9	31.79

TABLE 4.1: Relevant geometric features of the CHIMERA multidetector. For each ring we show: distance from the target, minimum and maximum polar angle θ, number of modules, azimuthal opening $\Delta\Phi$, surface and solid angle of each single detection cell [76].

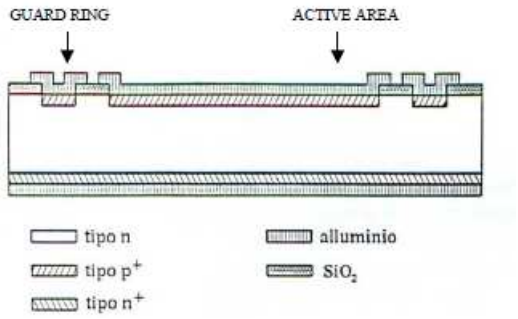

FIGURE 4.5: Typical cross-sectional view of a passivated ion implanted silicon detector with a guard ring surrounding the active area [76].

on both faces of the detector, in order to guarantee the right electrical contacts. In particular, a 300 A° thick aluminium layer covers front and rear faces of the silicon slice. Bonding wires assure the electric contacts from the bias pin to the detector.
In Fig. 4.5 we show the cross-sectional view not to scale of a silicon detector realized with this method.
The nominal thickness of the CHIMERA Si detectors is about 300 μm, with a resistivity of about 3000 and 5000 Ω cm and a capacitance from 500 to 2200 pF, depending on the surface area. The observed rise times are of the order of 10 - 50 ns for light ions. For highly charged ions, the rise time can overcome 150 ns. To optimize the depletion of the silicon junction, the detectors are over-biased by applying an extra-bias of 30% above the nominal one.
The geometry of the Si detectors changes according to the position in the device. In the forward part each cell contains two telescopes (called internal and external). Indeed, in order to minimize the dead layer of silicon detectors and to maximize the detection solid angle, the active zones of the internal and external detectors of each wheel were obtained in a single silicon slice, with a trapezoidal shape, using two active pads designed in a common block, as shown in Fig. 4.6. This procedure allows to avoid external frames, in order to obtain higher geometrical efficiency. The blocking contact is taken at ground in both pads constituting the slice, the rectifying contacts are instead biased at the same negative potential supplied by charge preamplifiers.
In Fig. 4.6 it is possible to note the wide dead zone, corresponding to 500 μm, of the detector, coming from the passivation technique, a guard ring that is placed at a distance of 50 μm from the edges of the active area, having the property to restrict the electric field inside the detector, avoiding the effect caused by a non-complete depletion of the zone close to the borders.

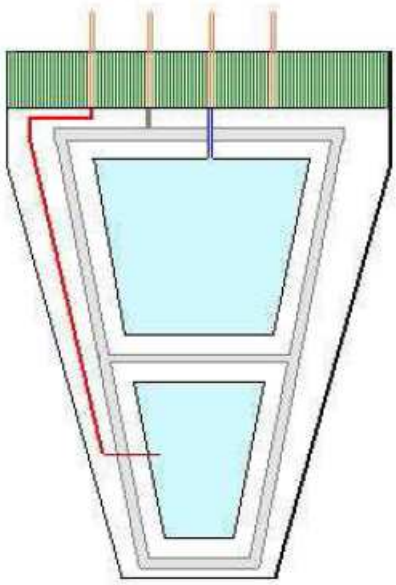

FIGURE 4.6: Not to scale scheme of a silicon detector belonging to the rings of the CHIMERA array. Green: fiberglass support. Azure-blue: detector active areas. Grey: guard ring. Red and Blue: electrical contacts [80].

The silicon bulk is glued to a plastic support (PCB) that allows to connect the detector to the mechanical structure. This PCB support houses 4 contacts: two for the connection of two pads, one for the guard ring connection and one for the common n^+ contact.
The silicon detectors of the sphere are single pad detectors. In this case a huge optimization work was done to minimize dead zones due to the fiberglass supports and to kapton flats used to contact detectors and preamplifiers. In this case a 500 μm alluminium dead zone, in which a guard ring is placed, surrounds the active area. In Fig. 4.7 (a) we show a photo of the Si detectors of the sphere, in Fig. 4.7 (b) we show the scheme of Si detectors in which is possible to note also the dead zone. In this case the Si bulk is glued with 600-800 μm thick epoxy frame, that can be fixed to the steel box of the mechanical structure.

4.1.2 CsI(Tl) detectors

The second detection module of the CHIMERA ΔE-E telescopes is constituted by a CsI(Tl) scintillator, optically coupled to an HAMAMATSU photodiode (324 mm^2

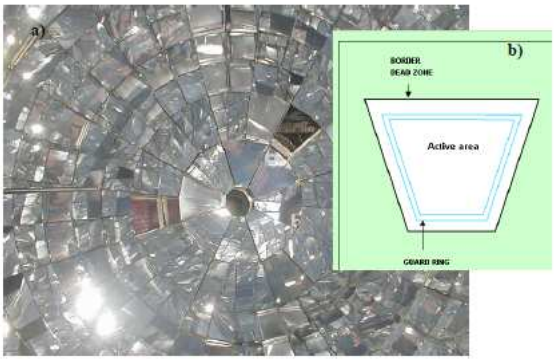

FIGURE 4.7: (a) Photo of the Si detectors of the CHIMERA sphere (b) schematic view of the Si detectors of the sphere [76].

surface, 300 μm thick)[81]. The use of CsI(Tl) has the following advantages in energy measurements [80]:

- Quite high density (4.51 gr/cm^3), leading to a large stopping power. This allows to stop high energy particles in a relatively low thickness. In particular, the CsI(Tl) detector is ideal for the LCP (low charged particles), usually defined as particles with Z$\leq$2. Indeed the density of this scintillator allows to stop these particles in a low distance, in comparison with other scintillators with lower density (for example NaI, 3.67 gr/cm^3)
- Quite low manufacturing costs
- Good light emission yield ($\approx 10^4$ photons/MeV), peaked at λ= 550 nm
- Stability of the response, due to the use of photodiodes
- Mass and charge identification of light particles as well as γ-rays by means of fast-slow correlation analysis.

The shape of CHIMERA scintillators is a truncated pyramid with a trapezoidal base. The dimensions of the front surface are the same of the silicon detectors and they depend on the position in the device. The backward surface of the CsI(Tl) is bigger than the front one, depending on the thickness of the crystal. The thickness for each ring is shown in Tab. 4.2, together with the maximum proton energy stopped in the detector [76].
In order to optimize the light collection, the front surface is covered with a 2 μm reflecting foil of aluminized mylar, while the other faces are wrapped in a 150 μm thick Teflon layer, coated with a 50 μm thick aluminium foil, in order to avoid

RING	Theta	Thickness (cm)	E_{max}^{proton} (MeV)
1-16	1° - 24°	12	190
17-18	24° - 30°	10	160
19-22	30° - 62°	8	140
23-25	62° - 86°	6	120
26-28	86° - 110°	5	95
29-32	110° - 142°	4	95
33-35	142° - 176°	3	90

TABLE 4.2: CsI(Tl) thickness for different rings, we report also the E_{max} of protons stopped in the detector [76].

the light dispersion, with a space in the rear face in order to glue the photodiodes. These photodiodes are indeed glued to the rear face of the CsI(Tl) crystal by means of flexible silicon-based optical cement. The photodiodes are encapsulated in a ceramic support and the light entrance side is protected by a thin window of transparent epoxy.
In general, the CsI(Tl) detectors can be coupled both to photomultipliers or to photodiodes with different merits. For the CHIMERA multidetector the designers chose to couple CsI(Tl) to photodiodes for their low operating voltage leading to low power dissipation, the simple handling and compact assembling and the good stability. Beyond the advantages mentioned above, some limitations exist: for example, photodiodes have signal to noise ratios not so good as photomultipliers.

4.1.3 Electronic chains

In this section we report the electronic chains used during the Pygmy experiment. Currently the pulse shape modules (PSD), described in detail in the following, are available for all the telescopes of the CHIMERA array.
In this section we recall two main works [76, 80]. The signals coming from the Si and CsI(Tl) detectors are processed by two different electronic chains. These chains have been developed to satisfy the following properties:

- Energy measurements with a good resolution in a wide energy range $\approx$ 1-100 A MeV

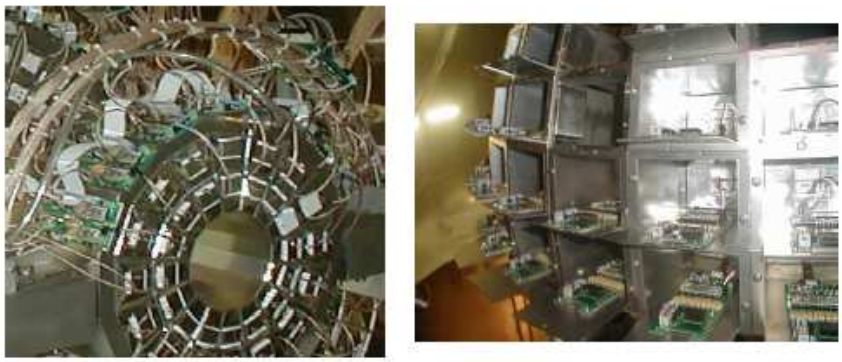

FIGURE 4.8: Photo of the motherboards placed on the external surface of the wheels mechanical structure (left) and on the top of the metallic baskets for sphere detectors (right)[76].

- velocity measurements using the ToF information with a resolution of ≈ 1 ns
- low power dissipation under vacuum

To minimize electronic noises, at a level of few mVolts, Silicon and photodiode preamplifiers have been assembled into motherboards and put in the vacuum chamber, close to the detectors. Each motherboard for the forward part contains four preamplifiers (for the external and internal telescopes), while each motherboard of the sphere contains just two preamplifiers. These motherboards are located on the external surface of the wheels in the forward part of the CHIMERA array, and on the top of the metallic baskets in the spherical part, as we show in Fig. 4.8. Heat dissipation is favored by the metallic contact with cooled supports. The bias supply of detectors and preamplifiers are placed outside the vacuum chamber, together with other racks of processing electronics.

Electronic chain for Si detectors

From the signal delivered by silicon detectors we extract:

- The energy deposited by detected particles
- A logic signal that is used as a start for time of flight measurements
- The rise time of the signal.

With the pulse shape analysis of silicon signals we are able to extract information about the rise time of signal, that can be very useful to identify in charge those slow

nuclei stopped in silicon detectors [82]. During the Pygmy experiment, the pulse shape for Silicon detectors was available just for some rings of the CHIMERA array (from ring 4 to ring 13), leading to two different electronic chains for the Si detectors. A summary scheme of electronic chains for silicon detectors is shown in Fig. 4.9 (top) and in Fig. 4.9 (bottom), where we show the electronic chain in the case in which the pulse shape was available.
In detail, the signals coming from the Si detectors are preamplified by a charge sensitive preamplifier (PAC). Employed preamplifiers were realized by the Saclay Service d'Electronique Nucleaire and INFN-Sezione di Milano, in order to have a low dissipation (200- 250 mW).
This PAC has also a test input, in which it is possible to send pulses generator (pulser signals), in order to control the electronics stability. The PAC integrates the signal of the detector giving to an output height independent of the detector capacity and proportional to the charge produced by detected particles. The output is a single negative fast signal, with a decay time of ≈ 200 μs and a rise time of $\approx$ 50 ns. The PAC sensitivity changes according to the polar angle. In the forward part, where the most energetic particles are expected, the sensitivity is 2 mV/MeV, while in the backward part the sensitivity is 4.5 mV/MeV. In both cases the output signals is lower than 6 Volt, which represents the maximum value accepted by the amplifier, a CAMAC 16 channels bipolar model or a CAEN module NIM1568B in the case of pulse shape electronics.
Each channel of the CAMAC amplifier produces a negative front bipolar signal (with the positive side cut) as energy output and an unipolar signal as timing output, differentiated to 100 ns and integrated to 20 ns. It is also possible to use multiplex output to control the signals coming from working channels.
The energy signals, with a shaping time of 0.7 μs, are coded by charge digital converters (QDCs), realized on VME 9U standard by CAEN.
In order to maintain a good energy resolution, also for low energy signals, the analogical to digital conversion is achieved with a double charge encoding: the "High Gain" (HG) and the "Low Gain" (LG) coding. The HG coding is obtained when the integrated charge is less than 1/8 ratio of the full dynamical range, in this case an amplification factor $\times$ 8 is applied.
As can be seen in Fig. 4.9 (top), the timing copy of the signal is then sent to a Constant Fraction Discriminator (CFD). This signal is of fundamental importance, being used to generate the main trigger.
The CFDs were designed by IPN-Orsay, and they are produced by CAEN on 16

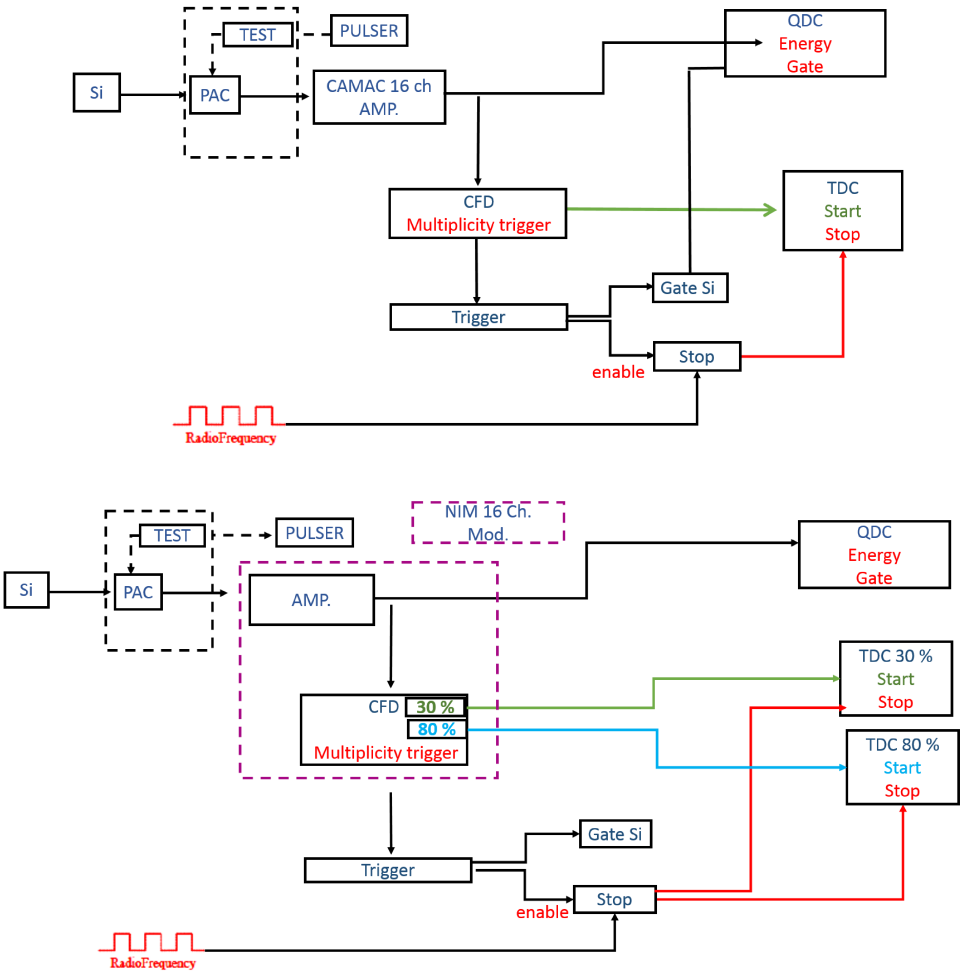

FIGURE 4.9: Top: Scheme of the electronic chain for the silicon detectors in rings 1-3 and 14-26. Amplifiers and CFDs are CAMAC modules. Bottom: Scheme of the electronic chain for silicon detectors in rings 4-13. For these detectors it is possible also to extract the rise-time information. The main component of this electronic chain is constituted by a module NIM1568B. It provides an amplified energy signal, a multiplicity signal and two logic signals corresponding to the instants when the signal overcomes 30% and 80% of its peak value.

channels CAMAC module. The discriminators present the following characteristics [76]:

- input signal with 50 Ω impedance and a maximum voltage of -5 Volt
- a delay of 20 ns
- a fraction typically of 30 %
- a discrimination threshold for each channel adjustable from 1 to 256 mV, in step of 1 mV
- an automatic set of the walk.

In general these CFDs generate also an OR signal, for each 16 channels of the prompt output, and an analogical multiplicity output for each 16 channels, with an amplitude equal to 25 mV for each busy output channel. The prompt output is used as a start signal for a VME 9U time digital converter (TDC), in order to deliver also the start for the time of flight measurement. CFDs are also equipped with a multiplexer that allows to control signals produced by each channel.
A copy of this signal is used to enable the radio frequency (RF) of the CS/MCP signal in order to generate the common stop for the ToF acquisition. This signal is duplicated and sent to all TDCs.
For the ring 4-13 it is also possible to have the pulse shape analysis, as shown in Fig. 4.9 (bottom). In detail, silicon signals are shaped by PACs and amplifiers, and then processed by two discriminators. The discriminators send logic signals when the input signals overcome respectively the 30% and 80% of the total rise time. These two logic signals, together with the energy signal, are obtained using a CAEN 16 channel Spectroscopy Amplifier NIM1568B. The two logic signals are then sent to two TDCs, that transform into digital information time differences with respect to the RF/MCP signal used as a common stop: $\Delta T_{30\%} = T_{RF} - T_{30}\%$ and $\Delta T_{80\%} = T_{RF} - T_{80}\%$.
The subtraction of these two quantities provides the rise time of the signal: $T_{rise} = T_{80}\% - T_{30}\%$. Energy signals are digitized by means of VME QDCs. Also in this case, the gate generation for QDCs is performed by a common trigger signal, based on the multiplicity of each reaction event.

Electronic chain for CsI(Tl) scintillators

In Fig. 4.10 we show the scheme of the electronic chain used for the CsI(Tl) scintillators. The main feature of the CsI(Tl) electronic chain is characterized by the

processing of the fast and slow components of the signal. The fast and slow components are a characteristic of CsI(Tl) detectors and they will be described in detail in the section 4.1.6.
In detail, charge preamplifiers, designed by INFN Sezione di Milano and produced by MICROTEL, provide the photodiode signal readout. These charge preamplifiers have a sensitivity of 50-100 mV/MeV. This requires capacitors that reach a maximum of some hundreds pF. The rise time of the output signals is longer than 50 ns and it can reach values of the order of μs.
Preamplifier signals are amplified and shaped, with variable shaping time (0.5, 1, 2, 3 μs), by means of a unipolar amplifier, designed by INFN Sezione di Milano and produced by SILENA, in 16 channels NIM module. Typically the chosen shaping time is 2 μs. These amplifiers are similar to those used for Si detectors, but they have a double output in energy, for each channel, with different gains, higher= 10*lower. The higher signals are sent to the QDCs, for the integration of the slow component, in order to be digitized and acquired. While the lower signals are sent to a stretcher, designed by the INFN of Milano and produced by ASCOM, in a 48 channels module. The output of the stretcher module is sent to the QDCs for the integration of the fast component. The stretched signals lead to a presence of a level, with the same amplitude of the peak, lasting for $\approx$ 10 μs, time determined from a gate signal.
We send also two synchronous gates to the two QDCs. The used gate signals start a few μs later than the time of peak. Thus, the QDCs outputs will correspond to the charge of the stretched fast signals and the charge integral of the tail of the signal (mainly dominated by the slow component). The correlation between these two quantities allows to identify in charge and mass light charged particles as well as γ-rays.

4.1.4 Trigger condition

In this section we report the standard method used to realize the trigger of the CHIMERA array. Of course each experiment may require different trigger conditions. At the end of this section we report the description of the trigger condition for the Pygmy experiment.
The trigger is the device that decides to process the data of the incoming event. The trigger system of a 4π detector must be able to perform an accurate event selection, in order to enhance the visibility of the events. Moreover, the event rejection

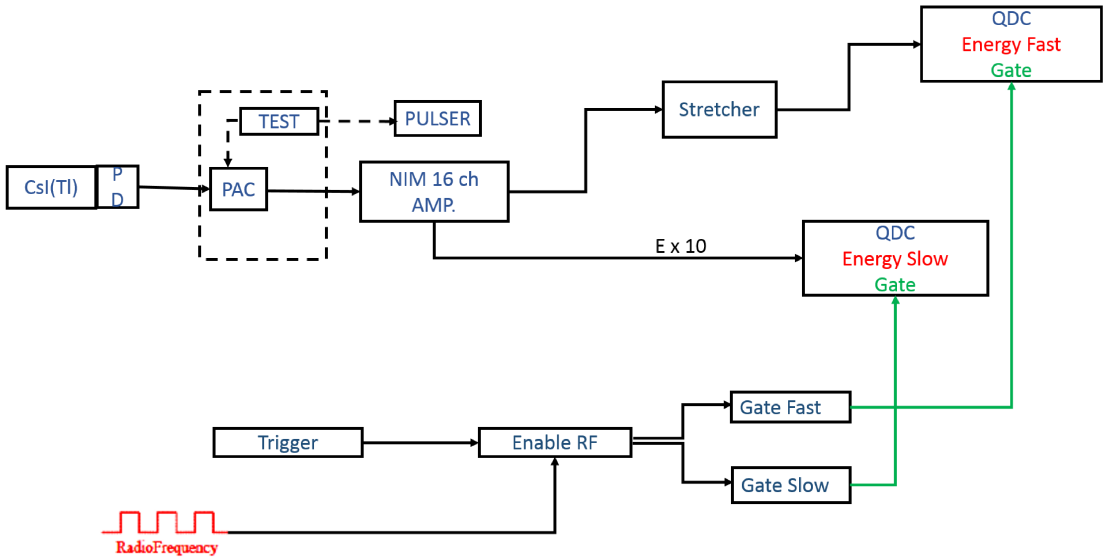

FIGURE 4.10: Sketch of the electronic chain used for the CsI(Tl) signals. The used amplifiers have NIM standard, and are manufactured by SILENA, they manage 16 channels. The stretchers are also NIM based modules. The QDCs are VME modules treating 64 channels with a common gate.

must be fast enough in order to avoid the increase of the dead time. The trigger device must be also flexible to allow the coupling with ancillary detectors. In most experiments performed with the CHIMERA multidetector, involving heavy ion intermediate energy reactions, the trigger is based on the selection of a given detected particle multiplicity.

The final decision to construct the main trigger is based on the analysis of the multiplicity (MASTER TRIGGER) and of other logic signals coming from the CHIMERA array and from any coupled device. In a standard experiment with the CHIMERA array to build the total multiplicity we use the multiplicity signals provided by the Si CFDs.

In particular, the multiplicity signals coming from the Si detectors of the CHIMERA array are summed together in a fan in-fan out. This sum is then sent to a Time Filter Amplifier, with integrated time of 20-50 ns, that allows to remove some noise. The signal is then sent to discriminators, with different thresholds.

For instance, the multiplicity ≥ 1 is obtained when the input signal is higher than 25 mV, multiplicity ≥ 2 is obtained when the input signal is higher than 50 mV. The obtained multiplicity ≥ 1 is typically sent to a divisor module and then to a logic fan in-fan out. In such module is made the logic OR between the divided multiplicity ≥ 1, the multiplicity ≥ 2 and the Pulser signal (with a frequency of 5

Hz). This logic OR is called MASTER TRIGGER.
The MASTER TRIGGER is then sent to a dual gain generator to provide the start signal. While the stop signal is the end-CPU-busy in logic OR with the start of the acquisition, used to remove the dead time at the start of a run.
The output time signal is called DEAD TIME (≈ 200 μs), and it is sent to a discriminator (the output of this discriminator is vetoed by some signals as the end-CPU-busy and the start of the acquisition to avoid spurious signals).
The output of the discriminator signal is called OK EVENT and it is sent as a veto to other discriminator in order to generate a validation window of the RF of the cyclotron. In such discriminator we indeed typically send as input also the RF of the cyclotron, and the output signals are used to generate the gate for Silicon detectors, the gate for the slow component, for the fast component, and the stop of TDCs for time measurements. The start for the TDCs is obtained with the 30 %, and also with the 80 % in the case of PSD modules.

Trigger condition for the Pygmy experiment

The main goal of the Pygmy experiment was the study of the low-lying dipole states, which decays via γ-rays and neutrons emission.
With respect to the standard method used in the CHIMERA multidetector a modification was made in the trigger chain. Indeed, because we used fragmentation beams the reference time was the time signal coming from the MCP detector.
Moreover, as can be seen in the electronic chains shown above (Fig. 4.10) we do not have the possibility to have discriminators acting on the CsI(Tl) signals for the CsI(Tl) detectors, indeed in standard experiments performed with the CHIMERA array the trigger is typically constructed with Si detectors signals.
During the Pygmy experiment the trigger for the acquisition of signals was made considering: the OR between the four telescopes of the FARCOS array, with multiplicity equal to 1, the pulser signal (5 Hz) and the signals coming from the DSSSD of the tagging system, divided by a factor 200. This trigger is necessary to correctly measure and to monitor the beam rate.

4.1.5 Identification methods

With the CHIMERA multidetector it is possible to use different methods to detect and to identify particles and nuclei. We summarize in this section the several methods, with a particular attention on the detection of γ-rays [76, 80, 83, 84]:

- ΔE-E method, using the signals coming from the Si and CsI(Tl) detectors. This method is based on the energy loss by charged particles in a medium, as can be explained by the Bethe-Bloch formula [73], and it allows to identify in charge and in mass those nuclei punching through silicon detectors.
- ΔE-ToF method, using the Si energy signals and the time of flight provided by the Si (start) and the reference time signals provided by the radio frequency coming from the CS (stop). This method allows to perform velocity measurements and it can give information on the mass of nuclei stopped in Si detectors.
- Pulse shape discrimination in Si detectors, this method is based on the analysis of the rise time of Si signals, and it can give information in order to identity in charge the particles and ions stopped in the Si detectors.
- Pulse shape discrimination in CsI(Tl), this method, based on the fast-slow signals provided by the CsI(Tl), allows to identify light charged particles in CsI(Tl) as well as γ-rays.

We show in the following figures several identification plots obtained with the different techniques [80]. In particular, we show in Fig. 4.11 a ΔE-E plot, in Fig. 4.12 a E-Rise Time plot, in Fig. 4.13 a ΔE-ToF plot and in the Fig. 4.14 a pulse shape discrimination (fast-slow) plot.

4.1.6 Particles detection and identification in CsI(Tl)

In order to study the PDR and its decay channel we used the CsI(Tl) scintillator and the fast-slow identification method. In this section we describe in detail such method.
In a CsI(Tl) scintillator the light response, that will be converted in electric pulse by the photodiode, is not linearly related to the energy loss of particles. In particular, defining as $\frac{dL}{dx}$ the light response of a scintillator, this quantity is related to specific energy loss of the particle $\frac{dE}{dx}$, through the Birks formula [73]:

$$\frac{dL}{dx} = \frac{A\frac{dE}{dx}}{1 + B\frac{dE}{dx} + C(\frac{dE}{dx})^2} \tag{4.1}$$

From this formula it follows that we will have an almost linear response only for small stopping power $\frac{dE}{dx}$, namely for light particles such as p, d, t and α at high energy.

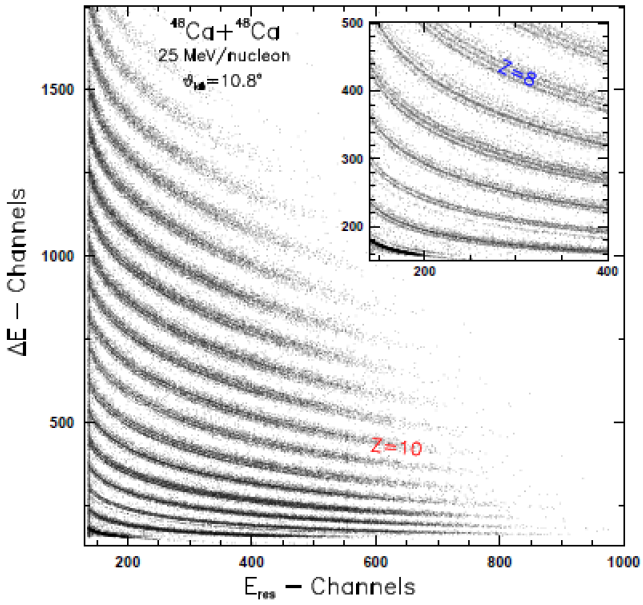

FIGURE 4.11: ΔE-E plot obtained with the CHIMERA multidetector [80].

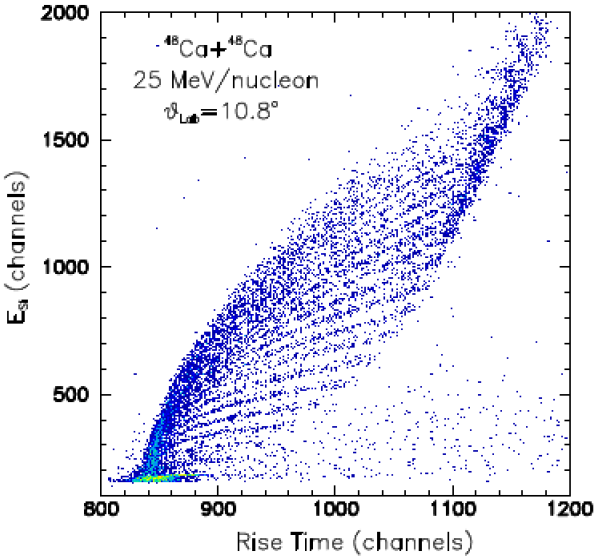

FIGURE 4.12: E-Rise Time plot obtained with the CHIMERA multidetector [80].

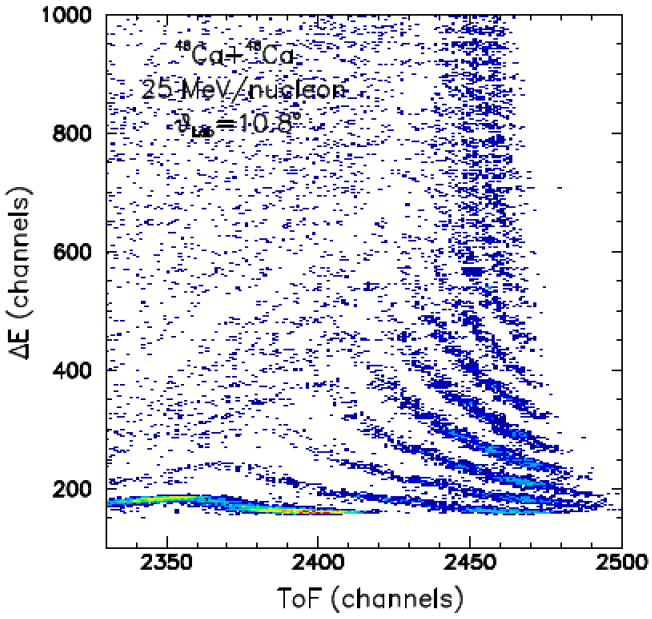

FIGURE 4.13: ΔE-ToF plot obtained with the CHIMERA multidetector [80].

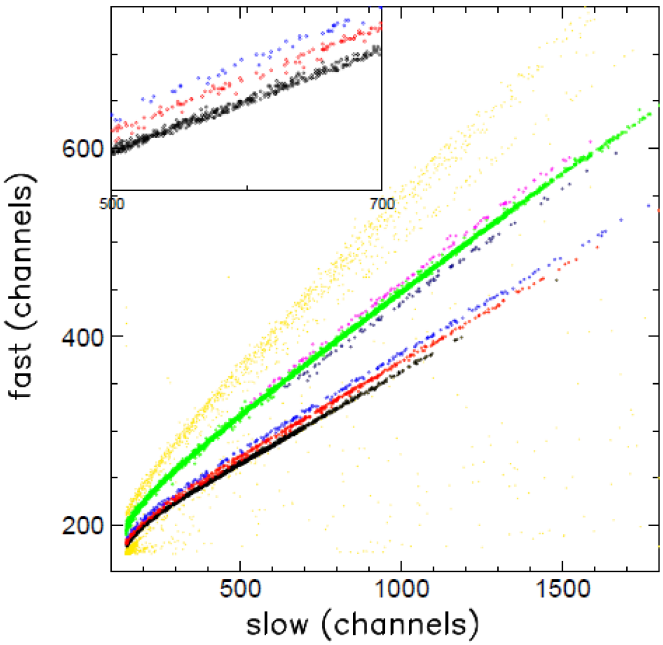

FIGURE 4.14: Fast-Slow identification plot obtained with the CHIMERA multidetector [80].

Moreover, the CsI(Tl) light output L(t) is composed by the overlap of two contributions, with fast and slow decay times, and it can be expressed as follows:

$$L(t) = A_1 e^{-\frac{t}{\tau_1}} + A_2 e^{-\frac{t}{\tau_2}} \tag{4.2}$$

In this equation L(t) is the light pulse amplitude at the time t, A_1, A_2 are the light amplitudes for the fast and slow components, τ_1 and τ_2 denote the decay time constant of the fast and slow components of the light pulse, respectively. Typically the time constant range for τ_1 is between 0.4 μs and 0.7 μs (fast), while τ_2 has a value of about 3.2 μs (slow). These decay times depend on the detected particles.
Particles identification using the photodiode signals of CsI(Tl) detectors can be obtained in different ways: a standard pulse shape method, similar to the one used for neutron-γ discrimination, has been used in ref. [85–89]. A two-gate method [81, 90, 91], with a simpler electronics, or a combination of the two methods [92], have shown also rather good results, also a digital signal analysis has been carried out and reported in ref. [93].
The two-gate method applied to a photodiode is based on the fact that the decay time of the amplifier signal, under proper shaping time conditions, keeps memory of the mass and charge of the detected particles.
The L(t) amplitude, integrated by the photodiode, passes through the amplifier that forms the signal with a time constant of about 1-2 μs. The information relative to the fast component, A_1, is thus maintained unchanged, while the information relative to the slow component, A_2, characterized by a longer time than the amplifier formation time, is cut off and it influences mainly the tail of the signal. Integrating two different parts of the signal, as schematically shown in Fig. 4.15, by means of two gate methods, it is possible to obtain two signals, proportional to the fast and the slow component, produced by the CsI(Tl) amplifier.
Plotting the slow component against the fast component we obtain the identification plot. An example of identification scatter plot obtained with the two gate method is shown in Fig. 4.16 [84].

As stated above, the CHIMERA detector is designed also to provide the mass identification of nuclei using the ToF information. Indeed the detectors are mounted at large distances from the target, up to 3.5 m for the very forward angles. The long fly paths ensure a quite long Time of Flight necessary for the mass identification but, on the other hand, they result in a time jitter of the signals with respect to the used common gate. The stretcher modules, used to analyze the fast component, allow to overcome this problem. In this way indeed, the energy resolution of the

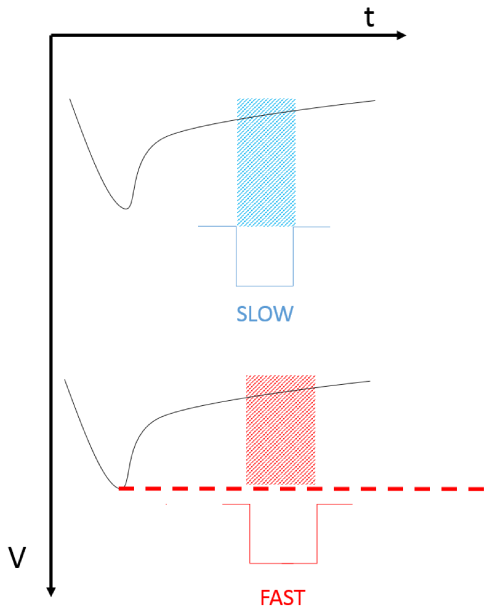

FIGURE 4.15: Scheme of treatment of Fast and Slow components using the two gate method.

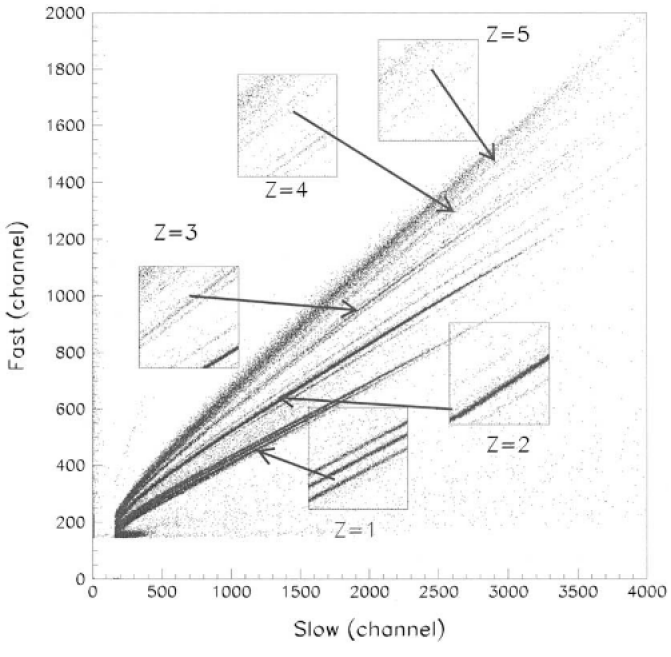

FIGURE 4.16: Fast–Slow identification scatter plot obtained for one crystal, located at θ= 13.75 ° of the CHIMERA array, in the reaction ^{124}Sn+ ^{64}Ni at 35 MeV/A. The insets show expanded portions of the scatter plot [84].

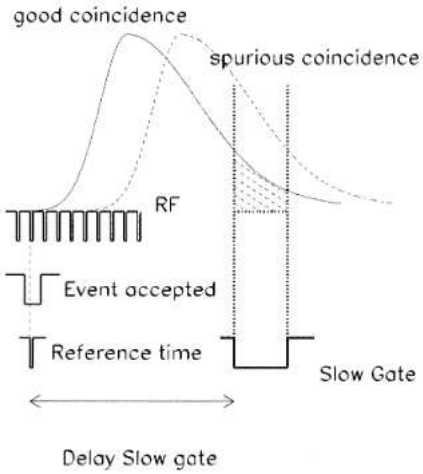

FIGURE 4.17: Sketch of the slow gate timing. The "event accepted" signal, produced by the trigger, enables one RF signal. This signal is used as reference time to generate all gates. The dashed region shows the slow integration region of a signal, produced by a good coincidence. One can note the difference with the charge, integrated with the same gate, for a signal produced in a different burst (dashed signal that corresponds to spurious coincidence) [84].

CsI(Tl) detectors is not affected by any dynamical jitter [84].
In order to work in this way the amplifier output of CsI(Tl), see also Fig. 4.10, is splitted: one signal is sent to the stretcher, when it reaches the maximum amplitude, while the other one, amplified $\times$ 10, remains unchanged. In this way we use a gate for the slow component, of about 2 μs, delayed of 9 μs with respect to the beginning of the signal, that integrates the tail of signals. Another independent gate is generated by the trigger for the fast component, integrating a part of the stretched signal. The gates are generated using as reference time the radio frequency of the cyclotron accelerator validated by the trigger, see Fig. 4.17 [84]. As a consequence of using the RF reference time, coincidences with particles produced within different beam bursts (spurious events, dashed signal of Fig. 4.17) are characterized by a slow integrated signal quite different than the one collected for good coincidences.
Particles produced in different beam bursts are clearly visible in Fig. 4.18, in which are shown data for a detector of the first ring, mounted at θ = 1.4 $^\circ$ [84]. At such small angle, due to the high rate of elastic scattered particles (1 kHz for an individual detector) there is a higher probability to observe spurious coincidences (of the order of 4%). Fig. 4.18 shows that due to the presence of the stretcher, the fast signal is independent on the beam burst, while the slow component is sampled,

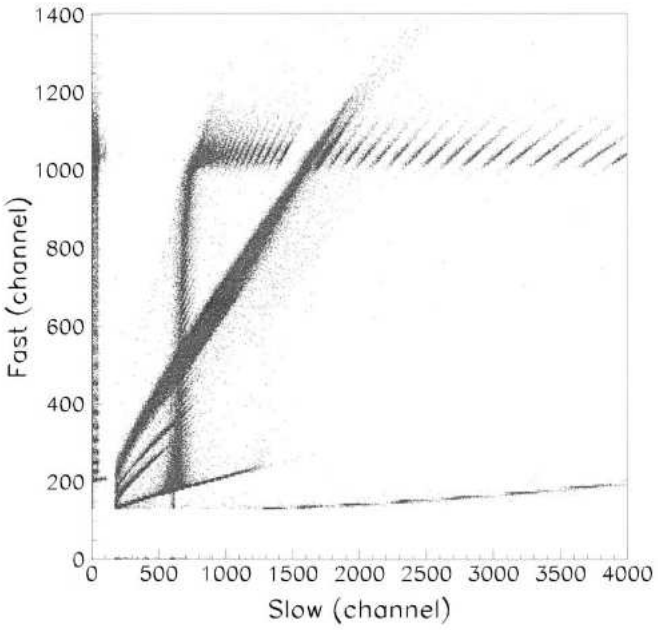

FIGURE 4.18: Fast–Slow identification scatter plot for a detector located at θ=1.4°. The observed lines with constant value of the fast component are due to spurious coincidences in different beam bursts. As can be seen in Fig. 4.17 the variation in the slow signal is due to the dependence of the position of the slow gate on the RF signal [84]. The vertical line corresponds to the case in which the gate is randomly sampling the fast signals at the edge of the flat/stretched part.

look also at the gate timing sketched in Fig. 4.17, in a wide range of the signal height [84].
By fitting the observed distribution of the events, corresponding to spurious coincidences with different beam bursts in Fig. 4.18, one can determine the dependence of the slow component on the time jitter of the signal. This information was used to study the effect of the signal jitter on particle identification resolution.
Spurious coincidences generated by cosmic rays obviously generate a noise in the fast-slow scatter plots. In order to evaluate such random contribution, one can simply integrate a region of the fast-slow plot far from good identified particles, as it is reported in Chapter 5. In the paper [84] the authors underlined that the main advantage obtained using the RF signal as time reference is a significant reduction of the identification thresholds. With a standard method, based on the time of CsI(Tl) detectors as reference time, indeed, the charge identification threshold for proton and α particles was above 8 MeV, whereas in this way the authors obtained a threshold for protons of about 4–5 MeV.

4.1.7 γ-rays detection and identification

CHIMERA is essentially a detector for charged particles and it can not compete, from the point of view of resolution, with very powerful germanium arrays in construction as AGATA or GRETA [94, 95] or with less performing germanium arrays as for instance EXOGAM, MINIBALL and GALILEO [96–98].
However due to the 4π coverage of the Si–CsI(Tl) telescopes and the simultaneous efficient detection of charged particles and γ-rays, on a large solid angle, CHIMERA can produce very interesting results, providing the adoption of appropriate detection methods [99].
As stated above, the second stage of CHIMERA is built with CsI(Tl) crystals, coupled with read out photodiodes, and having thickness ranging from 12 cm, in most forward detectors, to 3 cm , at backward angles. The CsI(Tl) stage of the telescopes is also suitable to detect γ-rays due to the high atomic number of the material, producing a relatively large efficiency.
The most useful part of CHIMERA for γ-rays detection is the CsI(Tl) stage of telescopes belonging to the spherical part of the detector. In fact, due to the larger solid angle coverage of the single detector and to the smaller yield of charged particles, we can benefit of a larger signal to noise ratio.
The method used for the detection and identification of γ-rays is based on the fast-slow method. The γ-rays in the CsI(Tl) generate electrons, that also at a low

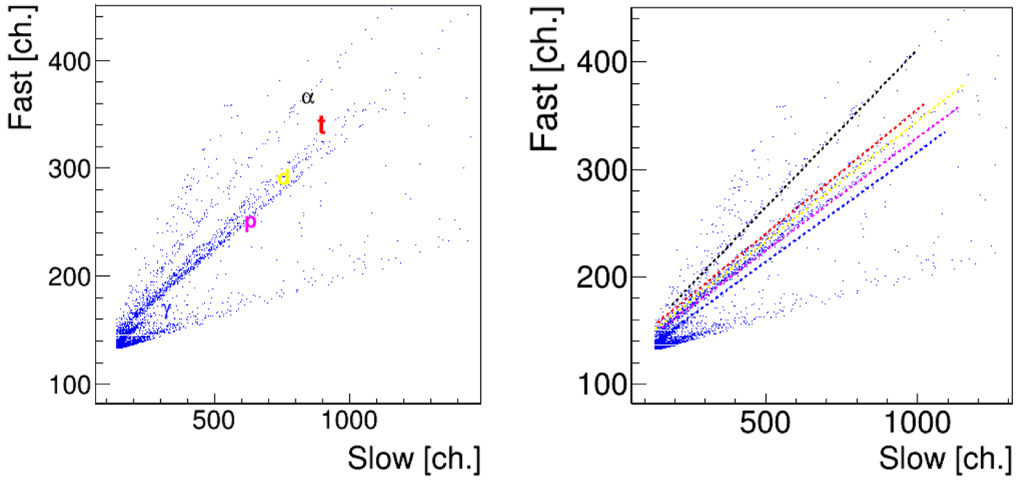

FIGURE 4.19: Left: fast-slow obtained in the Pygmy experiment, Right: the same fast-slow in which we plot also the identification lines to show the identification procedure.

energy are relativistic particles. Such electrons have a dE/dx very low comparing with other charged particles. This means that considering the same energy of another charged particles (for example a proton), namely the same fast component, such electrons will have a bigger slow component. This allows to understand that the line corresponding to γ-rays is placed just under the line of protons [100].
The identification procedure consists in performing the fast-slow plots, for each telescope of the CHIMERA array. An example of fast-slow, obtained in the Pygmy experiment in which the timing of the MCP was used as a reference time, is shown in Fig. 4.19 (left).
For each fast-slow plot we draw lines, each of them corresponding to a particular region, for example the region in which we observe γ-rays, protons, α and also other charged particles, as indicated in Fig. 4.19 (right). An analysis program, realized by the CHIMERA collaboration and based on the KaliVeda analysis program [101], allows to construct grids of identification. For each line, that corresponds to a particle identification, are then attributed codes corresponding to a good identification, as well as the mass and the charge of the particle. In Fig. 4.19 (left) it is possible to see light charged particles and the region corresponding to γ-rays. In Fig. 4.19 (right) it is shown the fast-slow and also the lines corresponding to the particles identification, in order to show in a schematic way the identification procedure.

4.1.8 Neutron detection

The simultaneous detection of neutrons, γ-rays and charged particles represents an important experimental progress for future experiments performed with both stable and exotic nuclei.
The possibility to detect neutrons with the CHIMERA array has been underlined also in ref. [84], indeed in this paper the authors underlined that the influence of the ToF on the fast-slow identification scatter plots have interesting consequences, allowing one to observe signals produced by neutrons that interacts with CsI(Tl) detectors.
In order to investigate about this possibility, Monte Carlo simulations have been performed and compared with experimental data [102].
The experimental method is based on the detection of charged particles that are produced by the interaction of neutrons with CsI(Tl) detectors. This method can be applied in two different ways:

- detecting charged particles in CsI(Tl) detectors imposing that in Si detectors we do not have any signals. This method allows to use all CsI(Tl) detectors, but a very careful analysis have to be performed in order to remove some light particles whose energy loss in Silicon is below thresholds
- detecting charged particles in CsI(Tl) detectors covered by ancillary detectors coupled to the CHIMERA array, as for example, the FARCOS array.

First results about the neutron detection have been obtained considering the CHIMERA telescopes covered by the FARCOS array [102], indeed in this way only γ-rays and neutrons can be detected in those CHIMERA telescopes.
A comparison between the experimental fast-slow obtained considering a telescope covered by FARCOS and a telescope not covered by FARCOS is shown in Fig. 4.20 [102]. A preliminary comparison between simulations and experimental spectra of charged particles (p, d, α) as detected in the CsI(Tl) which are in the shadow beyond FARCOS is shown in Fig. 4.21 [102].
In the Chapter 5 we will show some preliminary results in order to extract the information about the neutron decay channel of the PDR.

4.1.9 CsI(Tl) calibration

The first stage of data analysis for the CsI(Tl) was the energy calibration. For this purpose we used a proton beam accelerated by the TANDEM of INFN-LNS at an

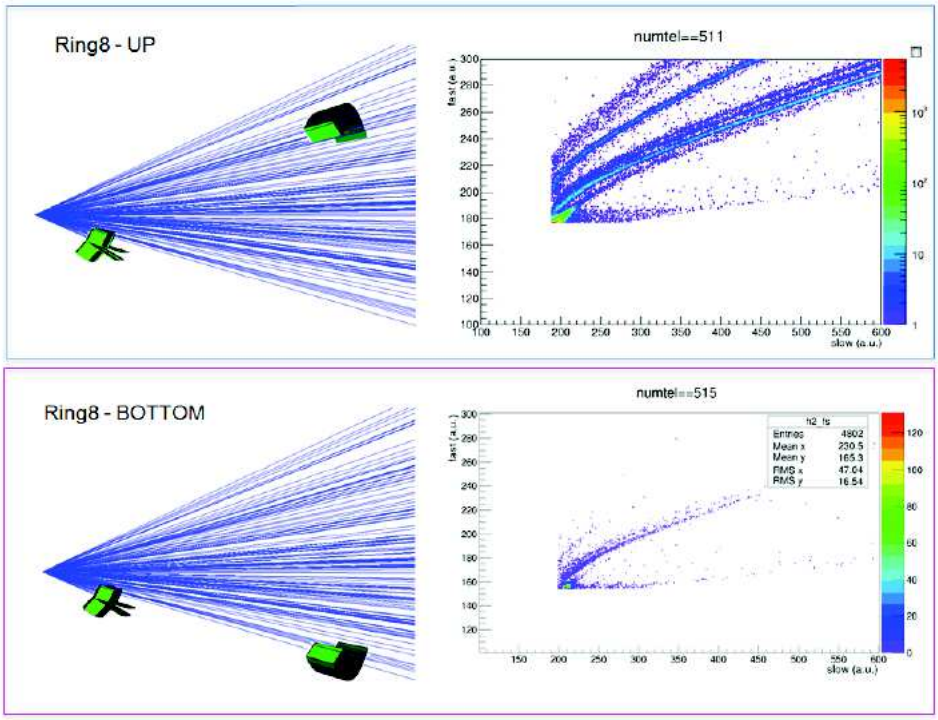

FIGURE 4.20: Fast-slow for CsI(Tl) detectors in the telescope 511 (covered by FARCOS) and 515 (not covered by FARCOS)[102].

energy of 24 MeV, and several targets of ^{12}C, ^{197}Au and CH_2. We used the elastic and inelastic reactions of proton beam as well as pulser signals to calibrate the detectors in proton-equivalent energy and also to verify the linearity of the response function.

As an example, we show in Fig. 4.22 (left) a ΔE-E plot, obtained for a telescope of the CHIMERA sphere, in the case of p+ ^{12}C reaction at 24 MeV. In this figure it is possible to observe several bumps corresponding to the elastic and inelastic channel reactions. In Fig. 4.22 (right) we plot the energy projection, observing several peaks.

From the Fig. 4.22 (right) we can extract the centroid for each observed bump. Such bumps correspond to the elastic channel (green region), the 4.44 MeV level (blue region), the 7.7 MeV level and the 9.64 MeV level (brown region) of ^{12}C.

In this way, we were able to perform the energy calibration, as shown in Fig. 4.23. Having obtained the energy calibration we were able to determine the Q-value. In Fig. 4.24 (a) we plot the Q-value spectrum for the p+ ^{12}C reaction, considering all the detectors of the CHIMERA sphere.

At this point, we performed coincidence measurements of γ-rays in coincidence

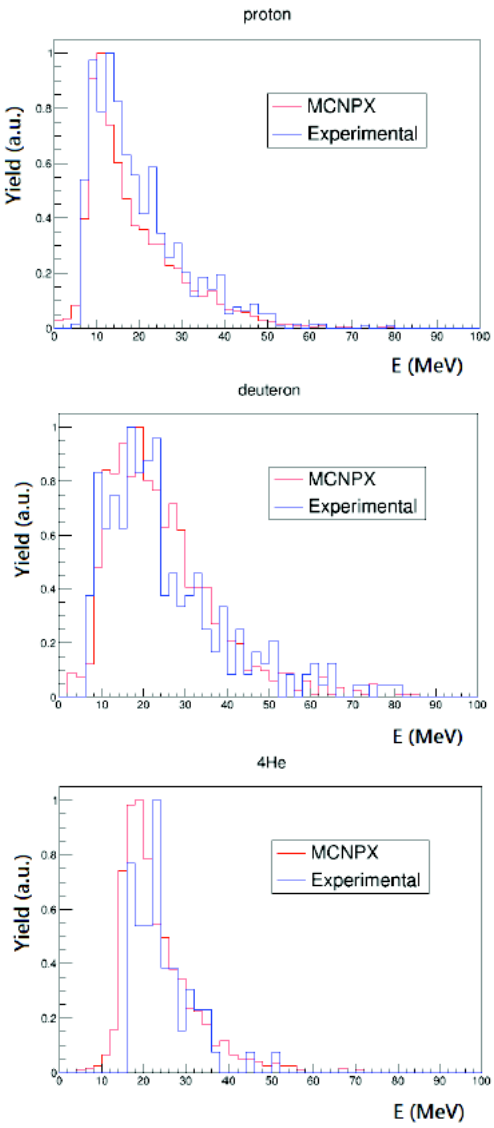

FIGURE 4.21: Comparison among MCNPX [103] and experimental energy spectra of light charged particles detected in the CHIMERA CsI(Tl) detectors in the shadow of FARCOS [102].

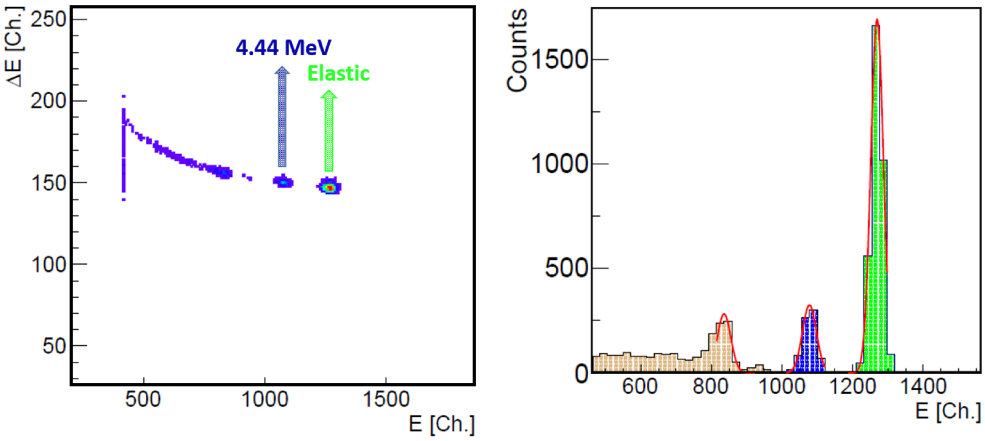

FIGURE 4.22: Left: ΔE-E plot obtained for a telescope of the CHIMERA sphere in the p + ^{12}C reaction at 24 MeV. Right: Projection on the fast (E) axis, shown in the left panel, with the Gaussian fit performed on each bump.

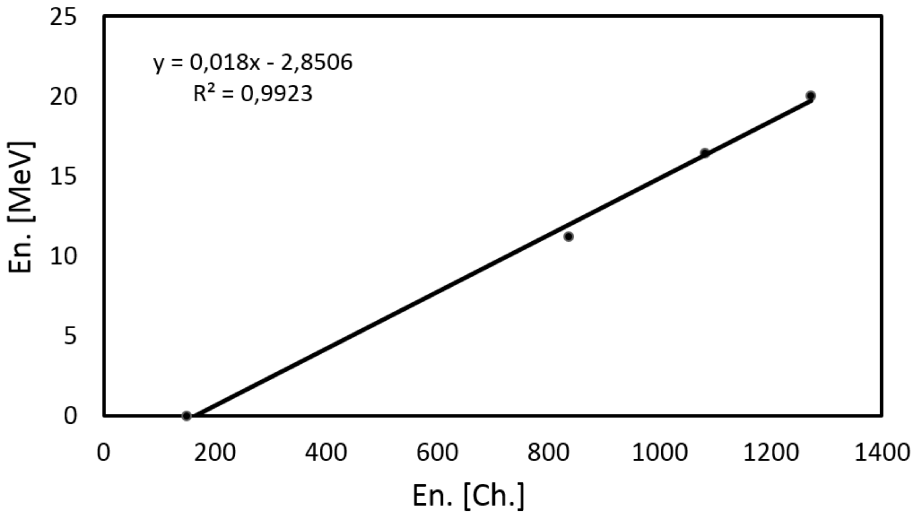

FIGURE 4.23: Linear calibration for protons, obtained for a telescope of the CHIMERA sphere.

with protons. This procedure allows also to correct the energy calibration for protons, measuring their quenching, in order to obtain the γ-rays energy calibration. In Fig. 4.24 (b) we plot the γ-ray energy spectra in coincidence with the two different windows of Q-value. The two colored regions correspond to the elastic (green) and the inelastic channel (yellow) [104]. The latter is associated to the 4.44 MeV level produced in the ^{12}C decay. The background under this peak was evaluated by means of the coincidence with the elastic channel (green spectrum). The subtraction of the two spectra is shown in Fig. 4.24 (c).

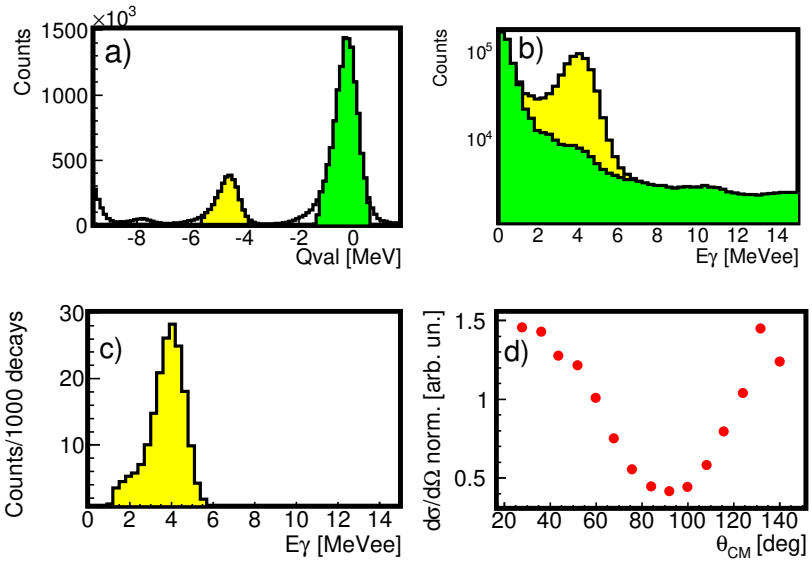

FIGURE 4.24: a) Q-value spectrum for the p + ^{12}C reaction. The elastic (green) and the inelastic peaks (yellow) are well separated. b) Energy spectra of γ-rays detected with the CsI(Tl) of CHIMERA, in coincidence with the inelastic (yellow peak) and the elastic channel (green peak) of the p + ^{12}C reaction. c) Energy spectra of γ-rays detected with the CHIMERA CsI(Tl), resulting from the subtraction of the two γ-ray spectra shown in panel b). d) γ- ray angular distribution for decay of the 4.44 MeV level.

This calibration was also used to extract γ-ray angular distributions; the one corresponding to the decay of the 4.44 MeV level is plotted in Fig. 4.24 (d). The observed trend is in agreement with a typical distribution for a $2^+ \rightarrow 0^+$ transition, see ref. [99] for details.

Moreover, as anticipated in Chapter 3, we want to highlight that we do not observe γ-rays in the region around 10 MeV, where the PDR is expected, due to the decay of ^{12}C. This is due to the very low γ-decay branching ratio of high-energy levels in ^{12}C [64].

We also underline that the γ rays can not be discriminated from particles in experiments performed with the TANDEM accelerator, this results in the large background shown in Fig. 4.24 b), while for fragmentation beams the fast-slow identification technique was possible by using the MCP signal as the starting time for the slow gate [84].

4.2 FARCOS array

In this section we describe the FARCOS array and the detection of the ^{68}Ni as well as other heavy ions fragments, produced in the reaction with the ^{12}C.
FARCOS (**F**emtoscope **AR**ray for **CO**rrelations and **S**pectroscopy) [70] consists of a new array that is designed and constructed inside the INFN-NEWCHIM experiment and supported by the INFN- Commissione Nazionale Scientifica III from 2015 to 2019. The original idea [70, 71, 105, 106] has been developed inside of the CHIMERA-EXOCHIM collaboration, with researchers and technical staff from the INFN - Sezione of Catania, Milano, Laboratori Nazionali del Sud, University of Catania, Milano, and including the participation of researchers from France, Spain and USA.
FARCOS will be a compact and relatively small-solid angle detection system, characterized by both high angular and energy resolution, with the peculiarity to be movable in a rather simple way and to be coupled to different detector systems.
It is possible to use FARCOS together with the CHIMERA detector [68] or with other existing and developing devices (as for example INDRA [107], GARFIELD [108], FAZIA [109], MUST2 [110], TRACE [111]), covering different angular regions, depending on the physics case, on the beam energy and on the kinematics of the reaction.
FARCOS is thought mainly to be used in the studies of correlations between charged particles, in reactions at low and Fermi energies, as well as in spectroscopic and in femtoscopy studies, in order to extract information about the space-time properties of nuclear reactions. Several analysis techniques have indeed allowed to get valuable information on the size (volume, density) of particle emitting sources, produced during heavy-ion collisions, as well as their lifetimes [112]. Typically these measurements are performed with dedicated arrays of silicon and scintillator crystals, covering a specific portion of the accessible phase space in the reaction. FARCOS indeed is composed by Silicon and CsI(Tl) detectors, and this choice

is based on the previously used devices at several beam energy regimes. Among them, we mention the LASSA silicon strip and cesium iodide array [113],the HodoCT hodoscope [114, 115] constructed by INFN Catania and Milano and used for particle-particle correlation measurements, as well as the HIRA detector, that is a set of charged particle detectors [116].
Moreover, the availability of 4π CHIMERA detector allows to get a unique tool to characterize the whole collision event in terms of impact parameter, reaction plane, and to extract important information about the dynamic and time-scale of fragment emission [117].

4.2.1 Silicon and CsI(Tl) detectors of the FARCOS array

FARCOS is a modular array of telescopes arranged in a single cluster, each of such telescopes consists of three detection stages. The first two stages are two Double Sided Silicon Strip Detectors (DSSSD) 300 μm and 1500 μm thick respectively. Each DSSSD has an active area of 6.4 $\times$ 6.4 cm^2, 32 vertical strips in the front side and 32 horizontal strips in the back side.
The 2 mm strip size represents a good compromise between the granularity and the loss of efficiency due to inter strip dead region (nominal 25 μm on the junction side and 40 μm on the ohmic side). Also the thickness of the first stage of 300 μm is a good compromise between threshold requirements for particle identification with the ΔE-E method and the expected large capacitance noise introduced by a thinner Si detectors. The thickness guarantees a large energy loss for light particles, that is very important for the energy calibration, an easier particle identification, and a good trigger efficiency. More in detail for the FARCOS prototype we used the BB7 Micron detector shown in Fig. 4.25.
The last stage of a FARCOS telescope consists of four CsI(Tl) crystals (3.2 $\times$ 3.2 cm^2) with 6 cm of thickness, read by a photodiode (18 $\times$ 18 mm^2). The simple choice, performed at the beginning of the project, to have such CsI(Tl) detectors was justified because it was not fixed yet the distance of the prototype from the target. This has an obvious consequence, that high energy particles impinging on silicon strips, near the external side of the detectors, can go out from the CsI(Tl) and the measurement of their energy will be wrong. On the other hand, because of the finite size of Silicon strips, some typical known problems arise for the good definition of the effective solid angle of the first and last strips in matching the two silicon stages. However, the more external strips generally suffer of a larger noise with respect the internal ones and are often excluded from the analysis, it is indeed

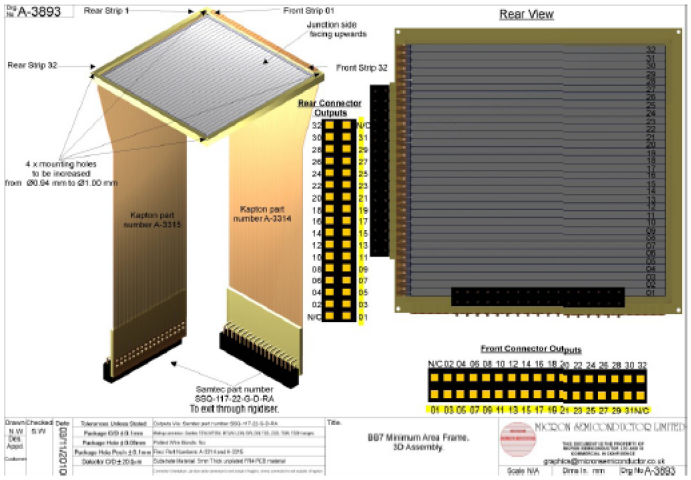

FIGURE 4.25: Mechanical draw of the BB7 silicon strip detectors used for the FARCOS prototype.

very important to save data coming from the second and 31st strips.
In Fig. 4.26 we show a scheme of one assembled cluster. In particular, in the left image we show one of the FARCOS telescope assembled, while in the image on the right are shown the components of each telescope: the two DSSSD and the four CsI(Tl) crystals [118].

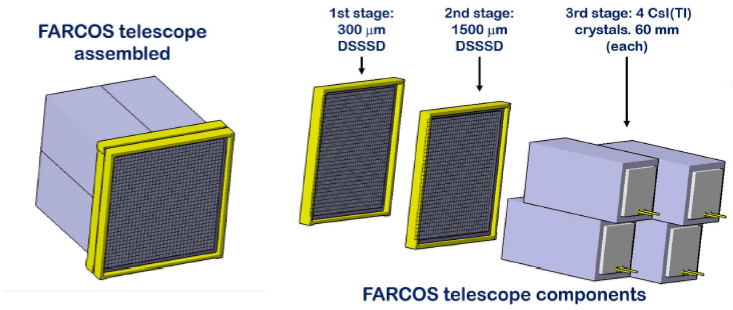

FIGURE 4.26: Left: the image shows one of the FARCOS telescope assembled. Right: the image shows the components of each telescope [118].

Behind each telescope we placed a liquid-cooled copper block (Fig. 4.27), in order to thermally stabilize the CsI(Tl) preamplifiers.
At the time of the experiment FARCOS was constituted by four telescopes, each of them having the characteristics mentioned above. The use of FARCOS in coincidence mode with other existing detectors requires the development of a special mechanical support, which allows to obtain different geometric configuration with

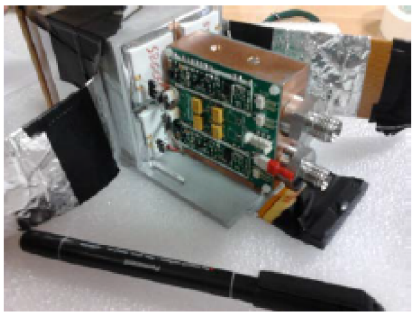

FIGURE 4.27: Copper block placed behind each telescope, in order to support and cool the four CsI(Tl) preamplifiers.

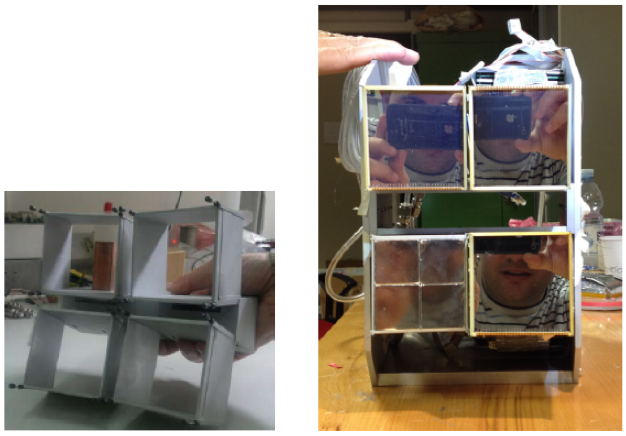

FIGURE 4.28: Left: Mechanical support used for the FARCOS prototype, composed by four telescopes. Right: photo of the support with the mounted four telescopes.

the minimal amount of dead solid angle. In Fig. 4.28 (left) it is shown the support used for the FARCOS prototype, in Fig. 4.28 (right) it is shown a photo of the support with the mounted four telescopes.

4.2.2 FARCOS configuration for the Pygmy experiment

For the Pygmy experiment FARCOS was used to detect and isotopically resolve the ions coming from the interaction with the target of ^{12}C. This measurement was therefore a first constraint to the mass of the detected nuclei.
During the Pygmy experiment FARCOS was placed just after the sphere of the CHIMERA array, covering θ angles from 2 $^\circ$ to 7 $^\circ$ and with about the 70 % coverage of the azimuthal angles, as also described in the Chapter 3 and in Fig. 3.2. The experiment was performed using the standard CHIMERA Front End electronics. In particular, we used part of the Pulse Shape modules, described in the previous

section 4.1.3. The electronics used for FARCOS , in the Pygmy experiment, was thus constituted by:

- Commercial MPR-64 Mesytec preamplifier with 1500 MeV of full-scale energy for 300 μm stage of telescopes
- Commercial MPR-64 Mesytec preamplifier with 1000 MeV of full-scale energy for 1500 μm stage of telescopes
- Analogue acquisition based on 16 channels NIM-CAEN Amplifiers and VME CAEN 64 channels QDC

The electronic chain for the CsI(Tl) detectors of the FARCOS array was the same of the one used for the CsI(Tl) detectors of the CHIMERA multidetector.

4.2.3 Identification method with the FARCOS array

In order to detect and identify ions with the FARCOS array we used the standard ΔE-E method. For a charged ion that punches through the first step of a telescope, the signal coming from the first step is used as energy loss ΔE, while the signal coming from the second stage is used as residual energy E_R signal.
The sum of these two quantities gives the total kinetic energy of the ion. The combination between the two quantities allows to identify the atomic number z of particles produced in the reaction. This procedure is based on the Bethe-Bloch formula for the specific energy loss of a charged particle in matter defined as [73, 100]:

$$-\frac{dE}{dx} = K\rho\frac{Z}{A}\frac{z^2}{\beta^2}\left[ln\left(\frac{2m_e\gamma^2v^2W}{I^2}\right) - 2\beta^2 - \delta - 2\frac{C}{Z}\right] \tag{4.3}$$

In such formula x represents the thickness of the considered medium, K is a constant value of 0.1535 $MeV\ \frac{cm^2}{g}$, ρ is the density of the absorbing material, Z is the atomic number of the absorbing material, A is the atomic mass of absorbing material, z is the atomic number of the incident particle, m_e is the electron mass, β= $\frac{v}{c}$ of the incident particle, W is the maximum energy transfer in a single collision, I is the mean excitation potential , γ= $\frac{1}{\sqrt{1-\beta^2}}$, C and δ represent two corrections, respectively the correction of shell and the correction of density.
In a classical approach, the specific energy loss of a charged particle in matter depends on the characteristic of the incident ion, as mass, charge and energy, and those of the absorbing medium, as density and atomic number.

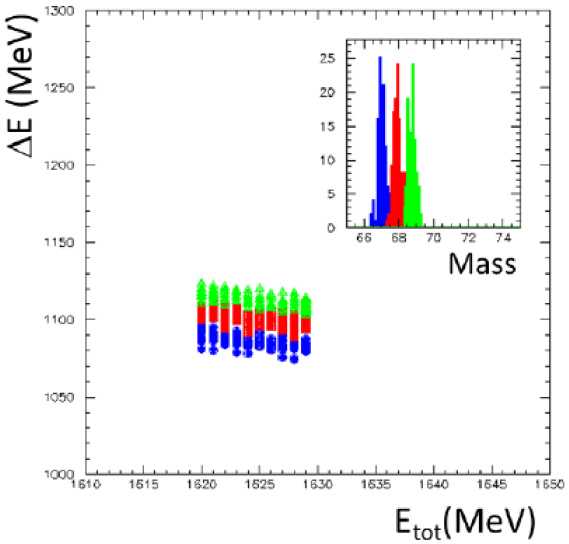

FIGURE 4.29: Simulation, performed with SRIM [119], of the energy loss ΔE against the total energy E_{tot} of nickel isotopes in the first two stages of a FARCOS telescope. In the inset the preliminary mass estimation for the ^{67}Ni, ^{68}Ni, ^{69}Ni is shown.

Plotting the energy loss in a detector, ΔE, as a function of the total or residue energy loss in another detector one obtains curves, each of them corresponding to a particular particle.

We performed simulations in order to understand the possibility to use the FARCOS array employing the ΔE-E method to detect ^{68}Ni as well as other heavy ions fragments. We considered the reaction products generated by the collision of the ^{70}Zn + ^{9}Be at 40A MeV, in this collision as discussed also in the Chapter 3 we obtain several isotopes. The simulations show that at the energies used in the experiment, considering also the interaction with the ^{12}C target, most ions deposit the total energy in the second stage of the FARCOS array, without reaching the CsI(Tl). In particular, the energy loss in the first stage of the FARCOS array by Ni ions is quite large, about 1.1 GeV, while the energy loss by the Ni ions in the second stage of FARCOS is about 500 MeV.

In Fig. 4.29 we show a simulation, performed with SRIM [119], of the energy loss against the total energy of nickel isotopes in the first two stages of a FARCOS telescope. In the inset is plotted the preliminary mass estimation. This simulation shows that the energy loss in the first stage is so large that one can have sensitivity to the mass identification in the ΔE-E plot. We performed also more complete LISE++ [74] simulations taking into account the envelop of beams and the effect of ^{12}C thick target confirming such results, as shown in Fig. 4.30. However, in this

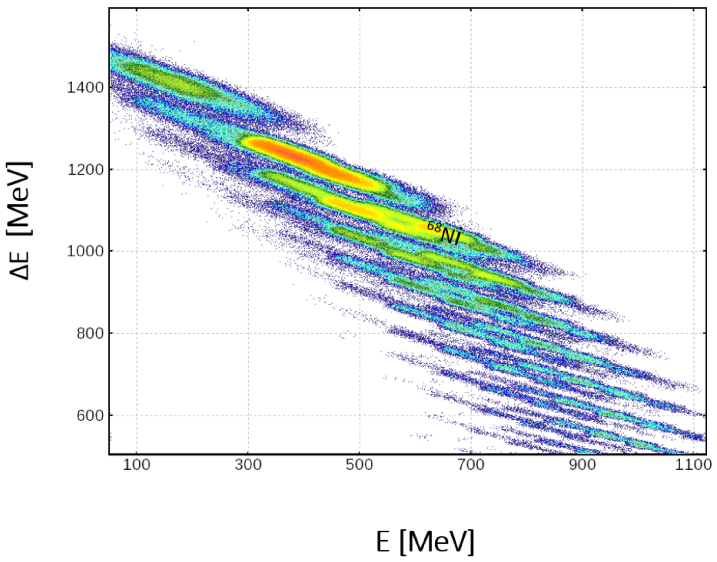

FIGURE 4.30: ΔE-E simulation of the energy loss in the first two stages of a FARCOS telescope, performed with LISE++ taking into account the envelop of beams. However, in this simulation we have not included the dipole after the MCP detector.

simulation we did not include the presence of the dipole after the MCP detector. In order to detect the ions produced in the reaction with the ^{12}C we performed several ΔE-E plots. Each plot was performed considering two correlated strips, between the 300 μm and 1500 μm front of DSSSD detectors. An example of ΔE-E plot, for two correlated strip, corresponding to the smaller θ angle covered by the FARCOS array is shown in Fig. 4.31. As it is possible to note in this figure we obtained a better identification with respect to the identification predicted with simulations. This good identification is due to the high quality of the FARCOS silicon detectors response, together with the cleaning effect of the fragment separator. Moreover, using the FARCOS array a quantitative analysis of the contamination of tagged beams was performed, as reported in the following.

We performed ΔE-E plots for correlated strips and for each plot we performed graphical cuts in order to select the region corresponding to a particular isotope. Moreover, in order to remove the events due to the inter strip effect we imposed a constraint on the time of observed isotopes. This was made at the beginning of the data analysis as condition to process the raw data.

During the experiment we used also a Au target with the ^{70}Zn primary and pilot

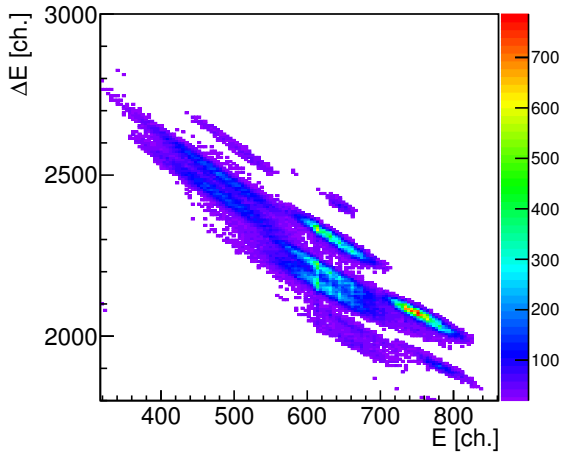

FIGURE 4.31: ΔE-E plot obtained with the FARCOS array, considering two correlated strips.

beams, in order to check the stability of the electronics, the transport and focusing of the beam.

In principle, the elastic reactions ^{70}Zn+ Au can be used to perform calibration of the FARCOS array. However due to the high energy and angular spread of the beam and due to some problems with the saturation of used preamplifiers, it was not possible to perform an energy calibration of the FARCOS array. For this reason we were forced to select the nuclei for each ΔE-E plot obtained with the FARCOS array, and due to the high quality of the DSSSD of the FARCOS array the identification of the ^{68}Ni as well as of other heavy ions was quite good, as will be better discussed in the Chapter 5.

Chapter 5

Decay channels of the PDR: results and discussion

In this Chapter we introduce the results and the discussion about the γ-rays decay of the Pygmy Dipole Resonance, moreover we present also some preliminary results about the neutron decay channel of the PDR.
The results about the γ-rays decay channel have been recently published in refs. [120, 121].

5.1 γ-decay channel

As mentioned in the previous Chapters, in order to investigate the γ-rays decay channel we used the nuclear interaction between the ^{68}Ni projectile at 28A MeV and the ^{12}C target. As shown by semiclassical calculations (Chapter 3), at this energy the Coulomb contribution is very low, but about the 30 % of the total cross section is due to the interference between Coulomb and nuclear contributions. Moreover, we have to take into account the contribution of the other multipolarities, that may influence the bump of the PDR. This contribution was evaluated performing also CASCADE calculations [122, 123], as discussed in the following.
The method used to investigate the γ-decay channel of the PDR is similar to the one used in ref. [55], in which the γ-ray spectrum was collected in coincidence with ^{68}Ni fragments.
In particular, we used a triple coincidence, looking for γ-rays detected in coincidence with the ^{68}Ni beam, detected with the tagging system, and the ^{68}Ni fragments, detected with the FARCOS array. Studying the Pygmy decay with γ-rays emission the excitation energy of the ^{68}Ni is not enough to emit also other particles, and therefore such triple coincidences increase the visibility of the γ-decay channel of the Pygmy resonance, as we will show better in the following.

In the inset of Fig. 5.1 (a) we show the ΔE-ToF plot obtained with the tagging system. The ^{68}Ni beam, evidenced by the black circle, is the most intense beam in the cocktail, about 20% of the total intensity. The beam energy after the DSSSD detector of the tagging system is about 28A MeV and, as discussed in Chapter 3, at this beam energy the ions identification is difficult, because of the presence of not fully stripped ions produced after the ^{9}Be target. However, we have shown in previous Chapter 3 that the configuration of the transport beam line, with the presence of magnets after the MCP, allows to reject the largest amount of this background by the stripping effect of the mylar foil. With this method we were therefore able to correctly identify the ^{68}Ni^{28+} beam.
In the section 4.2.3 it was already shown that FARCOS is able to perform isotopic identification of nickel fragments due to the high energy lost in the first silicon stage and the collection of the total energy in the second stage.
In Fig. 5.1 (a) a ΔE-E plot obtained with the FARCOS array is shown. The ΔE-E plot is plotted in channels, indeed, as described in the Chapter 4, due to the energy spread of the fragmentation beam (2 %), to the angular spread and due to some problems with the saturation of preamplifiers it was difficult to extract the absolute energy calibration.
In Fig. 5.1 (b) we show the ΔE-E plot obtained with the FARCOS array, in coincidence with the ^{68}Ni beam, shown as a black circle in the inset of Fig. 5.1 (a). From these figures one can better appreciate the presence of other nuclei in addition to the ^{68}Ni. We observe at smaller channels in the E stage a large percentage of the ^{66,67}Ni nuclei, also considering the coincidence with the ^{68}Ni beam (Fig. 5.1 (b)). Moreover, this analysis allows also to evaluate the presence of contamination of the tagged beam by ^{66}Ni^{27+} (14%), produced at similar energy with respect to the one of the main beam, and the ^{66}Cu^{28+} , produced at lower beam energy with a lower intensity (7%). Thanks to the isotopic resolution of the detection system, and to the energy difference of the various nuclei, the contaminants can be easily removed.

In Fig. 5.1 (b) excluding the beam contaminants we observe two main channels of reaction: one in which we detect ^{68}Ni and the other one in which we detect ^{66,67}Ni. The ^{68}Ni-^{68}Ni channel corresponds to the channel in which only γ-rays are emitted, indeed due to the angular coverage of the FARCOS array the elastic channel is completely lost in the hole of FARCOS, being the grazing angle about θ_{LAB}= 0.7 $^{\circ}$. The ^{66,67}Ni channel is due to either the decay of the ^{68}Ni with the emission of one or two neutrons or to transfer reactions with the target. Due to the energy used in the experiment and to the structure of the ^{12}C the probability to have this latter

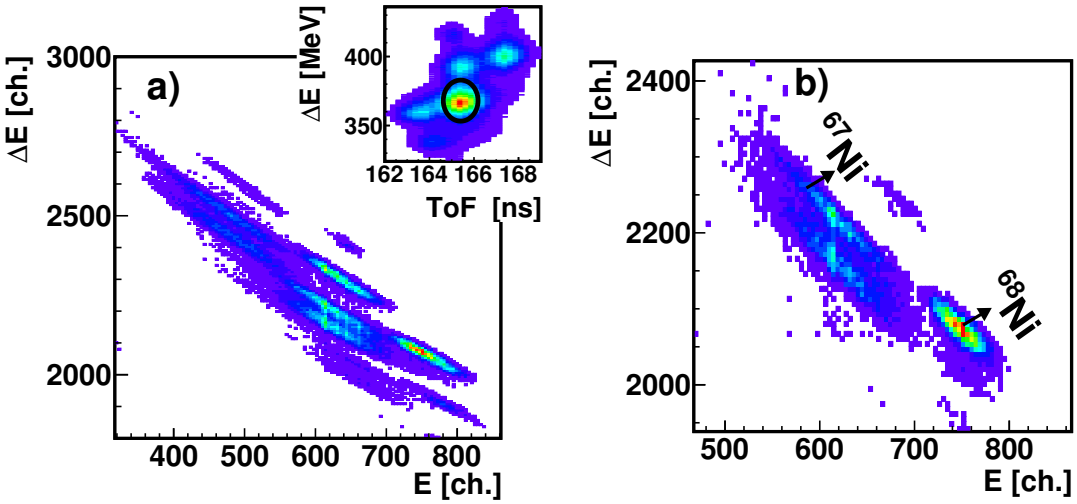

FIGURE 5.1: (a) ΔE-E scatter plot observed with the FARCOS array, irradiated by the reaction products produced with the whole fragmentation beam. The isotopic identification of fragments with Z from 27 to 30 is observed. In the inset the ΔE-ToF identification scatter plot of the cocktail beam is shown. (b) Reaction products detected with the FARCOS array in coincidence with $^{68}Ni^{28+}$ ions, as shown in the black circle in the inset of Fig. 5.1(a).

decay channel is lower with respect to the neutrons emission. A way to separate these two channels could consist in the collection of the coincidences spectra also with the ^{12}C target nuclei, detected in the CHIMERA multidetector. However, the ^{12}C nuclei lose the whole energy in the target thickness (75 μm).
Moreover, the ^{12}C has a low binding energy, this means that it is in any case difficult to detect the target because it decays, with a high probability, emitting particles.
In Fig. 5.2 (b) we show the γ-rays energy spectra, Doppler shift corrected, as described in the section 5.1.1, in coincidence with the Ni fragments, lying within a black ellipse in Fig. 5.2 (a). This means that in Fig. 5.2 (b) we show the energy γ-spectra in coincidence with the ^{68}Ni beam and the Ni fragments, which are mainly produced by the decay of the ^{68}Ni beam.
The blue spectrum shown in Fig. 5.2 (b) corresponds to the γ-rays well identified using the fast-slow method, as we discussed in Chapter 4. However, we can see that this spectrum extends to an energy region up to 20 MeV, this high energy region is due to spurious coincidences that are not well removed in the identification

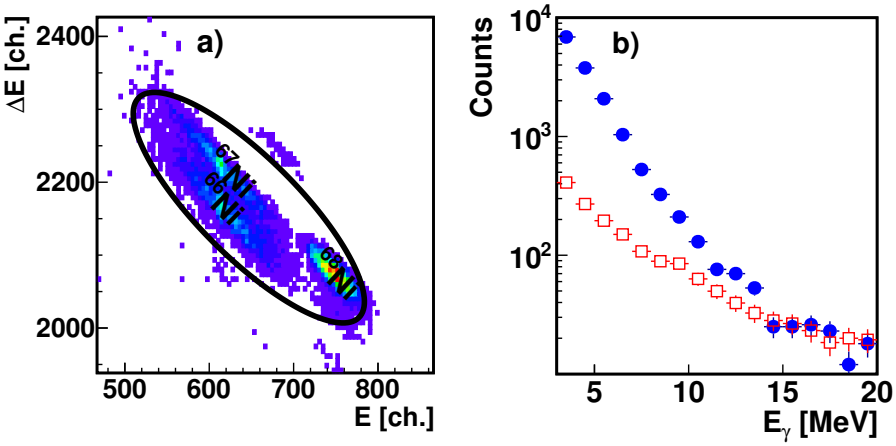

FIGURE 5.2: (a) ΔE-E plot obtained with FARCOS in coincidence with the $^{68}Ni^{28+}$ beam, detected with the tagging system. (b) Energy γ-spectrum obtained in coincidence with Ni fragments, inside the black ellipse in Fig. 5.2 (a). The blue spectrum corresponds to γ-rays correctly identified while the red one corresponds to spurious coincidences.

procedure. In order to subtract such spurious coincidences, we collected the energy γ-rays identified moving the fast-slow cuts around the γ-line (corresponding to the correct identification). This spectrum is plotted in Fig. 5.2 (b) as red squares.

The difference between these two spectra is shown in Fig. 5.3 (a). In this figure we display also two calculations performed using the statistical code CASCADE [122, 123]. The blue dashed curve corresponds to standard statistical calculations, obtained considering the statistical decay of ^{68}Ni nucleus with a range of excitation energies peaked at 26.5 MeV. The red curve corresponds to CASCADE calculations, obtained including the presence of PDR, GQR and GDR . The details of these calculations will be discussed in the section 5.1.2.
The blue curve fits only the first region of the energy γ-spectrum. This low energy region, indeed, is mainly dominated by the γ-yrast decay and consequently can be reproduced by a statistical decay. The high energy region is not reproduced since that, with this relatively low excitation energy range, the probability that the ^{68}Ni emits γ-rays in the higher energy region is very low. Starting from 7 MeV, representing the threshold of the neutron emission, we note that the experimental spectrum changes its slope.
At this point, we performed several CASCADE calculations in order to reproduce

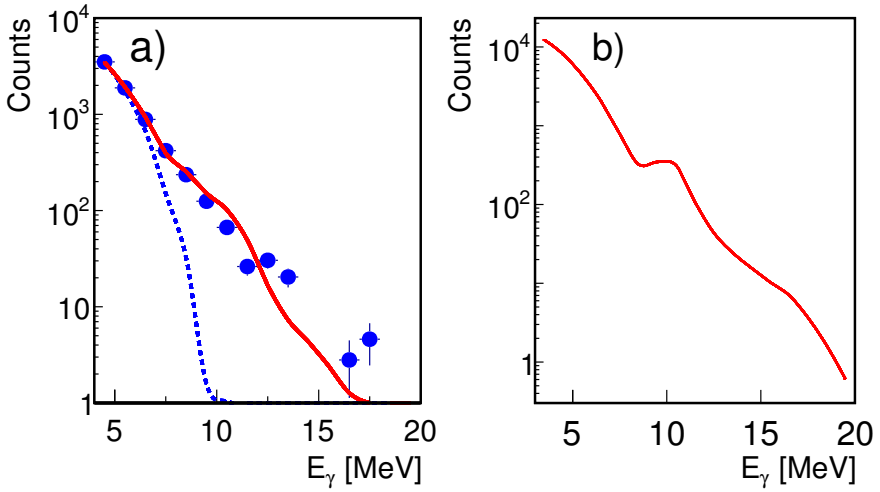

FIGURE 5.3: (a) Blue dots: energy γ-spectrum, Doppler shift corrected, obtained with the subtraction of the two spectra plotted in Fig. 5.2 (b). The blue dashed curve corresponds to standard statistical calculations, obtained considering the statistical decay of the ^{68}Ni nucleus populated with a range of excitation energies peaked at 26.5 MeV. The red full curve corresponds to CASCADE calculations, obtained including the presence of PDR, GDR and GQR. (b) CASCADE calculations obtained including the PDR, the GDR and the GQR without the folding with the detector response.

TABLE 5.1: Values of the PDR, GQR and GDR inserted in the CASCADE calculations.

Excitation mode	E [MeV]	Width [MeV]	Strength %
PDR	10	2	E1 9
GQR	16	1.5	E2 100
GDR	17	6	E1 91

the experimental spectrum also in the high energy region. We included in these CASCADE calculations the presence of the Pygmy Dipole Resonance, the Giant Dipole Resonance and also the Giant Quadrupole Resonance.
The population of the Isoscalar Giant Monopole Resonance (ISGMR) and Isoscalar Giant Quadrupole Resonance (ISGQR) have been studied for the ^{68}Ni in refs. [124, 125]. At the energy of 28A MeV, the cross section for the population of the ISGMR, as shown by semiclassical calculations (Chapter 3), is very low and moreover this mode can not decay, at least at the ground state, by γ-rays emission. For these reasons we neglected this transition in the CASCADE calculations. Whereas, we included in the statistical calculations the presence of the GQR, considering the values reported in refs. [124, 125]. We also underline that while resonances must be explicitly inserted, standard accepted constant strengths of other transitions are included in CASCADE.
The CASCADE calculations have been performed also by changing the strengths for the PDR and the GDR with the condition to preserve their total EWSR. The better agreement of calculations with experimental data was obtained with the values reported in the Tab. 5.1, obtaining an error for the PDR strength of about 2 %. Regarding the extracted widths we underline that they are strongly affected by the energy resolution of CsI(Tl) previously discussed.
The CASCADE calculations plotted in the Fig. 5.3 (a) are obtained considering the folding with the response function of used experimental set up, and including the correction for the solid angle and the malfunctioning detectors. The folding procedure is discussed in the section 5.1.3. Due to the low energy resolution of the CsI(Tl) and due to the presence of other decays, in Fig. 5.3 (a) the bump corresponding to the Pygmy decay can not be visible and its presence can be evidenced just by comparison with statistical calculations and observing a change in the slope of the spectrum. To have an idea about the folding effect we show in Fig. 5.3 (b) the CASCADE calculation without the folding procedure. In this figure the bump of the PDR at about 10 MeV is evident, whereas the bumps corresponding to the GQR and GDR are not so evident, their presence produces only a small change in

the slope.
This procedure allows to evaluate the statistical decay of the ^{68}Ni, mainly evident in the low energy region and the probability that other multipolarites may influence the bump at around 10 MeV. Moreover, in this way we are able to estimate the strength of the PDR.
A better experimental evidence of the PDR population can be obtained by comparing the γ-ray energy spectrum measured in coincidence with the ^{68}Ni channel with the γ-ray energy spectrum in coincidence with the ^{66,67}Ni channels. At this low excitation energy the high energy γ-decay of the PDR hinders further particle decay. On the contrary, if one or more neutrons are emitted by the system, the high energy γ-rays decay is inhibited. For these reasons, we compare in Fig. 5.4 (a) the γ-rays energy spectrum (blue dots) in coincidence with the ^{68}Ni, with the one measured in coincidence with neutron decay channels ^{66,67}Ni. The two spectra are normalized in the low energy region. Also these spectra are Doppler shift corrected by assuming an emission from the projectile. The background was evaluated and subtracted with the fast-slow cuts, as shown in Fig. 5.3 (a).
We note in Fig. 5.4 (a) the enhancement at about 10 MeV, as it was expected, due to the PDR decay of the ^{68}Ni isotope. We observe also a relatively small yield in the GDR high energy region as predicted by the semiclassical calculations. Indeed, these calculations (Fig. 3.1) show that, at these relatively low incident energies and with the low Coulomb field of the target, the excitation probability for the PDR mode is higher than the one corresponding to the GDR. The small yield is however also due to the lower detection efficiency in the higher energy region.
We underline that it is not possible to compare the exclusive energy spectra of Fig. 5.4 with inclusive CASCADE calculations (Fig. 5.3). However, one can compare the γ-rays spectrum in coincidence with ^{68}Ni, with γ-rays first step spectra generated with CASCADE, namely with the γ-rays emitted as first particles in the decay process. In fact, such events at the low excitation energy of the system produce only ^{68}Ni nuclei. This calculation, performed with the same parameters of Fig. 5.3, and folded with the CsI(Tl) response function, is plotted as blue full line in Fig. 5.4 (a). The comparison is quite good and the calculation reproduces the bump in the energy region of the PDR. Clearly, in this calculation, the lower energy spectrum is not reproduced because in this energy region the contribution of the decay of discrete levels in the final decay steps is missing.
In Fig. 5.4 (b) we report the PDR cross section obtained by subtracting the two normalized spectra of Fig. 5.4 (a). This method allows to give a lower limit to the PDR cross section, because some small PDR contribution could be present also in

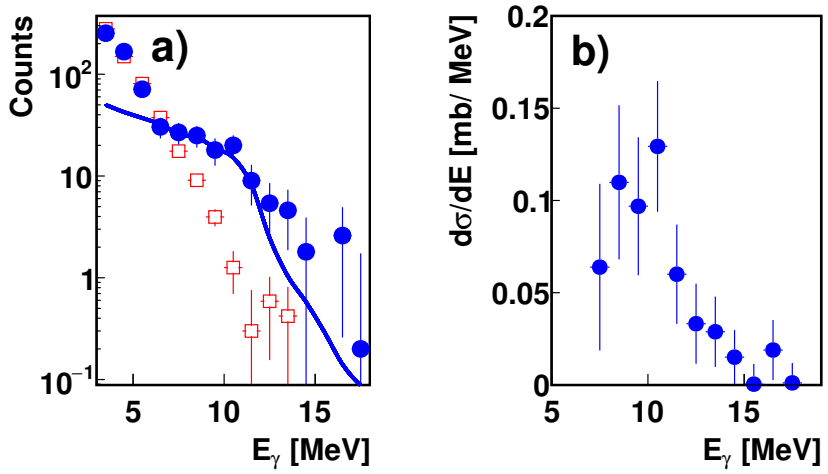

FIGURE 5.4: (a) γ-rays energy spectra Doppler shift corrected. The blue dots represent the coincidence with ^{68}Ni. The red squares represent the γ-rays energy spectrum in coincidence with ^{66,67}Ni. These spectra have been normalized at the low energy region. The blue full line is the γ-rays first step spectrum obtained with CASCADE. (b) Cross section of the PDR obtained considering the difference of the two spectra shown in Fig. 5.4 (a).

the ^{66,67}Ni coincidence spectrum. However this is the simplest way to compare the PDR yield with previous experimental results [55] and look to the presence of isospin splitting above particle emission threshold. The cross section is obtained taking into account the detection efficiency, as better specified in the following.
It is very important to verify the E1 character of the observed bump at around 10 MeV in coincidence with the ^{68}Ni channel, in order to prove the dipole character of the transition. To prove this we extracted the angular distribution of the emitted γ-rays in the region of the enhancement at around 10 MeV shown in Fig. 5.4 (b). The granularity of the spherical region of the CHIMERA multidetector, covering angles from 30° to 176°, in step of 8° up to 146°, allows to extract the angular distribution. Since the relatively low statistics, we were forced to sum γ-rays detected in two rings of the apparatus, therefore the effective laboratory angular resolution was $\pm 8°$, being negligible the error in the evaluation of the ^{68}Ni scattering angle assumed as reference axis. This angular distribution is shown in Fig. 5.5 (a). Despite of the scarce statistics, the angular distribution shows the typical distribution expected for a dipole transition, with a maximum around 90° (full blue line) [99]. As it is known, other multipolarities show a different angular distribution,

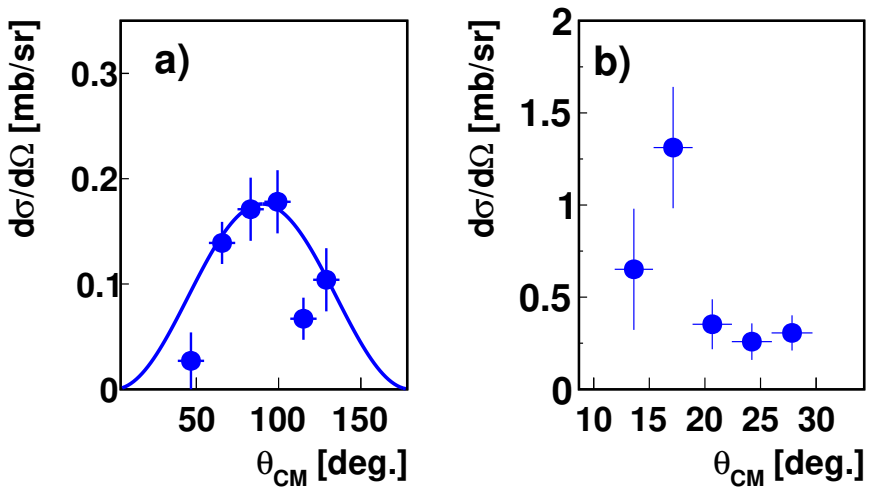

FIGURE 5.5: (a) The measured γ-rays angular distribution. The line is the expected E1 angular distribution. (b) The ^{68}Ni angular distribution measured in coincidence with γ-rays in the region of the Pygmy resonance.

for example in the case of a 2^+ state the angular distribution presents a minimum at around 90° (see also Fig. 4.24) [104]. The angular distribution was corrected for the effective γ-rays detection efficiency evaluated using GEANT4 simulations at 10 MeV, taking into account the thickness of CsI(Tl) scintillators of the sphere, mounted at different angles and malfunctioning detectors. On average the total γ-ray detection efficiency was of the order of 25 %.

In order to evaluate the overall detection efficiency it is also important to determine the angular distribution of the emitted ^{68}Ni in coincidence with the PDR enhancement. Unfortunately, due to losses in efficiency of the PPAC detector we did not have the information on the beam trajectory for all the events. However, the beam divergence was rather low, of the order of 0.5°; therefore by assuming this error in the angular distribution (and a further 0.2° due to the angular straggling in the thick ^{12}C target), and correcting for the average beam direction that can be evaluated by the impinging position in the DSSSD, we were able to evaluate the angular distribution which is plotted in Fig. 5.5 (b). We note that the largest part of the events is collected from 12° to 20°, with a maximum around 15° in the CM reference frame. The overall beam efficiency was calculated with a Monte-Carlo simulation, by using the measured beam distribution. Taking into account the observed angular distribution, one can evaluate an average efficiency for the ^{68}Ni

detection of the order of 52%.
We can not extract much more physical information from the ^{68}Ni angular distribution, shown in Fig. 5.5 (b). In fact, to perform meaningful DWBA calculations we should also have the measured elastic scattering angular distribution in order to fix the optical potential. However, the ^{68}Ni angular distribution is important for evaluating the ^{68}Ni detection efficiency and it may be a reference point for future measurements.
The cross sections of the Pygmy γ-rays decay shown in Fig. 5.4 (b), Fig. 5.5 (a) and Fig. 5.5 (b) are obtained thanks to the event-by -event counting of the beam intensity and the knowledge of target thickness, once determined the detection efficiency. In total, we counted about 1.4×10^9 ^{68}Ni beam particles detected with the tagging system.
Taking into account the average beam detection efficiency (52 %) and the average γ-ray detection efficiency (25 %), the total cross section of the PDR γ-decay amounts at 0.32 mb with a statistical error of the order of 18 %.

5.1.1 Doppler correction

If an excited nucleus decays in-flight with $\beta = v/c > 0$, the energy of the deexcitation γ-rays measured in the laboratory frame will be Doppler shifted. To correct the energy of γ-rays emitted by the ^{68}Ni we used the following equation:

$$E_{corr} = E_{lab} \frac{(1 - \beta cos(\theta))}{\sqrt{(1 - \beta^2)}} \tag{5.1}$$

where E_{lab} is the energy of γ-rays in the laboratory frame and θ is the angle between the velocity of the projectile and the velocity of γ-rays.
We applied this correction off-line, with the analysis based on the TTree of root [126]. Because of we did not have the energy calibration for the ^{68}Ni we were forced to assume a constant value of $\beta \approx 0.235$. As can be seen in Fig. 5.6 the Doppler correction effect is not dramatic at this β value.

5.1.2 CASCADE calculations

In order to study the statistical decay of ^{68}Ni and to subtract the low-energy region of the spectrum shown in Fig. 5.3 (a), we performed statistical calculations using the CASCADE code [122, 123]. We used this code also to extract parameters about the PDR contribution.

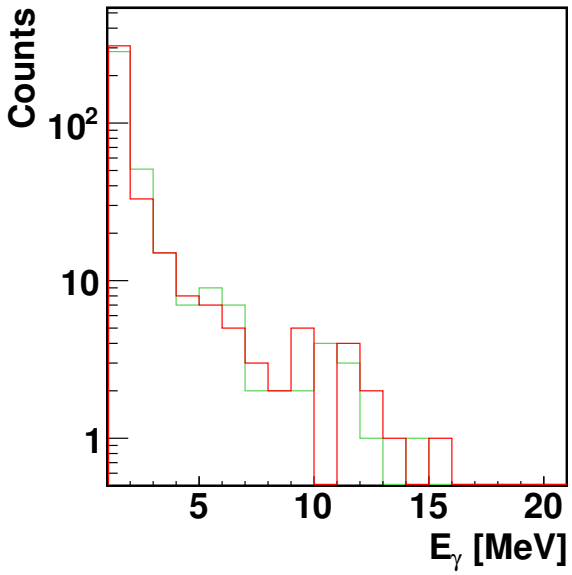

FIGURE 5.6: Energy γ spectrum without Doppler correction (red) and energy γ spectrum Doppler shift corrected (green).

First of all, we performed several calculations at different excitation energies using the standard input for these calculations, with a spin distribution peaked at low-spin values [122]. Among the standard input we underline that we used a standard value for the level density (A/8). The range of excitation energies has been fixed considering two main aspects: reproduce the slope of the observed γ-rays energy spectrum and reproduce the observed charge distribution.
As can be observed in Fig. 5.2 (a) in the reaction under consideration, nuclei with mass until 66 are produced. Therefore, we performed calculations in order to have the mass of residual nuclei $\geq$ 66. In Fig. 5.7 we show CASCADE calculations performed at several excitation energies from 24 MeV up to 28 MeV.
The 24 MeV and 28 MeV curves correspond respectively to the lower and higher limits, necessary to reproduce the observed charge distribution and the slope of experimental spectrum. The CASCADE calculations have been normalized at the experimental spectrum in the low energy region E $\approx$ 3.5 MeV.
This procedure allows to fix the range of excitation energies, moreover the best agreement is obtained in the case of the excitation energy peaked at 26.5 MeV. However, since in an inelastic scattering experiment the range of excitation energies is not a narrow peak but a quite broad region we prefer to perform CASCADE calculations considering the energy range between 24 and 28 MeV with a maximum at 26.5 MeV, as shown as a blue curve in Fig. 5.7. The curve obtained in this

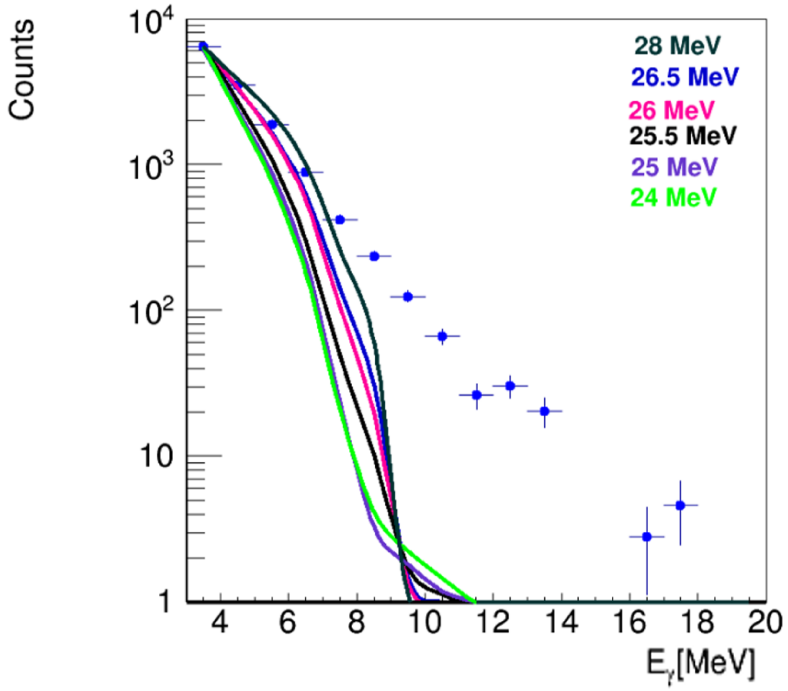

FIGURE 5.7: The curves represent CASCADE calculations obtained at several excitation energies up to 28 MeV. The blue dots represent the γ-rays energy spectrum in coincidence with Ni fragments.

way is the one plotted in Fig. 5.3 (a). These calculations have been folded with the detection response, the folding procedure is described in details in the section 5.1.3.

Such calculations are able to reproduce the low energy region of the spectra, confirming that this region is mainly due to the statistical decay of ^{68}Ni. Indeed, at this excitation energy the probability that the ^{68}Ni emits a high energy γ-ray, due to the statistical decay, is very low. For this reason, it is of fundamental importance to introduce resonances in the CASCADE calculations to reproduce the high energy region.

For this purpose we performed CASCADE calculations inserting resonances contributions based on the semiclassical calculations reported in the Chapter 3. Such calculations show that there are three states that can contribute in this high energy region: the Pygmy Dipole Resonance, the Giant Dipole Resonance and the Giant Quadrupole Resonance. For this reason, we insert in CASCADE such resonances, as it was also discussed in the section 5.1 (Tab. 5.1) in which we report values corresponding to the better agreement with the experimental data.

It is also important to evaluate whether such resonances can influence the region around 10 MeV. For this reason we report in Fig. 5.8 four curves obtained with

CASCADE, without the folding procedure, at an excitation energy peaked at 26.5 MeV.
The red curve is the calculation where the better agreement with the experimental spectrum is observed. In this calculation we have taken into account the PDR, GDR and GQR contributions. The violet curve is the CASCADE calculation obtained considering just the PDR + GDR contributions. As can be observed the bump corresponding to the GQR in the red curve causes just a little enhancement with respect the violet curve. The black curve is a standard CASCADE calculation considering the statistical decay of the ^{68}Ni and the green one is a CASCADE calculation obtained inserting just the GQR considering an unphysical strength of 300 % EWSR.
We prefer to report calculations without the folding procedure to clearly show the bumps corresponding to resonances and their influence in the region of 10 MeV. As can be deduced, the experimental spectrum can be reproduced only if we take into account the PDR presence, the other resonances have very little influence in the 10 MeV region.
As discussed above, semiclassical calculations allow to evaluate the population probability but we do not have information about the probability to have a γ-rays decay from such states. In particular, semiclassical calculations predict the presence of GQR with a high probability but in the present experiment we performed coincidence measurements of γ-rays, thus the calculations should be combined with the probability to emit a γ-ray. Moreover, we have also to consider that the resolution of the used experimental device in the higher energy region is very low, and in any case it is difficult to obtain information about the GQR and GDR population.

The inclusive statistical CASCADE calculations can reproduce the spectrum of Fig. 5.3, but it is not possible to compare such calculations with the spectrum in coincidence with the ^{68}Ni fragment as shown in Fig. 5.4 (a). However, the low energy region is in any case mainly due to the statistical decay of the ^{68}Ni as can be inferred also from Fig. 5.9. It is indeed possible to evaluate the cross section also considering the difference of the experimental spectrum (blue dots) with the CASCADE calculation. However, having the possibility to use also the experimental spectrum in coincidence with the ^{66,67}Ni isotopes, we prefer to use this channel in order to subtract also some events in the high energy region that can not be reproduced by calculations. Because the ^{66,67}Ni are neutron rich nuclei some events due to the PDR decay can be present also in this energy region; therefore,

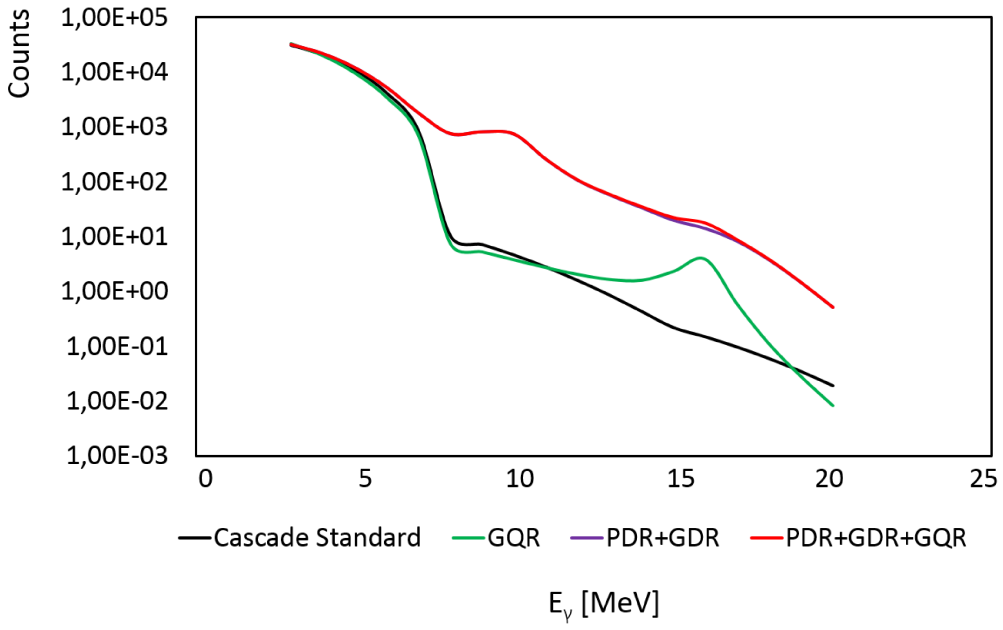

FIGURE 5.8: CASCADE calculations obtained with a standard CASCADE calculation (black curve), including the GQR contribution (green curve), including the PDR+GDR contributions (violet curve) and including the PDR+GDR+GQR contributions (red curve).

as mentioned above, the cross section represents just a lower limit.

5.1.3 GEANT4 simulations

The CASCADE calculations were folded with the detection response of our experimental set-up. The folding procedure takes into account of the detection response obtained with GEANT4 simulations, the solid angle covered by each ring and the experimental efficiency including just the functioning detectors.
The simulations have been performed using GEANT4 and root fair program [127, 128], in which the whole geometry of the CHIMERA array is taken into account, see Fig. 5.10
The GEANT4 simulations allow also to evaluate the average detection efficiency at 10 MeV, used to extract the cross section for the Pygmy decay. In Fig. 5.11 we report, as an example, the energy simulations at different angles $\theta \approx 30^\circ$, $\theta \approx 70^\circ$, $\theta \approx 94^\circ$, $\theta \approx 118^\circ$, considering the γ rays with energy of 10 MeV. Performing the integral of these spectra we are able to evaluate the detection efficiency at around 10 MeV. For CsI(Tl) detectors with the same thickness the efficiency depends also on the ratio between the surface of CsI(Tl) and the surface of the photodiode.

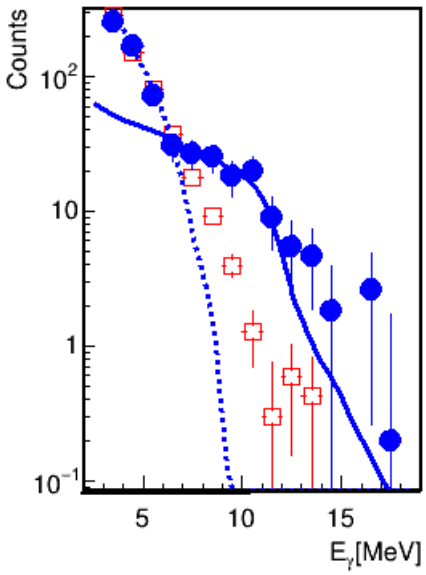

FIGURE 5.9: Energy γ spectrum obtained in coincidence with the ^{68}Ni beam and with the ^{68}Ni fragment. The blue dashed curve corresponds to the CASCADE calculation considering the statistical decay of the ^{68}Ni, while the blue full line corresponds to the first step CASCADE calculation.

In Fig. 5.12 we show the efficiency obtained with GEANT4 as a function of the thickness and θ_{LAB} of CsI(Tl). In this figure it is possible to observe that the detection efficiency is about 55 % for the scintillators having a thickness of 8 cm. However, these efficiencies have to be corrected for the solid angles covered by each ring and for the malfunctioning detectors. This correction lead to an average detection efficiency of 25 %.

Folding procedure

In order to obtain the folding of the CASCADE calculations, we performed 20 simulations, for each ring of the CHIMERA sphere, considering 2500 events of γ-rays. Each simulation corresponds to γ-rays with a definite energy (namely 1 MeV, 2 MeV, 3 MeV until to 20 MeV).
Such simulations allow also to evaluate the detection efficiency as a function of the γ-energy as shown in Fig. 5.13 for the ring 10, corresponding to a $\theta_{LAB} \approx 30°$. As it is possible to observe in this figure the detection efficiency decreases with the increase of the γ-energy.
The folding procedure can be expressed considering that *f(i)* is the curve that have

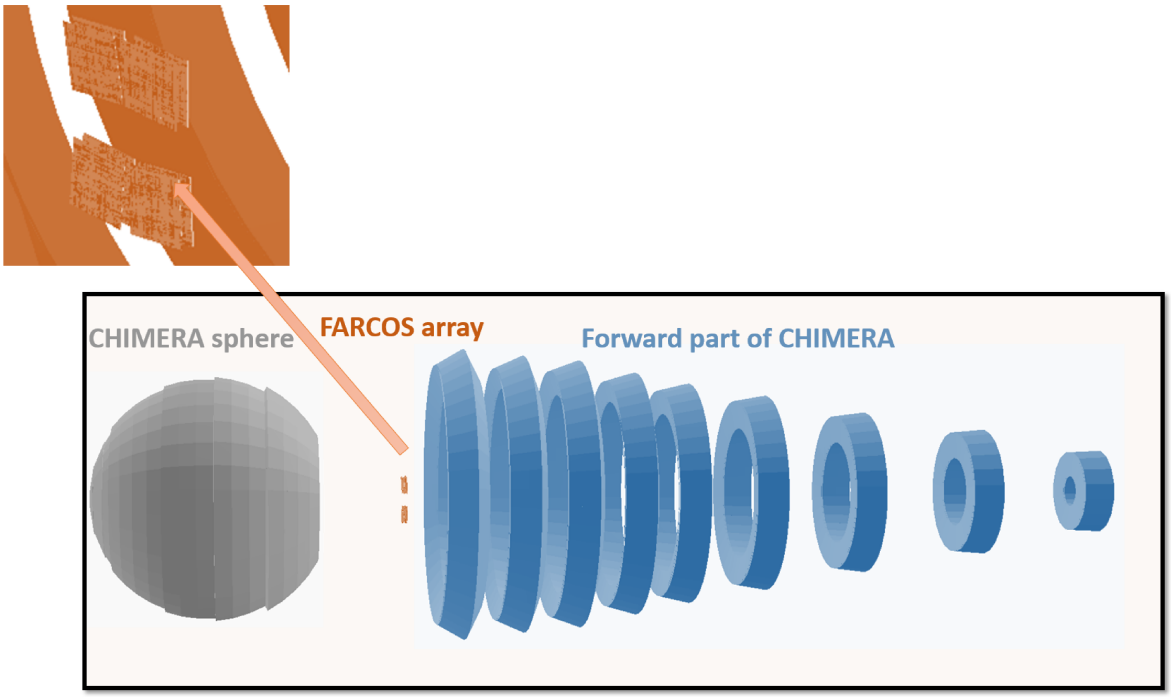

FIGURE 5.10: Geometry of the CHIMERA multidetector as used for the GEANT4 simulations. Also the Si detectors of the FARCOS array, placed after the CHIMERA multidetector sphere are visible. The Si detectors of the FARCOS array are better seen in the inset, where we plot a zoom of that region.

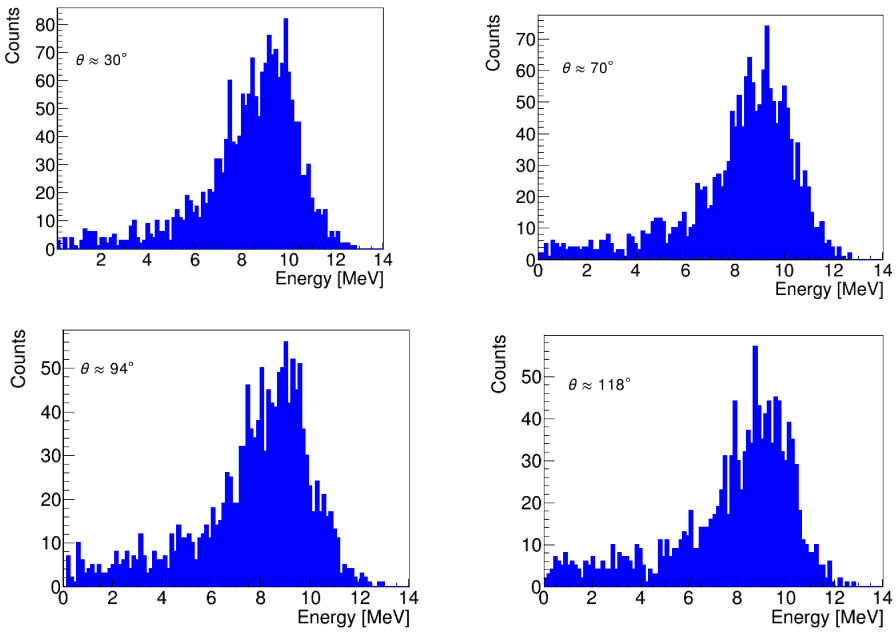

FIGURE 5.11: Energy γ-rays spectra simulated with GEANT4 in order to extract the detection efficiency around 10 MeV.

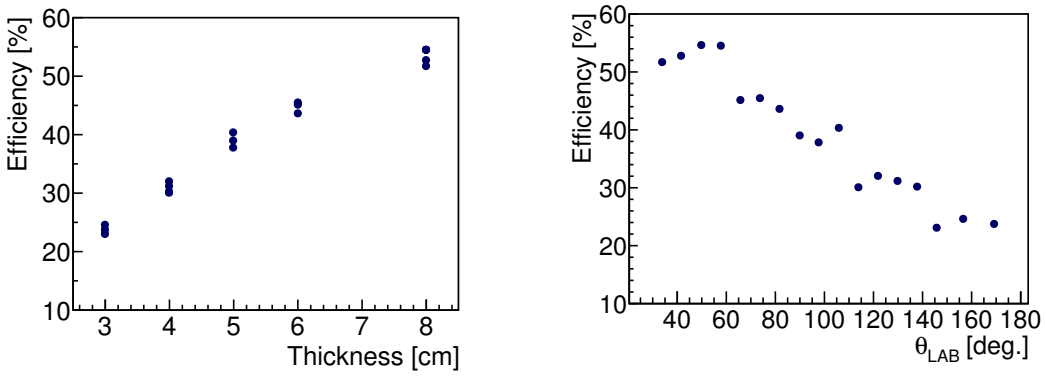

FIGURE 5.12: Detection efficiency obtained with GEANT4 simulations for γ-rays of about 10 MeV as a function of the thickness (left) and θ_{LAB} (right).

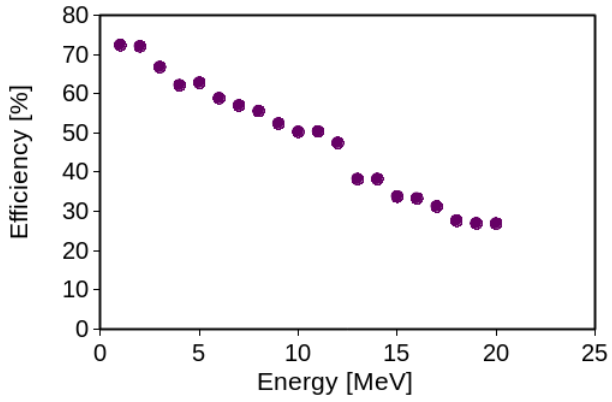

FIGURE 5.13: Detection efficiency obtained with GEANT4 as a function of the γ-energy for the ring 10 at $\theta_{LAB} \approx 30$ °.

to be folded with the detection response, and it is function of the energy *i*. In the present case *f(i)* is the CASCADE calculation and (i) represents a definite value of energy.
Having the detection response, for each energy value, the folded curve with the detection response will be given by the following formula:

$$f_{folded}(i) = \sum_{j=1}^{N} f(i) R_j(i) \tag{5.2}$$

in this formula N is the maximum of energy, in the present case 20 MeV. R is the detection efficiency as a function of the energy *(i)* and *(j)*.
To obtain the folding we performed for each simulation, and each ring, several integrals in order to extract the detection efficiency. In the case of 1 MeV simulation we performed the integral between 0.5 MeV and 1.5 MeV. In the case of the simulation up to 20 MeV we performed several integrals: in the region between 0.5 and 1.5 MeV, to evaluate the response function at 1 MeV generated from a γ-rays of 20 MeV, in the region between 1.5 and 2.5 MeV to evaluate the response function at 2 MeV generated from a γ-rays of 20 MeV, and so on until the integral around 20 MeV.
In Fig. 5.14 we show, as an example, the simulated spectrum at an energy of about 10 MeV for $\theta \approx 30\,^{\circ}$. The several colored regions correspond to the region in which we performed the integral to evaluate the 10 MeV detector response at 1 MeV, 2 MeV up to about 12 MeV.
Following this procedure, we obtained the CASCADE calculation folded with the detection efficiency. Moreover, to compare the CASCADE calculation with the experimental spectra, we have taken into account also of the solid angle coverage, for each ring, and of the malfunctioning detectors. Each f_{folded} obtained was indeed corrected for the corresponding values.

5.1.4 Comparison with other experiments

In Fig. 5.15 we report the fits on the Pygmy bump, obtained in two different ways: the first one considering the difference between the ^{68}Ni channel and the ^{66,67}Ni channel, the second one considering the ratio between these two channels. In both cases we obtained a centroid around 10 MeV and a width of $\approx$ 2 MeV. Being sure of the E1 character of the resonance, we can compare the measured γ-ray spectrum to the one obtained using an almost pure isovector probe, like in the relativistic

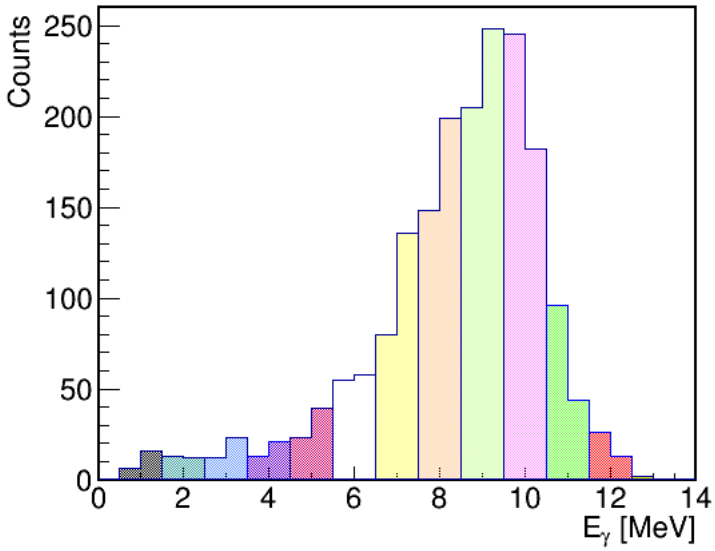

FIGURE 5.14: γ-rays energy spectrum obtained with GEANT4 at $\theta_{LAB} \approx 30°$. Each colored region corresponds to the region in which we performed the integral to obtain the folding of CASCADE calculations.

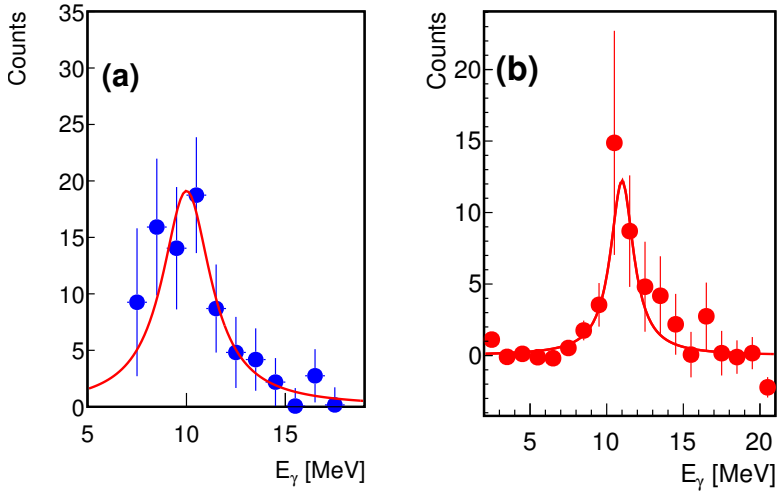

FIGURE 5.15: Fits on the Pygmy Dipole Resonance bump obtained with the subtraction (a) and the ratio (b) between the ^{68}Ni channel and the ^{66,67}Ni.

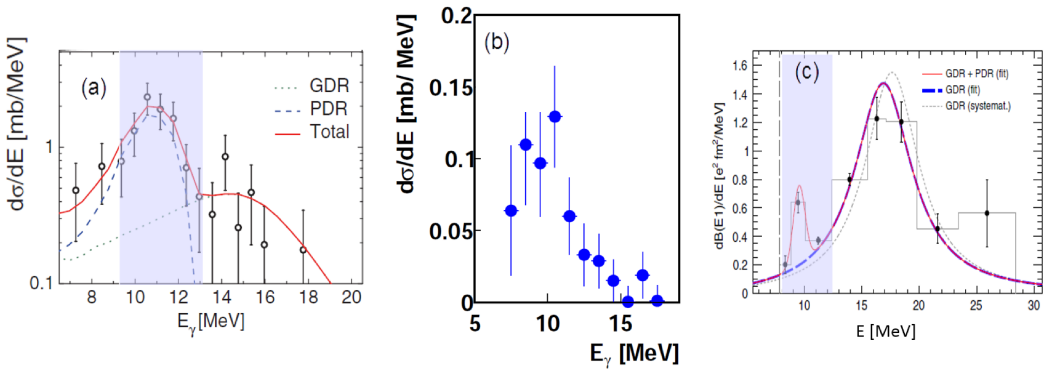

FIGURE 5.16: (a) Results obtained in ref. [55], (b) results obtained in our experiment, (c) results obtained in ref. [44].

Coulomb excitation of refs. [44, 55].

In Fig. 5.16 we show side by side the results obtained in our experiment (b) and the ones obtained in refs. [44, 55]. Comparing our results with the results obtained in ref. [55] we observe almost an order of magnitude difference between the two cross sections, which is probably caused by the different reactions regimes. Furthermore, in the experiment of ref. [55] the maximum of the energy distribution is located at around 11 MeV, while in our case it is peaked at around 10 MeV, more in agreement with the result obtained in ref. [44] where the peak for the PDR is at about 9.5 MeV.

Due to the response function of our CsI(Tl) detectors, the peak observed at 10 MeV can be generated also by γ-rays with energy of approximately 10.5 MeV. Moreover, the different slope of statistical γ-rays spectra underlying the resonance and propagation errors, in the calibration procedure, can account for the residual difference on the observed energy strength of the resonance, so these differences in energy of about 1 MeV or 0.5 MeV can be attributed to our detection efficiency and resolution.

Therefore, within the small statistics and the relatively scarce energy resolution of the present measurement and previous experiments [44, 55], this comparison seems to indicate that the outcome of the excitation process due to the two isoscalar and isovector probes is similar along the PDR energy region. Therefore, the isospin splitting seems not to be observed at the energy above the neutron emission threshold.

The position of the observed peak is also close to the predicted values reported in ref. [25, 129] of 9–10 MeV and in ref. [31], in which the result of an extended

relativistic calculation including coupling to more complicated states shows a centroid at 10.3 MeV.
Regarding the obtained strength, the value of 9 % $\pm$ 2 % is quite in agreement with the value obtained in ref. [55], considering the standard value of level density and also with the strength predicted by theoretical calculations [31]. However, in order to extract precise information about the strength one should perform DWBA calculations in an accurate way.

In summary we have observed, for the first time, the γ-ray decay of the Pygmy Dipole Resonance populated by an isoscalar probe in the ^{68}Ni. The measured γ-ray angular distribution shows the E1 character of the resonance. The measured cross section of the process amounts at 0.32 mb with 18 % of statistical error. We have shown that ^{12}C is a good probe for the isoscalar excitation. Moreover, the target contribution to the γ-ray energy spectrum in the region around 10 MeV is negligible. We have also shown that the E1 states at the low lying energy region around 10 MeV can be excited by both isoscalar and isovector probes, which is in agreement with the theoretical findings [4] about the mixed character of these dipole states. From the comparison with previous experiments performed with isovector probes it seems that the so-called isospin splitting it is not present for the low lying dipole states found at excitation energies above the neutron emission threshold. However, due to the limits of the relative small statistics and relative scarce energy resolution of the present measurement and previous experiments [44, 55], it is not possible to draw definite conclusions. Moreover, the role of multistep contributions to the population of the PDR, which is not present in the (α,α' γ) experiments in stable nuclei, may modify the shape of the energy distribution. The multistep contribution has been taken into account in ref. [15], for Coulomb relativistic excitation of Tin isotopes, where this effect has been estimated for the ^{132}Sn to be of the order of 10 %.
In order to further improve this observation, we are planning a new experiment to excite the Pygmy Dipole Resonance with both isoscalar and isovector probes. Such experiment will be performed during the 2019 at INFN-LNS. With the new oven the problem with the Zn source will be overcome and moreover we will use some improvements in the used experimental set up. First of all, we will use the GET electronics [130] that will allow to improve the quality of CsI(Tl) signals. This will provide also a better trigger realization, allowing to a more efficient removal of spurious coincidences. Moreover, we will use the new FARCOS configuration, consisting up to 8 telescopes with the possibility to have a better coverage of the

solid angle.

5.2 Neutron decay channel of the Pygmy Dipole Resonance: method and preliminary results

In this section we introduce the method and the preliminary results about the neutron decay channel of the Pygmy Dipole Resonance.
The study of the neutron decay channel allows to calculate the total cross section and to extract information about the parameters connected to the EoS and to the neutron skin, following the methods used in the section 1.3.
In order to extract information about the neutron decay we have to use an indirect method, as described in the section 4.1.8, in which we described two possible methods to detect neutrons.
We chose to start such data analysis using the second method, namely we considered just the telescopes of CHIMERA covered by the FARCOS array.
The study of the neutron decay is in any case very difficult, because we do not have the information on the neutrons energy and this means that the observed charged particles could be due to neutrons produced by several reaction channels. However, the energy distribution can be obtained using appropriated simulations.
In order to study this channel, we performed the coincidences between charged particles, observed in the CsI(Tl) detectors of the CHIMERA array, with the ^{67}Ni fragments, detected with the FARCOS array, and the ^{68}Ni beam, detected with the tagging system.
For this reason, the first step of such data analysis was to consider the first rings of the CHIMERA array to select just the telescopes covered by FARCOS. In Fig. 5.17 it is evident the difference between the fast-slow plot of the CsI(Tl) not covered by FARCOS (a) and the fast-slow plot of CsI(Tl) covered by FARCOS (b). In this way we are able to select the telescopes covered by FARCOS, and for each of such telescopes we performed graphical cuts in order to select the charged particles and remove also the γ-region, as shown in Fig. 5.18.
Having the cuts for all the telescopes covered by the FARCOS array we proceeded performing the coincidences with the ^{68}Ni beam and the ^{67}Ni detected using the FARCOS array. As mentioned we do not have the possibility to calculate the energy, in order to extract information about the neutron decay of the PDR we calculated the relative θ angle between the ^{67}Ni ions and the charged particle region observed in the CHIMERA CsI(Tl) telescopes. In Fig. 5.19 we report the obtained

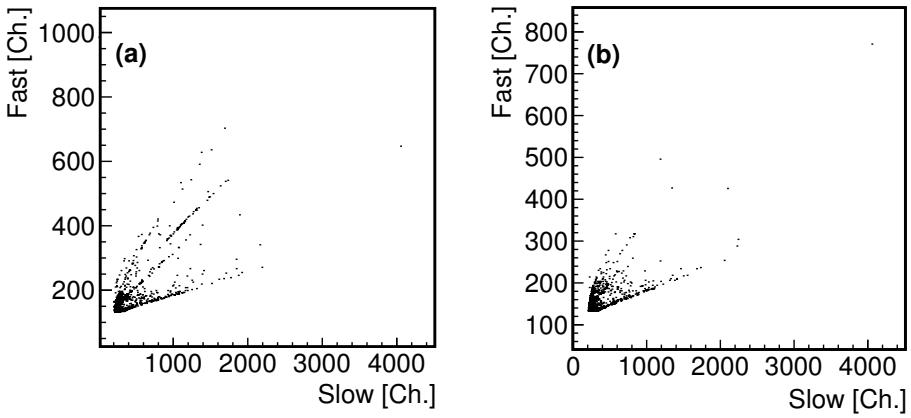

FIGURE 5.17: In the figure two fast-slow plots are shown, for a telescope not covered (a) by the FARCOS array and for a telescope covered (b) by the FARCOS array.

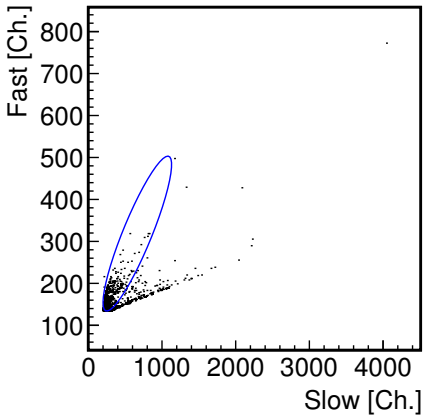

FIGURE 5.18: Fast-slow for a telescope of the CHIMERA array covered by FARCOS. In the figure also the charged particles region (blue ellipse), produced by neutrons interaction, is shown.

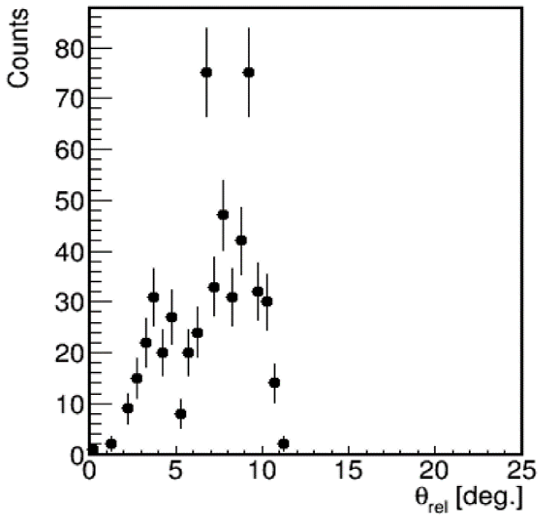

FIGURE 5.19: θ relative angle obtained performing the coincidence between the neutrons, detected with the CHIMERA array, and ^{67}Ni detected with FARCOS.

relative angle. We are performing also simulations in order to understand whether the angular distribution of θ relative observed is compatible with an emission of neutrons by the decay channel of the PDR. We are performing such simulations using the Phase Space class of root [131]. In Fig. 5.20 we report a preliminary result obtained with a simulation performed with Phase Space, such simulation is still in progress and we can not provide any conclusion.

5.3 Outlook

5.3.1 FraISe: the new INFN-LNS facility for in-flight RIBs production

In the forthcoming years, the Superconducting Cyclotron of the INFN-LNS is going to be improved [66, 132]. In particular, one of the main novelties will be the upgrading of the extraction system, based on electrostatic deflector, with a new extraction system based on stripping. The extraction by stripping is based on the change of the magnetic rigidity of an accelerated ion, when its charge state is increased crossing a thin carbon foil. This method will be highly efficient for light ions; in fact ions with mass number A < 20 and energy higher than 15A MeV are fully stripped with probability > 99 % when crossing a stripper foil [66]. This new extraction method will be very efficient also for nuclei with mass up to A $\approx$ 40.

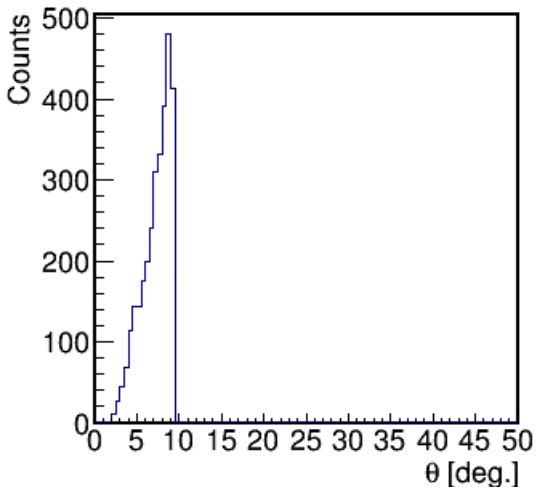

FIGURE 5.20: θ relative angle simulated with Phase Space [131].

This upgrade project opens new perspectives also for the production of fragmentation beams. The expected high power for primary beams indeed can be used to produce intense RIBs, allowing to obtain good intensities also for ions very far from the stability valley. For this purpose a new fragment separator, FraISe (**Fra**gment **I**n-flight **SE**parator), is designed [66]. The main idea is to maintain the possibility to deliver the beam in different experimental points, for this reason the new fragment separator will be placed in the area in which are currently located the 20° and 40° LNS experimental halls. This area is shown as a circle in Fig. 5.21. The first part of the fragment separator will be composed of two 70 ° and 40 ° dipoles (D1 and D2, respectively in Fig. 5.22) and 1 triplet and 1 doublet (Q1-Q3 and Q4-Q5, respectively, in Fig. 5.22). The second part of the fragment separator will be a mirror-copy of the first part, as it is shown in Fig. 5.22. This design ensures a full achromaticity of the fragment separator [66]. However, it will be possible to use also a mechanical control of the beam profile by means of a mechanical slits system, and to insert, just after the slits system, a wedge (degrader) to perform a better rejection of unwanted ions.
Indeed, as discussed in Chapter 3, a magnetic analysis can not separate ions having the same A/Z ratio. A solution is then to use a degrader, namely a piece of matter inserted at the dispersive focal plane between the two sections of the fragment separator. In such way, different isotopes, depending mainly on their atomic number, will have different velocities after passing through the degrader. This

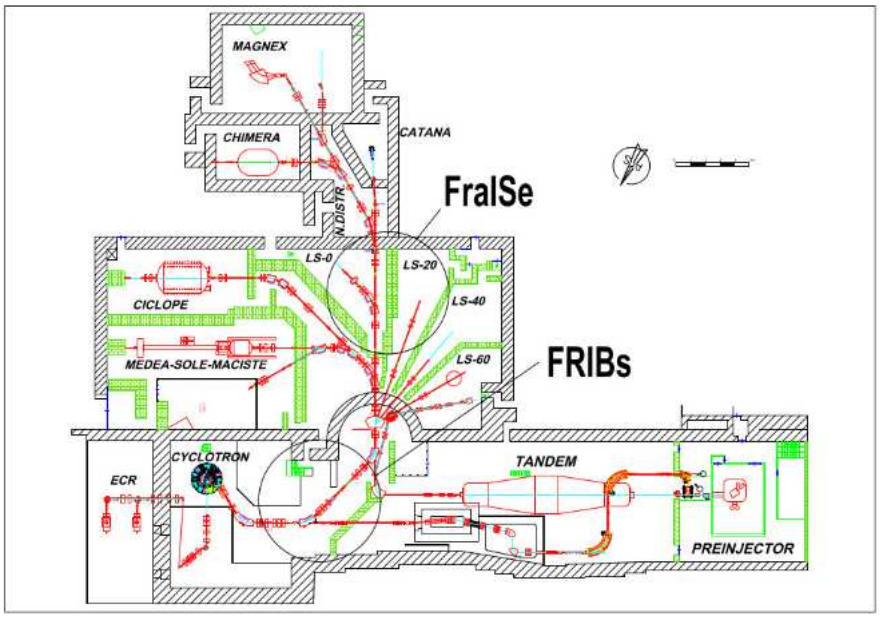

FIGURE 5.21: Schematic view of the INFN-LNS beam lines and halls. The position of the actual fragment separator and of the new one, FraISe, are indicated by circles [66].

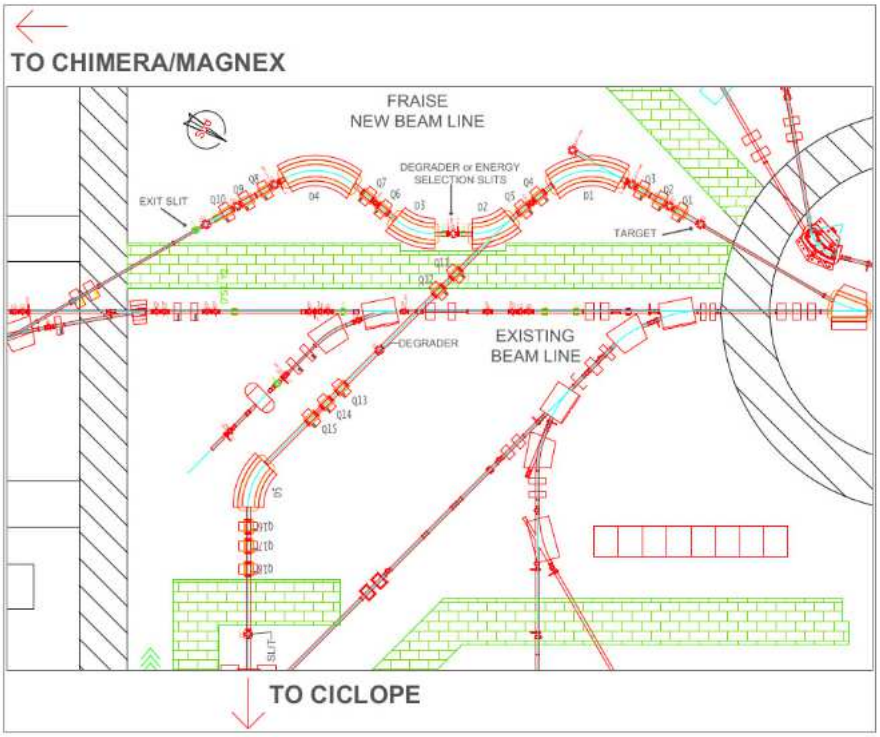

FIGURE 5.22: Schematic view of FraISe [66].

main product	primary beam/energy (AMeV)	thickness Be target (μm)	wedge thickness (μm)	primary intensity (kW)	expected yield (kHz)	purity (%)	energy after tagging (AMeV)
^{14}Be	$^{18}O/55$	1500	0	2	2.6	2	46
^{14}Be	$^{18}O/55$	1500	1000	2	2.2	70	43
^{13}N	$^{16}O/40$	700	600	2	1230	54	4
^{14}O	$^{16}O/40$	700	600	2	807	36	4
^{18}Ne	$^{20}Ne/60$	1000	0	2	16700	16	43
^{18}Ne	$^{20}Ne/60$	1000	1000	2	3120	47	24
^{17}F	$^{20}Ne/60$	1000	1000	2	3300	49	23
^{34}Si	$^{36}S/40$	500	500	2	980	81	11
^{38}S	$^{40}Ar/40$	500	300	2	1840	66	17
^{34}Ar	$^{36}Ar/50$	250	0	2	2800	4	41
^{34}Ar	$^{36}Ar/50$	250	500	2	426	12	4
^{68}Ni	$^{70}Zn/50$	250	200	1	490	50	18

FIGURE 5.23: Expected yield with the new fragment separator FraISe [66].

change in velocity causes that the isotopes with the same A/Z ratio will be separated in the second dispersive stage. This method has been described in ref. [133]. Because the degrader slows all particles down, the Bρ setting of the magnetic elements following the degrader have to be accordingly adjusted. In particular the optical settings of the two dispersive sections of the fragment separator are not mirror of each other anymore, and the magnetic rigidity of the second dipole has to be decreased. In other cases, it can be useful that the shape of the wedge preserves another parameter of the beam such as, for instance, its velocity. In that case, the wedge is shaped in order to narrow the energy spread of the selected particles.
Moreover, also an improvement of the diagnostic systems [134] will be needed to measure the intensity and the profile of the RIBs along the lines, in order to perform an optimal transport.

With an efficient rejection of the unwanted ions from the fragmentation beam, together with the use of the degrader and the slits system, the RIBs will have a higher purity. In many cases, it will be possible to get higher intensities for the wanted isotope, with respect to the FRIBs, still keeping the total rate low enough in order to use the present tagging system. Expected intensities, calculated by using the LISE simulation code are listed in Tab. 5.23.

Using this upgrade the investigation of Pygmy Dipole Resonance at INFN-LNS will be extended also to other systems, allowing to probe several mass regions with a high intensity.

Conclusion

In this thesis we discussed the results of an experiment carried out at the INFN-LNS in Catania, aimed to study for the first time the Pygmy Dipole Resonance, above the neutron emission threshold in the unstable nucleus ^{68}Ni, using a natural carbon target.
In order to produce the exotic beam we used a primary beam of ^{70}Zn, accelerated at 40A MeV by the Superconducting Cyclotron. The ^{70}Zn beam impinged on a 250 μm thick ^{9}Be target to produce, with a projectile fragmentation reaction, the ^{68}Ni beam, delivered via the FRIBs@LNS fragment separator.
Within semiclassical calculations it has been shown that the ^{68}Ni + ^{12}C reaction at 28A MeV allows to populate the PDR mainly through the nuclear interaction, but although the Coulomb contribution is very low, about the 30 % of the total inelastic cross section is due to the interference between nuclear and Coulomb contributions. Such calculations showed also as other multipolarities can be populated at this energy.
The main goal of such experiment was to investigate the γ-rays decay channel of the PDR. In order to detect the γ-rays we used the CsI(Tl) scintillators of the CHIMERA sphere and in particular we used the fast-slow method to identify such γ-rays. A considerable part of the data analysis was dedicated to the calibration of the CsI(Tl) scintillators, performed using a proton beam, accelerated by the TANDEM accelerator of the INFN-LNS at 24 MeV, and several targets of Au, CH_2 and ^{12}C. The p+ ^{12}C reaction was very useful to show that the probability to have γ-rays produced by the decay of the ^{12}C in the energy region of the PDR, namely at about 10 MeV, is negligible. Furthermore, it allowed to extract the angular distribution for the 2^+ state of the ^{12}C, confirming also the capacity of the CHIMERA multidetector to realize nuclear structure experiment.
The γ-decay channel was investigated using triple coincidences, namely detecting the energy γ-ray spectrum in coincidence with the ^{68}Ni^{28+} beam, detected with the tagging system, and the Ni fragments, detected using the FARCOS array. The high quality of the DSSSD detectors of the FARCOS array, together with the cleaning effect of the fragment separator, provided the full isotopic identification of ^{68}Ni

and also of other ions produced in the reaction.
We performed also CASCADE calculations in order to study the statistical decay of the ^{68}Ni at an excitation energy of about 26.5 MeV. By means of the CASCADE calculations we were able to understand that only the low energy region of the γ-rays energy spectrum can be fitted with the statistical decay of the ^{68}Ni, while in order to reproduce the experimental spectrum also in the high energy region we have to consider the contribution of resonance states. This procedure made clear that the presence of the GQR and GDR is negligible and the experimental spectrum could be fitted only inserting in CASCADE calculations the presence of the Pygmy Dipole Resonance, with a centroid around 10 MeV, a width of 2 MeV, and a strength of 9 ± 2 %. Such CASCADE calculations were folded with the detection response of used experimental set up, therefore a part of the data analysis was dedicated to perform GEANT4 simulations in order to extract such detection efficiency.
Taking advantage of the triple coincidences we used them in order to increase the visibility of the Pygmy resonance, indeed the γ-rays energy spectrum detected in coincidence with the ^{68}Ni beam and with the ^{68}Ni fragment clearly showed the bump at around 10 MeV. We compared the γ-rays energy spectrum in coincidence with the ^{68}Ni, with the one measured in coincidence with ^{66,67}Ni nuclei. Using the difference of the two spectra we evaluated the cross section of the PDR. This method allowed to give a lower limit to the PDR cross section, because some small PDR contribution could be present also in the ^{66,67}Ni coincidence spectrum. It was also of fundamental importance to verify the dipole character of the observed bump at 10 MeV, for such purpose we evaluated the γ-rays angular distribution that showed the E1 character of the transition with a maximum at 90 $^{\circ}$.
Finally, we performed some comparisons with other two experiments in which the PDR in the ^{68}Ni was studied using an isovector probe. This comparison did not show important differences in the centroid of the peaks. This indicates that the isospin splitting seems not to be observed at the energy above the neutron emission threshold. However, due to the limits of the relative small statistics and relative scarce energy resolution of the present measurement and previous experiments, it is not possible to draw definite conclusions. Moreover, the role of multistep contributions to the population of the PDR, which is not present in the (α,α' γ) experiments in stable nuclei, may modify the shape of the energy distribution.

We presented also the preliminary results in order to extract information about the neutron decay channel of the PDR. Such results are still in progress and we can

not provide any conclusive information about this data analysis.
With the aim to deeply understand the nature of the PDR we proposed another experiment, that will be realized during the 2019, in order to excite the PDR in the ^{68}Ni using also an isovector probe. Moreover, we will use some improvements in the used experimental set up to better realize such experiment. First of all, we will use the GET electronics, that will allow to improve the quality of CsI(Tl) signals. This will provide also a better trigger realization, allowing to a more efficient removal of spurious coincidences. Moreover, we will use the new FARCOS configuration, consisting up to 8 telescopes with new large dynamic ASIC preamplifier telescopes. This means that we will have a better coverage of the solid angle and the possibility to cover also the region at small angles, detecting the elastic channel. This information will be of fundamental importance to perform DWBA calculations and to extract the strength of the PDR in an accurate way.
In the future the investigation of Pygmy Dipole Resonances at INFN-LNS will be extended to other systems thanks to the upgrading in intensity of the cyclotron and the construction of the new fragment separator FraISe presented in the section 5.3.1.

Appendix A

Semiclassical calculations

The calculations presented in Chapter 3 have been done according to the semiclassical coupled channel model described in refs. [4, 15, 16]. In such semiclassical model one can assume that in the heavy ions collisions the motion of the center of mass of the two interacting nuclei is described using the classical mechanics [4, 15, 16, 135]. In the Coulomb scattering case this assumption is true when the Sommerfeld parameter η is bigger than 1. The Sommerfeld parameter is defined as follows:

$$\eta = \frac{Z_A Z_B e^2}{h\nu} \tag{A.1}$$

in this equation ν is the asymptotic relative velocity, Z_A, Z_B are the atomic numbers of the two interacting nuclei, e is the charge of the electron and h is the Planck constant.

The Sommerfeld parameter can be considered as the ratio between the half of the distance of closest approach $a=\frac{Z_A Z_B e^2}{m_0 \nu^2}$ and the wave length of De Broglie.

In case of nuclear plus Coulomb interactions the approach is more complex, but the semiclassical assumption is valid when the De Broglie wave length associate with the incident particle is smaller with respect to a characteristic distance of the process, like the distance of closest approach.

In the case of heavy ions collisions this assumption is true at incident energies $E \geq E_c$ (in which E_c is the energy of the Coulomb barrier).

Therefore, in such semiclassical approach the two colliding nuclei move according to a classical trajectory determined by the Coulomb plus nuclear fields, while the inelastic excitations are described according to quantum mechanics.

The Hamiltonian H of the system can be written as:

$$H = H_B + H_A \tag{A.2}$$

Where H_A and H_B are the Hamiltonian for the nuclei A and B.

The Hamiltonian H for the nucleus whose excitation one wants to describe, for instance the nucleus B, is formed by two parts: one describing the internal structure of the nucleus H_B^0 and the other one is given by the external field $W_B(t)$ responsible for the excitation of one partner of the reaction through the mean field of the other one:

$$H_B = H_B^0 + W_B(t) \tag{A.3}$$

In the case in which the trajectory is not influenced by the excitation of two nuclei the wave function can be written as follows:

$$|\psi(t)\rangle = |\psi_B(t)\rangle|\psi_A(t)\rangle \tag{A.4}$$

At this point one can resolve the Schrödinger equation for the nucleus A:

$$ih\frac{\partial|\psi_A(t)\rangle}{\partial t} = H_A|\psi_A(t)\rangle \tag{A.5}$$

with the condition $|\psi_A(-\infty)\rangle = |\psi_A^0\rangle$.

The wave function for the nucleus A can be written as:

$$|\psi_A(t)\rangle = \sum_\alpha a_\alpha(t)e^{-\frac{i}{h}E_\alpha t}|\phi_\alpha\rangle \tag{A.6}$$

where ϕ_α is an eigenstate of the Hamiltonian H_0^A.

The time evolution of the eigenstates of the internal Hamiltonian is described by the Schrödinger equation which can be cast into a set of coupled first order differential equations for the time-dependent probability amplitude of the channels wave functions:

$$\dot{a}_\alpha(t) = -\frac{i}{h}\sum_{\alpha'} e^{\frac{i}{h}(E_\alpha - E_{\alpha'})t}\langle\phi_\alpha|W(t)|\phi_{\alpha'}\rangle a_{\alpha'}(t) \tag{A.7}$$

The system of semiclassical coupled channel equations obtained in this way has to be solved for each impact parameter b. The solution of this system of coupled equations provides the excitation probability for each of the states we take into account, as a function of the impact parameter .

The probability P to excite the state α is given by:

$$P_\alpha(b) = |a_\alpha(b, +\infty)|^2 \tag{A.8}$$

the corresponding total cross section is then given by:

$$\sigma_\alpha = 2\pi \int_0^\infty P_\alpha(b) T(b) b db \tag{A.9}$$

where *T(b)* is the transmission coefficient, related to the imaginary part of the optical potential.
Then, the excitation cross section for each of these states is obtained by an integration of the excitation probabilities of the states over the interval of the impact parameters contributing to the reaction.
The states considered in the excitation process are usually determined by a mean field model like the HF plus RPA . In the case there are many states with significant EWSR belonging to the same energy region, one bunches them together by taking as energy their average energy with the condition that the EWSR must be preserved.

Bibliography

[1] D. Savran, T. Aumann, and A. Zilges, "Experimental studies of the Pygmy Dipole Resonance", in: *Progress in Particle and Nuclear Physics*, vol. 70, (2013), pp. 210 –245, ISSN: 0146-6410, DOI: https://doi.org/10.1016/j.ppnp.2013.02.003, URL: http://www.sciencedirect.com/science/article/pii/S0146641013000057.

[2] N. Paar et al., "Exotic modes of excitation in atomic nuclei far from stability", in: *Reports on Progress in Physics*, vol. 70, no. 5, (2007), p. 691, URL: http://stacks.iop.org/0034-4885/70/i=5/a=R02.

[3] A. Bracco, F. C. L. Crespi, and E. G. Lanza, "Gamma decay of pygmy states from inelastic scattering of ions", in: *The European Physical Journal A*, vol. 51, no. 8, (2015), p. 99, ISSN: 1434-601X, DOI: 10.1140/epja/i2015-15099-6, URL: https://doi.org/10.1140/epja/i2015-15099-6.

[4] E. G. Lanza, A. Vitturi, and M. V. Andrés, "Microscopic nuclear form factors for the pygmy dipole resonance", in: *Phys. Rev. C*, vol. 91, iss. 5 (2015), p. 054607, DOI: 10.1103/PhysRevC.91.054607, URL: https://link.aps.org/doi/10.1103/PhysRevC.91.054607.

[5] G. A. Bartholomew, "Neutron capture gamma rays", in: *Annu. Rev. Nucl. Sci.* Vol. 11, (1961), p. 259.

[6] J. S. Brzosko et al., "Effect of the pigmy resonance on the calculations of the neutron capture cross section", in: *Canad. Journ. of Phys.* Vol. 47, (1969), p. 2849.

[7] R. Mohan, M. Danos, and L. C. Biedenharn, "Three-Fluid Hydrodynamical Model of Nuclei", in: *Phys. Rev. C*, vol. 3, iss. 5 (1971), pp. 1740–1749, DOI: 10.1103/PhysRevC.3.1740, URL: https://link.aps.org/doi/10.1103/PhysRevC.3.1740.

[8] K. Govaert et al., "Dipole excitations to bound states in ^{116}Sn and ^{124}Sn", in: *Phys. Rev. C*, vol. 57, iss. 5 (1998), pp. 2229–2249, DOI: 10.1103/PhysRevC.57.2229, URL: https://link.aps.org/doi/10.1103/PhysRevC.57.2229.

[9] I. Tanihata et al., "Measurements of interaction cross sections and radii of He isotopes", in: *Physics Letters B*, vol. 160, no. 6, (1985), pp. 380 –384, ISSN: 0370-2693, DOI: https://doi.org/10.1016/0370-2693(85)90005-X, URL: http://www.sciencedirect.com/science/article/pii/037026938590005X.

[10] I. Tanihata et al., "Measurements of Interaction Cross Sections and Nuclear Radii in the Light *p*-Shell Region", in: *Phys. Rev. Lett.* Vol. 55, iss. 24 (1985), pp. 2676–2679, DOI: 10.1103/PhysRevLett.55.2676, URL: https://link.aps.org/doi/10.1103/PhysRevLett.55.2676.

[11] P. G. Hansen and B. Jonson, "The Neutron Halo of Extremely Neutron-Rich Nuclei", in: *EPL (Europhysics Letters)*, vol. 4, no. 4, (1987), p. 409, URL: http://stacks.iop.org/0295-5075/4/i=4/a=005.

[12] A. Leistenschneider et al., "Photoneutron Cross Sections for Unstable Neutron-Rich Oxygen Isotopes", in: *Phys. Rev. Lett.* Vol. 86, iss. 24 (2001), pp. 5442–5445, DOI: 10.1103/PhysRevLett.86.5442, URL: https://link.aps.org/doi/10.1103/PhysRevLett.86.5442.

[13] E. Tryggestad et al., "Low-lying dipole strength in 20O", in: *Physics Letters B*, vol. 541, no. 1, (2002), pp. 52 –58, ISSN: 0370-2693, DOI: https://doi.org/10.1016/S0370-2693(02)02224-4, URL: http://www.sciencedirect.com/science/article/pii/S0370269302022244.

[14] F. Catara et al., "Effect of large neutron excess on the dipole response in the region of the giant dipole resonance", in: *Nuclear Physics A*, vol. 624, no. 3, (1997), pp. 449 –458, ISSN: 0375-9474, DOI: https://doi.org/10.1016/S0375-9474(97)00485-5, URL: http://www.sciencedirect.com/science/article/pii/S0375947497004855.

[15] E. G. Lanza et al., "Multiphonon excitations and pygmy resonances in tin isotopes", in: *Phys. Rev. C*, vol. 79, iss. 5 (2009), p. 054615, DOI: 10.1103/PhysRevC.79.054615, URL: https://link.aps.org/doi/10.1103/PhysRevC.79.054615.

[16] E. G. Lanza et al., "Excitations of pygmy dipole resonances in exotic and stable nuclei via Coulomb and nuclear fields", in: *Phys. Rev. C*, vol. 84, iss. 6 (2011), p. 064602, DOI: 10.1103/PhysRevC.84.064602, URL: https://link.aps.org/doi/10.1103/PhysRevC.84.064602.

[17] I. Hamamoto and H. Sagawa, "Low energy strength in low-multipole response function of nuclei near the neutron drip line", in: *Phys. Rev. C*, vol. 53, iss. 4 (1996), R1492–R1496, DOI: 10.1103/PhysRevC.53.R1492, URL: https://link.aps.org/doi/10.1103/PhysRevC.53.R1492.

[18] X. Roca-Maza et al., "Low-lying dipole response: Isospin character and collectivity in ^{68}Ni, ^{132}Sn, and ^{208}Pb", in: *Phys. Rev. C*, vol. 85, iss. 2 (2012), p. 024601, DOI: 10.1103/PhysRevC.85.024601, URL: https://link.aps.org/doi/10.1103/PhysRevC.85.024601.

[19] J. Terasaki and J. Engel, "Self-consistent description of multipole strength: Systematic calculations", in: *Phys. Rev. C*, vol. 74, iss. 4 (2006), p. 044301, DOI: 10.1103/PhysRevC.74.044301, URL: https://link.aps.org/doi/10.1103/PhysRevC.74.044301.

[20] Kenichi Yoshida and Nguyen Van Giai, "Deformed quasiparticle-random-phase approximation for neutron-rich nuclei using the Skyrme energy density functional", in: *Phys. Rev. C*, vol. 78, iss. 6 (2008), p. 064316, DOI: 10.1103/PhysRevC.78.064316, URL: https://link.aps.org/doi/10.1103/PhysRevC.78.064316.

[21] D. Gambacurta, M. Grasso, and F. Catara, "Low-lying dipole response in the stable ^{40,48}Ca nuclei with the second random-phase approximation", in: *Phys. Rev. C*, vol. 84, iss. 3 (2011), p. 034301, DOI: 10.1103/PhysRevC.84.034301, URL: https://link.aps.org/doi/10.1103/PhysRevC.84.034301.

[22] Mitsuru Tohyama and Takashi Nakatsukasa, "Fragmentation of electric dipole strength in $N = 82$ isotones", in: *Phys. Rev. C*, vol. 85, iss. 3 (2012), p. 031302, DOI: 10.1103/PhysRevC.85.031302, URL: https://link.aps.org/doi/10.1103/PhysRevC.85.031302.

[23] T. Hartmann et al., "Microscopic Nature of the Pygmy Dipole Resonance: The Stable Ca Isotopes", in: *Phys. Rev. Lett.* Vol. 93, iss. 19 (2004), p. 192501, DOI: 10.1103/PhysRevLett.93.192501, URL: https://link.aps.org/doi/10.1103/PhysRevLett.93.192501.

[24] N. Tsoneva and H. Lenske, "Pygmy dipole resonances in the tin region", in: *Phys. Rev. C*, vol. 77, iss. 2 (2008), p. 024321, DOI: 10.1103/PhysRevC.77.024321, URL: https://link.aps.org/doi/10.1103/PhysRevC.77.024321.

[25] D. Vretenar et al., "Collectivity of the low-lying dipole strength in relativistic random phase approximation", in: *Nuclear Physics A*, vol. 692, no. 3, (2001), pp. 496 –517, ISSN: 0375-9474, DOI: https://doi.org/10.1016/S0375-9474(01)00653-4, URL: http://www.sciencedirect.com/science/article/pii/S0375947401006534.

[26] J. Piekarewicz, "Pygmy dipole resonance as a constraint on the neutron skin of heavy nuclei", in: *Phys. Rev. C*, vol. 73, iss. 4 (2006), p. 044325, DOI: 10.1103/PhysRevC.73.044325, URL: https://link.aps.org/doi/10.1103/PhysRevC.73.044325.

[27] E. Litvinova, P. Ring, and D. Vretenar, "Relativistic RPA plus phonon-coupling analysis of pygmy dipole resonances", in: *Physics Letters B*, vol. 647, no. 2, (2007), pp. 111 –117, ISSN: 0370-2693, DOI: https://doi.org/10.1016/j.physletb.2007.01.056, URL: http://www.sciencedirect.com/science/article/pii/S0370269307001815.

[28] N. Paar et al., "Quasiparticle random phase approximation based on the relativistic Hartree-Bogoliubov model", in: *Phys. Rev. C*, vol. 67, iss. 3 (2003), p. 034312, DOI: 10.1103/PhysRevC.67.034312, URL: https://link.aps.org/doi/10.1103/PhysRevC.67.034312.

[29] N. Paar et al., "Isotopic dependence of the pygmy dipole resonance", in: *Physics Letters B*, vol. 606, no. 3, (2005), pp. 288 –294, ISSN: 0370-2693, DOI: https://doi.org/10.1016/j.physletb.2004.12.011, URL: http://www.sciencedirect.com/science/article/pii/S0370269304016673.

[30] A. Klimkiewicz et al., "Nuclear symmetry energy and neutron skins derived from pygmy dipole resonances", in: *Phys. Rev. C*, vol. 76, iss. 5 (2007), p. 051603, DOI: 10.1103/PhysRevC.76.051603, URL: https://link.aps.org/doi/10.1103/PhysRevC.76.051603.

[31] E. Litvinova, Peter Ring, and Victor Tselyaev, "Mode Coupling and the Pygmy Dipole Resonance in a Relativistic Two-Phonon Model", in: *Phys. Rev. Lett.* Vol. 105, iss. 2 (2010), p. 022502, DOI: 10.1103/PhysRevLett.105.022502, URL: https://link.aps.org/doi/10.1103/PhysRevLett.105.022502.

[32] N. Paar, D. Vretenar, and P. Ring, "Proton Electric Pygmy Dipole Resonance", in: *Phys. Rev. Lett.* Vol. 94, iss. 18 (2005), p. 182501, DOI: 10.1103/PhysRevLett.94.182501, URL: https://link.aps.org/doi/10.1103/PhysRevLett.94.182501.

[33] P. Ring and P. Schuck, in: *The Nuclear Many-Body Problem*, (1980).

[34] M. N. Harakeh and A. E. L. Dieperink, "Isoscalar dipole resonance: Form factor and energy weighted sum rule", in: *Phys. Rev. C*, vol. 23, iss. 5 (1981), pp. 2329–2334, DOI: 10.1103/PhysRevC.23.2329, URL: https://link.aps.org/doi/10.1103/PhysRevC.23.2329.

[35] G.R. Satchler and W.G. Love, "Folding model potentials from realistic interactions for heavy-ion scattering", in: *Physics Reports*, vol. 55, no. 3, (1979), pp. 183 –254, ISSN: 0370-1573, DOI: https://doi.org/10.1016/0370-1573(79)90081-4, URL: http://www.sciencedirect.com/science/article/pii/0370157379900814.

[36] G. R. Satchler, in: *Direct Nuclear Reactions (Oxford University Press, Oxford)*, (1983).

[37] E. Litvinova et al., "Relativistic quasiparticle time blocking approximation. II. Pygmy dipole resonance in neutron-rich nuclei", in: *Phys. Rev. C*, vol. 79, iss. 5 (2009), p. 054312, DOI: 10.1103/PhysRevC.79.054312, URL: https://link.aps.org/doi/10.1103/PhysRevC.79.054312.

[38] J. Piekarewicz et al., "Electric dipole polarizability and the neutron skin", in: *Phys. Rev. C*, vol. 85, iss. 4 (2012), p. 041302, DOI: 10.1103/PhysRevC.85.041302, URL: https://link.aps.org/doi/10.1103/PhysRevC.85.041302.

[39] S. Goriely and E. Khan, "Large-scale QRPA calculation of E1-strength and its impact on the neutron capture cross section", in: *Nuclear Physics A*, vol. 706, no. 1, (2002), pp. 217 –232, ISSN: 0375-9474, DOI: https://doi.org/10.1016/S0375-9474(02)00860-6, URL: http://www.sciencedirect.com/science/article/pii/S0375947402008606.

[40] N. Tsoneva et al., "Pygmy resonances and radiative nucleon captures for stellar nucleosynthesis", in: *Phys. Rev. C*, vol. 91, iss. 4 (2015), p. 044318, DOI: 10.1103/PhysRevC.91.044318, URL: https://link.aps.org/doi/10.1103/PhysRevC.91.044318.

[41] E. Litvinova et al., "Low-lying dipole response in the relativistic quasiparticle time blocking approximation and its influence on neutron capture cross sections", in: *Nuclear Physics A*, vol. 823, no. 1, (2009), pp. 26 –37, ISSN: 0375-9474, DOI: https://doi.org/10.1016/j.nuclphysa.2009.03.009, URL: http://www.sciencedirect.com/science/article/pii/S0375947409001845.

[42] A. Carbone et al., "Constraints on the symmetry energy and neutron skins from pygmy resonances in ^{68}Ni and ^{132}Sn", in: *Phys. Rev. C*, vol. 81, iss. 4 (2010), p. 041301, DOI: 10.1103/PhysRevC.81.041301, URL: https://link.aps.org/doi/10.1103/PhysRevC.81.041301.

[43] P.G. Reinhard and W. Nazarewicz, "Information content of a new observable: The case of the nuclear neutron skin", in: *Phys. Rev. C*, vol. 81, iss. 5 (2010), p. 051303, DOI: 10.1103/PhysRevC.81.051303, URL: https://link.aps.org/doi/10.1103/PhysRevC.81.051303.

[44] D. M. Rossi et al., "Measurement of the Dipole Polarizability of the Unstable Neutron-Rich Nucleus ^{68}Ni", in: *Phys. Rev. Lett.* Vol. 111, iss. 24 (2013), p. 242503, DOI: 10.1103/PhysRevLett.111.242503, URL: https://link.aps.org/doi/10.1103/PhysRevLett.111.242503.

[45] J. Piekarewicz, "Pygmy resonances and neutron skins", in: *Phys. Rev. C*, vol. 83, iss. 3 (2011), p. 034319, DOI: 10.1103/PhysRevC.83.034319, URL: https://link.aps.org/doi/10.1103/PhysRevC.83.034319.

[46] S. Goriely, "Radiative neutron captures by neutron-rich nuclei and the r-process nucleosynthesis", in: *Physics Letters B*, vol. 436, no. 1, (1998), pp. 10–18, ISSN: 0370-2693, DOI: https://doi.org/10.1016/S0370-2693(98)00907-1, URL: http://www.sciencedirect.com/science/article/pii/S0370269398009071.

[47] D. Savran et al., "Fragmentation and systematics of the pygmy dipole resonance in the stable $N = 82$ isotones", in: *Phys. Rev. C*, vol. 84, iss. 2 (2011), p. 024326, DOI: 10.1103/PhysRevC.84.024326, URL: https://link.aps.org/doi/10.1103/PhysRevC.84.024326.

[48] R. Schwengner et al., "Dipole response of ^{88}Sr up to the neutron-separation energy", in: *Phys. Rev. C*, vol. 76, iss. 3 (2007), p. 034321, DOI: 10.1103/PhysRevC.76.034321, URL: https://link.aps.org/doi/10.1103/PhysRevC.76.034321.

[49] R. Palit et al., "Exclusive measurement of breakup reactions with the one-neutron halo nucleus ^{11}Be", in: *Phys. Rev. C*, vol. 68, iss. 3 (2003), p. 034318, DOI: 10.1103/PhysRevC.68.034318, URL: https://link.aps.org/doi/10.1103/PhysRevC.68.034318.

[50] S. Typel and G. Baur, "Effective-Range Approach and Scaling Laws for Electromagnetic Strength in Neutron-Halo Nuclei", in: *Phys. Rev. Lett.* Vol. 93, iss. 14 (2004), p. 142502, DOI: 10.1103/PhysRevLett.93.142502, URL: https://link.aps.org/doi/10.1103/PhysRevLett.93.142502.

[51] E.G. Fuller, "Photonuclear reaction cross sections for 12C, 14N and 16O", in: *Physics Reports*, vol. 127, no. 3, (1985), pp. 185 –231, ISSN: 0370-1573, DOI: https://doi.org/10.1016/0370-1573(85)90145-0, URL: http://www.sciencedirect.com/science/article/pii/0370157385901450.

[52] H. Sagawa and Toshio Suzuki, "Pigmy and giant dipole states in oxygen isotopes", in: *Phys. Rev. C*, vol. 59, iss. 6 (1999), pp. 3116–3119, DOI: 10.1103/PhysRevC.59.3116, URL: https://link.aps.org/doi/10.1103/PhysRevC.59.3116.

[53] J. Gibelin et al., "Decay Pattern of Pygmy States Observed in Neutron-Rich ^{26}Ne", in: *Phys. Rev. Lett.* Vol. 101, iss. 21 (2008), p. 212503, DOI: 10.1103/PhysRevLett.101.212503, URL: https://link.aps.org/doi/10.1103/PhysRevLett.101.212503.

[54] P. Adrich et al., "Evidence for Pygmy and Giant Dipole Resonances in ^{130}Sn and ^{132}Sn", in: *Phys. Rev. Lett.* Vol. 95, iss. 13 (2005), p. 132501, DOI: 10.1103/PhysRevLett.95.132501, URL: https://link.aps.org/doi/10.1103/PhysRevLett.95.132501.

[55] O. Wieland et al., "Search for the Pygmy Dipole Resonance in ^{68}Ni at 600 MeV/nucleon", in: *Phys. Rev. Lett.* Vol. 102, iss. 9 (2009), p. 092502, DOI: 10.1103/PhysRevLett.102.092502, URL: https://link.aps.org/doi/10.1103/PhysRevLett.102.092502.

[56] A. Tamii et al., "Complete Electric Dipole Response and the Neutron Skin in ^{208}Pb", in: *Phys. Rev. Lett.* Vol. 107, iss. 6 (2011), p. 062502, DOI: 10.1103/PhysRevLett.107.062502, URL: https://link.aps.org/doi/10.1103/PhysRevLett.107.062502.

[57] T.D. Poelhekken et al., "Low-energy isoscalar dipole strength in 40Ca, 58Ni, 90Zr and 208Pb", in: *Physics Letters B*, vol. 278, no. 4, (1992), pp. 423 – 427, ISSN: 0370-2693, DOI: https://doi.org/10.1016/0370-2693(92)90579-S, URL: http://www.sciencedirect.com/science/article/pii/037026939290579S.

[58] J. Endres et al., "Structure of the pygmy dipole resonance in ^{124}Sn", in: *Phys. Rev. C*, vol. 85, iss. 6 (2012), p. 064331, DOI: 10.1103/PhysRevC.85.064331, URL: https://link.aps.org/doi/10.1103/PhysRevC.85.064331.

[59] J. Endres et al., "Isospin Character of the Pygmy Dipole Resonance in ^{124}Sn", in: *Phys. Rev. Lett.* Vol. 105, iss. 21 (2010), p. 212503, DOI: 10.1103/PhysRevLett.105.212503, URL: https://link.aps.org/doi/10.1103/PhysRevLett.105.212503.

[60] F. C. L. Crespi et al., "Isospin Character of Low-Lying Pygmy Dipole States in ^{208}Pb via Inelastic Scattering of ^{17}O Ions", in: *Phys. Rev. Lett.* Vol. 113, iss. 1 (2014), p. 012501, DOI: 10.1103/PhysRevLett.113.012501, URL: https://link.aps.org/doi/10.1103/PhysRevLett.113.012501.

[61] F. C. L. Crespi et al., "1^- and 2^+ discrete states in ^{90}Zr populated via the $(^{17}\mathrm{O},^{17}\mathrm{O}'\gamma)$ reaction", in: *Phys. Rev. C*, vol. 91, iss. 2 (2015), p. 024323, DOI: 10.1103/PhysRevC.91.024323, URL: https://link.aps.org/doi/10.1103/PhysRevC.91.024323.

[62] L. Pellegri et al., "Pygmy dipole resonance in 124Sn populated by inelastic scattering of 17O", in: *Physics Letters B*, vol. 738, (2014), pp. 519 –523, ISSN: 0370-2693, DOI: https://doi.org/10.1016/j.physletb.2014.08.029, URL: http://www.sciencedirect.com/science/article/pii/S0370269314005966.

[63] N. Nakatsuka et al., "Observation of isoscalar and isovector dipole excitations in neutron-rich 20O", in: *Physics Letters B*, vol. 768, (2017), pp. 387 – 392, ISSN: 0370-2693, DOI: https://doi.org/10.1016/j.physletb.2017.03.017, URL: http://www.sciencedirect.com/science/article/pii/S0370269317301958.

[64] G. Cardella et al., "A new method for the determination of very small partial widths", in: *EPJ Web Conf.* Vol. 165, (2017), p. 01009, DOI: 10.1051/epjconf/201716501009, URL: https://doi.org/10.1051/epjconf/201716501009.

[65] *https://www.lns.infn.it/it/acceleratori/fribs-lns.html*, (2018).

[66] P. Russotto et al., "Status and Perspectives of the INFN-LNS In-Flight Fragment Separator", in: *Journal of Physics: Conference Series*, vol. 1014, no. 1, (2018), p. 012016, URL: http://stacks.iop.org/1742-6596/1014/i=1/a=012016.

[67] I. Lombardo et al., "Use of Large Surface MicroChannel Plates for the Tagging of Intermediate Energy Exotic Beams", in: *Nuclear Physics B - Proceedings Supplements*, vol. 215, no. 1, (2011), Proceedings of the 12th Topical Seminar on Innovative Particle and Radiation Detectors (IPRD10), pp. 272 –274, ISSN: 0920-5632, DOI: https://doi.org/10.1016/j.nuclphysbps.2011.04.028, URL: http://www.sciencedirect.com/science/article/pii/S0920563211002672.

[68] A. Pagano et al., "Fragmentation studies with the CHIMERA detector at LNS in Catania: recent progress", in: *Nuclear Physics A*, vol. 734, (2004), pp. 504 –511, ISSN: 0375-9474, DOI: https://doi.org/10.1016/j.nuclphysa.2004.01.093, URL: http://www.sciencedirect.com/science/article/pii/S0375947404001137.

[69] A. Pagano, "Studies of Nuclear Reactions and Time Scale with the 4π Detector CHIMERA", in: *Nuclear Physics News*, vol. 22, no. 1, (2012), pp. 25–30, DOI: 10.1080/10619127.2011.629922, eprint: https://doi.org/10.1080/10619127.2011.629922, URL: https://doi.org/10.1080/10619127.2011.629922.

[70] E.V. Pagano et al., "Status and perspective of FARCOS: A new correlator array for nuclear reaction studies", in: *EPJ Web of Conferences*, vol. 117, (2016), p. 10008, DOI: 10.1051/epjconf/201611710008, URL: https://doi.org/10.1051/epjconf/201611710008.

[71] L. Acosta et al., "FARCOS, a new array for femtoscopy and correlation spectroscopy", in: *EPJ Web of Conferences*, vol. 31, (2012), p. 00035, DOI: 10.1051/epjconf/20123100035, URL: https://doi.org/10.1051/epjconf/20123100035.

[72] G. Raciti et al., "Intermediate energies tagged RIBs", in: *Nuclear Instruments and Methods in Physics Research Section B: Beam Interactions with Materials and Atoms*, vol. 266, no. 19, (2008), Proceedings of the XVth International Conference on Electromagnetic Isotope Separators and Techniques Related to their Applications, pp. 4632 –4636, ISSN: 0168-583X, DOI: https://doi.org/10.1016/j.nimb.2008.05.153, URL: http://www.sciencedirect.com/science/article/pii/S0168583X0800791X.

[73] G. Knoll, in: *Radiation Detection and Measurement*, (2000).

[74] *http://lise.nscl.msu.edu/lise.html*, (2018).

[75] D. Pierroutsakou et al., "The experimental set-up of the RIB in-flight facility EXOTIC", in: *Nuclear Instruments and Methods in Physics Research Section A: Accelerators, Spectrometers, Detectors and Associated Equipment*, vol. 834, (2016), pp. 46 –70, ISSN: 0168-9002, DOI: https://doi.org/10.1016/j.nima.2016.07.019, URL: http://www.sciencedirect.com/science/article/pii/S0168900216307367.

[76] P. Russotto, "Dynamical emission of heavy fragments in the 112,124Sn+ 58,64Ni reactions at 35 AMeV as seen with CHIMERA", in: *PhD Thesis, Università degli Studi di Catania*, (2003-2006).

[77] S. Aiello et al., "Chimera: a project of a 4 π detector for heavy ion reactions studies at intermediate energy", in: *Nuclear Physics A*, vol. 583, (1995), Nucleus-Nucleus Collisions, pp. 461 –464, ISSN: 0375-9474, DOI: https://doi.org/10.1016/0375-9474(94)00705-R, URL: http://www.sciencedirect.com/science/article/pii/037594749400705R.

[78] S. Aiello et al., "Timing performances and edge effects of detectors worked from 6-in. silicon slices", in: *Nuclear Instruments and Methods in Physics Research Section A: Accelerators, Spectrometers, Detectors and Associated Equipment*, vol. 385, no. 2, (1997), pp. 306 –310, ISSN: 0168-9002, DOI: https://doi.org/10.1016/S0168-9002(96)00881-9, URL: http://www.sciencedirect.com/science/article/pii/S0168900296008819.

[79] S. Aiello et al., "Plasma effects for heavy ions in implanted silicon detectors", in: *Nuclear Instruments and Methods in Physics Research Section A: Accelerators, Spectrometers, Detectors and Associated Equipment*, vol. 427, no. 3, (1999), pp. 510 –517, ISSN: 0168-9002, DOI: https://doi.org/10.1016/S0168-9002(98)01426-0, URL: http://www.sciencedirect.com/science/article/pii/S0168900298014260.

[80] I. Lombardo, "N/Z effects on nuclear reactions near the fragmentation threshold", in: *PhD Thesis, Università degli Studi di Catania*, (2007-2010).

[81] S. Aiello et al., "Light response and particle identification with large CsI(TI) crystals coupled to photodiodes", in: *Nuclear Instruments and Methods in Physics Research Section A: Accelerators, Spectrometers, Detectors and Associated Equipment*, vol. 369, no. 1, (1996), pp. 50 –54, ISSN: 0168-9002, DOI: https://doi.org/10.1016/0168-9002(95)00763-6, URL: http://www.sciencedirect.com/science/article/pii/0168900295007636.

[82] J.B.A. England, G.M. Field, and T.R. Ophel, "Z-identification of charged particles by signal risetime in silicon surface barrier detectors", in: *Nuclear Instruments and Methods in Physics Research Section A: Accelerators, Spectrometers, Detectors and Associated Equipment*, vol. 280, no. 2, (1989), pp. 291 – 298, ISSN: 0168-9002, DOI: https://doi.org/10.1016/0168-9002(89)90920-0, URL: http://www.sciencedirect.com/science/article/pii/0168900289909200.

[83] A. Pagano et al., "Physics with the Chimera detector at LNS in Catania: the REVERSE experiment", in: *Nuclear Physics A*, vol. 681, no. 1, (2001), 3rd Catania Relativistic Ion Studies, pp. 331 –338, ISSN: 0375-9474, DOI: https://doi.org/10.1016/S0375-9474(00)00536-4, URL: http://www.sciencedirect.com/science/article/pii/S0375947400005364.

[84] M. Alderighi et al., "Particle identification method in the CsI(Tl) scintillator used for the CHIMERA 4π detector", in: *Nuclear Instruments and Methods in Physics Research Section A: Accelerators, Spectrometers, Detectors and Associated Equipment*, vol. 489, no. 1, (2002), pp. 257 –265, ISSN: 0168-9002, DOI: https://doi.org/10.1016/S0168-9002(02)00800-8, URL: http://www.sciencedirect.com/science/article/pii/S0168900202008008.

[85] P. Kreutz et al., "Photodiode readout and pulse shape analysis of CsI(Tl) scintillator signals", in: *Nuclear Instruments and Methods in Physics Research Section A: Accelerators, Spectrometers, Detectors and Associated Equipment*, vol. 260, no. 1, (1987), pp. 120 –123, ISSN: 0168-9002, DOI: https://doi.org/10.1016/0168-9002(87)90392-5, URL: http://www.sciencedirect.com/science/article/pii/0168900287903925.

[86] R.J. Meijer et al., "A compact multidetector system for highly energetic charged particles", in: *Nuclear Instruments and Methods in Physics Research Section A: Accelerators, Spectrometers, Detectors and Associated Equipment*, vol. 264, no. 2, (1988), pp. 285 –290, ISSN: 0168-9002, DOI: https://doi.org/10.1016/0168-9002(88)90916-3, URL: http://www.sciencedirect.com/science/article/pii/0168900288909163.

[87] W.G. Gong et al., "Resolution tests of CsI(Tl) scintillators read out by pin diodes", in: *Nuclear Instruments and Methods in Physics Research Section A: Accelerators, Spectrometers, Detectors and Associated Equipment*, vol. 268, no. 1, (1988), pp. 190 –199, ISSN: 0168-9002, DOI: https://doi.org/10.1016/

0168-9002(88)90605-5, URL: http://www.sciencedirect.com/science/article/pii/0168900288906055.

[88] Xi Hongfei et al., "The use of CsI(Tl) scintillators with photodiode readout in heavy ion experiments", in: *Nuclear Instruments and Methods in Physics Research Section A: Accelerators, Spectrometers, Detectors and Associated Equipment*, vol. 320, no. 3, (1992), pp. 504 –507, ISSN: 0168-9002, DOI: https://doi.org/10.1016/0168-9002(92)90946-2, URL: http://www.sciencedirect.com/science/article/pii/0168900292909462.

[89] R. Laforest et al., "Particle identification with FAUST detector", in: *Nuclear Instruments and Methods in Physics Research Section A: Accelerators, Spectrometers, Detectors and Associated Equipment*, vol. 404, no. 2, (1998), pp. 470 – 472, ISSN: 0168-9002, DOI: https://doi.org/10.1016/S0168-9002(97)01192-3, URL: http://www.sciencedirect.com/science/article/pii/S0168900297011923.

[90] D. Guinet et al., "Using the combination Csl(TI) and photodiode for identification and energy measurement of light particles", in: *Nuclear Instruments and Methods in Physics Research Section A: Accelerators, Spectrometers, Detectors and Associated Equipment*, vol. 278, no. 2, (1989), pp. 614 –616, ISSN: 0168-9002, DOI: https://doi.org/10.1016/0168-9002(89)90889-9, URL: http://www.sciencedirect.com/science/article/pii/0168900289908899.

[91] M. Moszyński et al., "Particle identification by digital charge comparison method applied to CsI(Tl) crystal coupled to photodiode", in: *Nuclear Instruments and Methods in Physics Research Section A: Accelerators, Spectrometers, Detectors and Associated Equipment*, vol. 336, no. 3, (1993), pp. 587 – 590, ISSN: 0168-9002, DOI: https://doi.org/10.1016/0168-9002(93)91267-Q, URL: http://www.sciencedirect.com/science/article/pii/016890029391267Q.

[92] D.G. Sarantites et al., ""The microball" Design, instrumentation and response characteristics of a 4 π multidetector exit channel-selection device for spectroscopic and reaction mechanism studies with Gammasphere", in: *Nuclear Instruments and Methods in Physics Research Section A: Accelerators, Spectrometers, Detectors and Associated Equipment*, vol. 381, no. 2, (1996), pp. 418 –432, ISSN: 0168-9002, DOI: https://doi.org/10.1016/S0168-9002(96)00785-1, URL: http://www.sciencedirect.com/science/article/pii/S0168900296007851.

[93] W. Skulski and M. Momayezi, "Particle identification in CsI(Tl) using digital pulse shape analysis", in: *Nuclear Instruments and Methods in Physics Research Section A: Accelerators, Spectrometers, Detectors and Associated Equipment*, vol. 458, no. 3, (2001), pp. 759 –771, ISSN: 0168-9002, DOI: https://doi.org/10.1016/S0168-9002(00)00938-4, URL: http://www.sciencedirect.com/science/article/pii/S0168900200009384.

[94] E. Farnea et al., "Conceptual design and Monte Carlo simulations of the AGATA array", in: *Nuclear Instruments and Methods in Physics Research Section A: Accelerators, Spectrometers, Detectors and Associated Equipment*, vol. 621, no. 1, (2010), pp. 331 –343, ISSN: 0168-9002, DOI: https://doi.org/10.1016/j.nima.2010.04.043, URL: http://www.sciencedirect.com/science/article/pii/S0168900210008922.

[95] M.A. Deleplanque et al., "GRETA: utilizing new concepts in gamma ray detection", in: *Nuclear Instruments and Methods in Physics Research Section A: Accelerators, Spectrometers, Detectors and Associated Equipment*, vol. 430, no. 2, (1999), pp. 292 –310, ISSN: 0168-9002, DOI: https://doi.org/10.1016/S0168-9002(99)00187-4, URL: http://www.sciencedirect.com/science/article/pii/S0168900299001874.

[96] M. Petri et al., "The use of EXOGAM for in-beam spectroscopy of proton drip-line nuclei with radioactive ion beams", in: *Nuclear Instruments and Methods in Physics Research Section A: Accelerators, Spectrometers, Detectors and Associated Equipment*, vol. 607, no. 2, (2009), pp. 412 –420, ISSN: 0168-9002, DOI: https://doi.org/10.1016/j.nima.2009.04.031, URL: http://www.sciencedirect.com/science/article/pii/S0168900209008341.

[97] N. Warr, "The Miniball spectrometer", in: *The European Physical Journal A*, vol. 49, no. 3, (2013), p. 40, ISSN: 1434-601X, DOI: 10.1140/epja/i2013-13040-9, URL: https://doi.org/10.1140/epja/i2013-13040-9.

[98] J. J. Valiente-Dobón et al., "Status of the Gamma-Ray spectrometer GALILEO", in: *INFN-LNL Ann. Report*, (2014), p. 95.

[99] G. Cardella et al., "Particle gamma correlations in 12C measured with the CsI(Tl) based detector array CHIMERA", in: *Nuclear Instruments and Methods in Physics Research Section A: Accelerators, Spectrometers, Detectors and Associated Equipment*, vol. 799, (2015), pp. 64 –69, ISSN: 0168-9002, DOI: https://doi.org/10.1016/j.nima.2015.07.054, URL: http://www.sciencedirect.com/science/article/pii/S0168900215008839.

[100] W.R. Leo, in: *Techniques for Nuclear and Particle Physics Experiments*, (1994).

[101] *http://indra.in2p3.fr/kaliveda/index.html*, (2018).

[102] L. Auditore, A. Pagano, and P. Russotto, "Preliminary study for the detection of neutrons in heavy-ion collisions with charged particle detectors", in: *EPJ Web of Conferences*, vol. 88, (2015), p. 01001, DOI: 10.1051/epjconf/20158801001, URL: https://doi.org/10.1051/epjconf/20158801001.

[103] D. B. Pelowitz, in: *MCNPX User's Manual, Version 2.5.0, Los Alamos National Laboratory report LA-CP-05-0369*, (2005).

[104] G. Cardella et al., "Past and future detector arrays for complete event reconstruction in heavy-ion reactions", in: *Nuovo Cim.* Vol. C39, no. 6, (2017), p. 407, DOI: 10.1393/ncc/i2016-16407-6.

[105] G. Verde et al., "The Farcos project: Femtoscope Array for Correlations and Femtoscopy", in: *Journal of Physics: Conference Series*, vol. 420, no. 1, (2013), p. 012158, URL: http://stacks.iop.org/1742-6596/420/i=1/a=012158.

[106] L. Quattrocchi et al., "The FARCOS project. First characterization of CsI(Tl) crystals of the FARCOS array using charged particle beams at LNS", in: *EPJ Web of Conferences*, vol. 66, (2014), p. 11001, DOI: 10.1051/epjconf/20146611001, URL: https://doi.org/10.1051/epjconf/20146611001.

[107] J. Pouthas et al., "INDRA, a 4 π charged product detection array at GANIL", in: *Nuclear Instruments and Methods in Physics Research Section A: Accelerators, Spectrometers, Detectors and Associated Equipment*, vol. 357, no. 2, (1995), pp. 418 –442, ISSN: 0168-9002, DOI: https://doi.org/10.1016/0168-9002(94)01543-0, URL: http://www.sciencedirect.com/science/article/pii/0168900294015430.

[108] F. Gramegna et al., "A telescope with microstrip gas chambers for the detection of charged products in heavy-ion reactions", in: *Nuclear Instruments and Methods in Physics Research Section A: Accelerators, Spectrometers, Detectors and Associated Equipment*, vol. 389, no. 3, (1997), pp. 474 –478, ISSN: 0168-9002, DOI: https://doi.org/10.1016/S0168-9002(96)01212-0, URL: http://www.sciencedirect.com/science/article/pii/S0168900296012120.

[109] The FAZIA Collaboration, R. Bougault, et al., "The FAZIA project in Europe: R&D phase", in: *The European Physical Journal A*, vol. 50, no. 2, (2014), p. 47, ISSN: 1434-601X, DOI: 10.1140/epja/i2014-14047-4, URL: https://doi.org/10.1140/epja/i2014-14047-4.

[110] E. Pollacco et al., "MUST2: A new generation array for direct reaction studies", in: *The European Physical Journal A - Hadrons and Nuclei*, vol. 25, no. 1, (2005), pp. 287–288, ISSN: 1434-601X, DOI: 10.1140/epjad/i2005-06-162-5, URL: https://doi.org/10.1140/epjad/i2005-06-162-5.

[111] *https://web.infn.it/spes/index.php/nuclear-physics/spes-instrumentation/150-trace*, (2018).

[112] G. Verde et al., "Correlations and characterization of emitting sources", in: *The European Physical Journal A - Hadrons and Nuclei*, vol. 30, no. 1, (2006), pp. 81–108, ISSN: 1434-601X, DOI: 10.1140/epja/i2006-10109-6, URL: https://doi.org/10.1140/epja/i2006-10109-6.

[113] B. Davin et al., "LASSA: a large area silicon strip array for isotopic identification of charged particles", in: *Nuclear Instruments and Methods in Physics Research Section A: Accelerators, Spectrometers, Detectors and Associated Equipment*, vol. 473, no. 3, (2001), pp. 302 –318, ISSN: 0168-9002, DOI: https://doi.org/10.1016/S0168-9002(01)00295-9, URL: http://www.sciencedirect.com/science/article/pii/S0168900201002959.

[114] H. F. Xi et al., "Dynamical emission and isotope thermometry", in: *Phys. Rev. C*, vol. 58, iss. 5 (1998), R2636–R2639, DOI: 10.1103/PhysRevC.58.R2636, URL: https://link.aps.org/doi/10.1103/PhysRevC.58.R2636.

[115] V. Serfling et al., "Temperatures of Exploding Nuclei", in: *Phys. Rev. Lett.* Vol. 80, iss. 18 (1998), pp. 3928–3931, DOI: 10.1103/PhysRevLett.80.3928, URL: https://link.aps.org/doi/10.1103/PhysRevLett.80.3928.

[116] M.S. Wallace et al., "The high resolution array (HiRA) for rare isotope beam experiments", in: *Nuclear Instruments and Methods in Physics Research Section A: Accelerators, Spectrometers, Detectors and Associated Equipment*, vol. 583, no. 2, (2007), pp. 302 –312, ISSN: 0168-9002, DOI: https://doi.org/10.1016/j.nima.2007.08.248, URL: http://www.sciencedirect.com/science/article/pii/S016890020701947X.

[117] E. De Filippo et al., "Correlations between emission timescale of fragments and isospin dynamics in ^{124}Sn+^{64}Ni and ^{112}Sn+^{58}Ni reactions at 35A MeV", in: *Phys. Rev. C*, vol. 86, iss. 1 (2012), p. 014610, DOI: 10.1103/PhysRevC.86.014610, URL: https://link.aps.org/doi/10.1103/PhysRevC.86.014610.

[118] L. Acosta et al., "Campaign of measurements to probe the good performance of the new array FARCOS for spectroscopy and correlations.", in: *Journal of Physics: Conference Series*, vol. 730, no. 1, (2016), p. 012001, URL: http://stacks.iop.org/1742-6596/730/i=1/a=012001.

[119] *http://www.srim.org/*, (2018).

[120] N.S. Martorana et al., "First measurement of the isoscalar excitation above the neutron emission threshold of the Pygmy Dipole Resonance in 68Ni", in: *Physics Letters B*, vol. 782, (2018), pp. 112 –116, ISSN: 0370-2693, DOI: https://doi.org/10.1016/j.physletb.2018.05.019, URL: http://www.sciencedirect.com/science/article/pii/S0370269318303836.

[121] N.S. Martorana et al., "Experimental study of the Pygmy Dipole Resonance in the 68Ni nucleus", in: *Acta physica polonica B*, vol. 49, (2018), pp. 475–482, DOI: DOI:10.5506/APhysPolB.49.475.

[122] F. Pühlhofer, "On the interpretation of evaporation residue mass distributions in heavy-ion induced fusion reactions", in: *Nuclear Physics A*, vol. 280, no. 1, (1977), pp. 267 –284, ISSN: 0375-9474, DOI: https://doi.org/10.1016/0375-9474(77)90308-6, URL: http://www.sciencedirect.com/science/article/pii/0375947477903086.

[123] I. Diószegi, "Comment on "Spin and excitation energy dependence of fission survival for the ^{19}F+^{175}Lu system"", in: *Phys. Rev. C*, vol. 64, iss. 1 (2001), p. 019801, DOI: 10.1103/PhysRevC.64.019801, URL: https://link.aps.org/doi/10.1103/PhysRevC.64.019801.

[124] M. Vandebrouck et al., "Measurement of the Isoscalar Monopole Response in the Neutron-Rich Nucleus ^{68}Ni", in: *Phys. Rev. Lett.* Vol. 113, iss. 3 (2014), p. 032504, DOI: 10.1103/PhysRevLett.113.032504, URL: https://link.aps.org/doi/10.1103/PhysRevLett.113.032504.

[125] M. Vandebrouck et al., "Isoscalar response of ^{68}Ni to α-particle and deuteron probes", in: *Phys. Rev. C*, vol. 92, iss. 2 (2015), p. 024316, DOI: 10.1103/PhysRevC.92.024316, URL: https://link.aps.org/doi/10.1103/PhysRevC.92.024316.

[126] *https://root.cern.ch/doc/v612/classTTree.html*, (2018).

[127] S. Agostinelli et al., "Geant4- a simulation toolkit", in: *Nuclear Instruments and Methods in Physics Research Section A: Accelerators, Spectrometers, Detectors and Associated Equipment*, vol. 506, no. 3, (2003), pp. 250 –303, ISSN: 0168-9002, DOI: https://doi.org/10.1016/S0168-9002(03)01368-8, URL: http://www.sciencedirect.com/science/article/pii/S0168900203013688.

[128] D. Kresan et al., "Event Reconstruction and Analysis in the R3BRoot Framework", in: *Journal of Physics: Conference Series*, vol. 523, no. 1, (2014), p. 012034, URL: http://stacks.iop.org/1742-6596/523/i=1/a=012034.

[129] T. Aumann and T. Nakamura, "The electric dipole response of exotic nuclei", in: *Physica Scripta*, vol. 2013, no. T152, (2013), p. 014012, URL: http://stacks.iop.org/1402-4896/2013/i=T152/a=014012.

[130] E.C. Pollacco et al., "GET: A generic electronics system for TPCs and nuclear physics instrumentation", in: *Nuclear Instruments and Methods in Physics Research Section A: Accelerators, Spectrometers, Detectors and Associated Equipment*, vol. 887, (2018), pp. 81 –93, ISSN: 0168-9002, DOI: https://doi.org/10.1016/j.nima.2018.01.020, URL: http://www.sciencedirect.com/science/article/pii/S0168900218300342.

[131] *https://root.cern.ch/root/html534/TGenPhaseSpace.html*, (2018).

[132] L. Calabretta et al., "Overview of the future upgrade of the INFN-LNS superconducting cyclotron", in: *Modern Physics Letters A*, vol. 32, no. 17, (2017), p. 1740009, DOI: 10.1142/S0217732317400090, eprint: https://doi.org/10.1142/S0217732317400090, URL: https://doi.org/10.1142/S0217732317400090.

[133] R. Anne et al., "The achromatic spectrometer LISE at GANIL", in: *Nuclear Instruments and Methods in Physics Research Section A: Accelerators, Spectrometers, Detectors and Associated Equipment*, vol. 257, no. 2, (1987), pp. 215 –232, ISSN: 0168-9002, DOI: https://doi.org/10.1016/0168-9002(87)90741-8, URL: http://www.sciencedirect.com/science/article/pii/0168900287907418.

[134] A. Amato et al., "The upgrade of the radioactive ion beam diagnostics at LNS", in: *LNS- Activity Report*, (2009), p. 160.

[135] E.G. Lanza et al., "Role of anharmonicities and nonlinearities in heavy ion collisions A microscopic approach", in: *Nuclear Physics A*, vol. 613, no. 4, (1997), pp. 445 –471, ISSN: 0375-9474, DOI: https://doi.org/10.1016/

S0375-9474(96)00444-7, URL: http://www.sciencedirect.com/science/article/pii/S0375947496004447.